Non-Penetrating Microelectrode Interfaces for Cortical Neuroprosthetic Applications with a Focus on Sensory Encoding: Feasibility and Chronic Performance in Striate Cortex

by

Denise Oswalt

A Dissertation Presented in Partial Fulfillment
of the Requirements for the Degree
Doctor of Philosophy

Approved October 2018 by the
Graduate Supervisory Committee:

Bradley Greger, Chair
Christopher Buneo
Zaman Mirzadeh
Antonia Papandreou-Suppappola
Stephen Helms Tillery

ARIZONA STATE UNIVERSITY

December 2018

ABSTRACT

Growing understanding of the neural code and how to speak it has allowed for notable advancements in neural prosthetics. With commercially-available implantable systems with bi-directional neural communication on the horizon, there is an increasing imperative to develop high resolution interfaces that can survive the environment and be well tolerated by the nervous system under chronic use. The sensory encoding aspect optimally interfaces at a scale sufficient to evoke perception but focal in nature to maximize resolution and evoke more complex and nuanced sensations. Microelectrode arrays can maintain high spatial density, operating on the scale of cortical columns, and can be either penetrating or non-penetrating. The non-penetrating subset sits on the tissue surface without puncturing the parenchyma and is known to engender minimal tissue response and less damage than the penetrating counterpart, improving long term viability in vivo. Provided non-penetrating microelectrodes can consistently evoke perception and maintain a localized region of activation, non-penetrating micro-electrodes may provide an ideal platform for a high performing neural prosthesis; this dissertation explores their functional capacity.

The scale at which non-penetrating electrode arrays can interface with cortex is evaluated in the context of extracting useful information. Articulate movements were decoded from surface microelectrode electrodes, and additional spatial analysis revealed unique signal content despite dense electrode spacing. With a basis for data extraction established, the focus shifts towards the information encoding half of neural interfaces. Finite element modeling was used to compare tissue recruitment under surface stimulation across electrode scales. Results indicated charge density-based metrics provide a reasonable approximation for current levels required to evoke a visual sensation and showed tissue recruitment increases exponentially with electrode diameter. Micro-

scale electrodes (0.1 – 0.3 mm diameter) could sufficiently activate layers II/III in a model tuned to striate cortex while maintaining focal radii of activated tissue.

In vivo testing proceeded in a nonhuman primate model. Stimulation consistently evoked visual percepts at safe current thresholds. Tracking perception thresholds across one year reflected stable values within minimal fluctuation. Modulating waveform parameters was found useful in reducing charge requirements to evoke perception. Pulse frequency and phase asymmetry were each used to reduce thresholds, improve charge efficiency, lower charge per phase – charge density metrics associated with tissue damage. No impairments to photic perception were observed during the course of the study, suggesting limited tissue damage from array implantation or electrically induced neurotoxicity. The subject consistently identified stimulation on closely spaced electrodes (2 mm center-to-center) as separate percepts, indicating sub-visual degree discrete resolution may be feasible with this platform. Although continued testing is necessary, preliminary results supports epicortical microelectrode arrays as a stable platform for interfacing with neural tissue and a viable option for bi-directional BCI applications.

TABLE OF CONTENTS

LIST OF TABLES

LIST OF FIGURES

Figure Page

CHAPTER 1

BACKGROUND INTRODUCTION

ELECTRODE INTERFACES

In the growing history of studying function and structure of the cerebral cortex, electrophysiology has been a central means of investigation. Throughout that time, techniques have advanced to allow for interfacing at a variety of scales and depths, with each technique allowing for collection of specific biophysical features. As such, it is becoming increasingly imperative to consider the balance of features in selecting an approach for a given application. Brain-computer interfaces (BCI), and those specifically for use in neuroprosthetics, require high spatiotemporal resolution and stability over an extended period.

In selecting an interface, there is typically a tradeoff between signal quality and invasiveness. The least invasive approach for BCI is electroencephalography (EEG), which records electric potentials from the scalp. The resulting signals are smoothed over an area of 10 cm^2 from the attenuating effect of the soft and hard tissues separating the recording site from the source. There is little discernable relationship between the EEG trace and the firing patterns of the contributing neurons(Buzsaki, Anastassiou, & Koch, 2012a). EEG based BCI applications are dependent on event related potentials (ERPs) or learned control over lower frequency signals, which limits potential applications and require focused attention and effort to use (Padmavathi & Ranganathan, 2008). Despite improvements from advanced signal processing techniques (Kevric & Subasi, 2017; Kottaimalai, Rajasekaran, Selvam , & Kannapiran, 2013; Kottaimalai, Rajasekeran, Selvam, & Kannapiran, 2013; G. Lange, C. Low, K. Johar, F. Hanapiah, & F. Kamaruzaman, 2016; G. Lange, C. Y. Low, K. Johar, F. A. Hanapiah, & F. Kamaruzaman, 2016; Dong Wen, Jia, Lian, Zhou, & Lu, 2016; D. Wen, Jia, Zhou, & Lu, 2016) and its clinical relevance, EEG has limited functionality in BCI because of its low spatiotemporal resolution (J. Wolpaw, N. Birbaumer, D. McFarland, G. Pfurtscheller, & T. Vaughan, 2002; Jonathan Wolpaw, Niels Birbaumer, Dennis McFarland, Gert Pfurtscheller, & Theresa Vaughan, 2002).

A more invasive approach, electrocorticography (ECoG), improves spatiotemporal resolution and signal fidelity by interfacing directly with dura or cortex. ECoG grids have been an invaluable tool in both clinical diagnostics and medical research for since their introduction over 50 years ago (Buzsaki et al., 2012a; Chen, Canales, & Anikeeva, 2017; Yang, Hakimian, & Schwartz, 2014). Standard ECoG typically consists of subdural electrodes with diameters between 2 to 5 mm spaced by centimeter distances, and capture waveforms representing integration of activity within an estimated range of 5 to 10 mm^2 (Buzsaki et al., 2012a; Chen et al., 2017). While ECoG electrodes at this scale have been successfully used to decode language, motor, and somatosensory activity as well as evoke sensations (Chang et al., 2010; Chao, Nagasaka, & Fuji, 2010; C. Chestek et al., 2013; Hiremath et al., 2017; Kubanek, Miller, Ojemann, & Schalk, 2009; Mugler et al., 2014; Winawer & Parvizi, 2016), the columnar organization of neocortex and the underlying biophysics of the cellular electrophysiology suggests a size inconsistency. Unique spatiotemporal dynamics have been shown to exist within millimeter variations on the cortical surface, as observed with microelectrode recordings (S. Kellis et al., 2011). For BCI applications, the cortical activity ECoG attempts to record likely occurs at a smaller scale than it can resolve(Schevon et al., 1997).

Behaviorally relevant information in complex animals is depended on coordinated activity by populations of neurons(Panzeri, Macke, Gross, & Kayser, 2015). Micrometer to submillimeter scale subdivisions exist within cortical regions of the brain. These cortical columns are considered individual processing units where a localized population of cells combine to encode a certain processing function or response (V. B. Mountcastle, 1957). Studies have suggested information in the cerebral cortex may be represented by the synchronization of neural activity in different columns via synaptic connectivity (Hill, 2012). These synchronous oscillations have been observed in sensory and motor areas and correlated with perceptual binding, attention, and movement preparation (Bauer, 2006).

These ionic processes, largely synaptic potentials, summate to yield the local field potentials (LFPs) observed on ECoG electrodes. LFP activity contains a mixture of local and distant potentials volume conducted through the medium of the brain (Buzsaki et al., 2012a). As it

constitutes a summation of activity, synchronous oscillations will yield a larger influence on the resulting waveform (Mehring et al., 2004). The signal content is also dependent on the electrode scale; the volume of tissue represented is proportional to the geometric surface area of the electrode. For high magnitude signal deflections to be observed on larger electrodes requires broader synchronization of the underlying tissue as the summed potentials are integrated across a larger population of cells (Chang, 2015; S. Kellis et al., 2016; Mehring et al., 2004; Rouse, Williams, Wheeler, & Moran, 2016; Wang et al., 2017). This implies that ECoG, while capable of discriminating larger, coordinated fluctuations associated with gross motor movement, will likely not have the specificity to detect smaller fluctuations associated with fine motor movements.

Intracortical microelectrode arrays (MEAs), like the Utah Array (Blackrock Microsystems) provide small inter-electrode spacing and electrode-tissue interfaces to avoid under-sampling cortical activity. These arrays consist of up to 128 shank-like electrodes, with approximately 4μm diameter tips spaced 200-400μm center-to-center and extend into cortex 1-3mm(Maynard, Nordhausen, & Normann, 1997; Wise, 2005). Intracortical MEAs are often considered for use in neuroprosthetics because of their high signal quality and spatiotemporal resolution, resulting from their close apposition to the signal source. The scale and placement of the array allows for collection of both action potentials from individual cells and local field potentials from tightly localized cell populations. The high-impedance electrodes have a tight recording radius and can acquire neural signals with high spatial resolution (Tsanov et al., 2011). While the spatial extent of LFPs is debated, it is significantly more localized than the signals observed on ECoG (Buzsaki, Anastassiou, & Koch, 2012b; V. Mountcastle, 1978). A recent study comparing the spatial and temporal dynamics of neural signal recorded at different scales suggests that LFPs recorded intracortically and epicortically with micro electrodes operate at a similar cortical column scale(S. Kellis et al., 2016).

Although intracortical MEAs have shown considerable use in short term studies, fewer studies have had long term success. This may be in part due to the tissue response evoked by the array and a mismatch between the flexibility of tissue and rigidity of the shank electrodes. Implantation of the array is also considered traumatic, and associated with localized neuronal and

glial cell death, disruption of vasculature, and compromise of the blood brain barrier(Fernandez et al., 2014). A larger scale analysis of failure modes for the Utah array reported 56% of arrays failing within a year of implantation (Barrese et al., 2013). Reports of tissue damage resulting from these arrays include tissue dimpling, inflammation, foreign body response and encapsulation, decreased neural density near the electrode site, and persistent activation of microglia, potentially leading to neurotoxicity (Polikov, Tresco, & Reichert, 2005). This effectively reduces the long-term viability of penetrating arrays and contributes to the instability of the interface after chronic implantation. There is comparatively less documentation of the tissue response to chronically implanted epicortical arrays; however, because they do not penetrate the pial surface it is likely the foreign body response will be reduced (Christie, Ashmont, House, & Greger, 2016).

Epicortical microelectrode arrays, which use submillimeter electrode diameters and millimeter-scale inter-electrode spacing, were designed to record LFPs at high spatiotemporal resolution with an invasiveness equivalent to ECoG. The electrodes in these micro-electrocorticography (micro-ECoG) arrays have a small surface area and high impedance and therefore record local field potentials rather than the macro-scale field potentials recorded on ECoG grids (Schalk & Leuthardt, 2011). LFPs recorded from the surface of the cortex may be less prone to signal degradation over time compared to those collected with intracortical microelectrode arrays (Schendel et al., 2013). The smaller inter-electrode spacing of non-penetraing microelectrode arrays grids provides the ability to sample the closely spaced areas of motor cortex that control different movement (C. Chestek et al., 2013; C. A. Chestek et al., 2013; Crone, 2006; Freeman, Rogers, Holmes, & Silbergeld, 2000; J. Kim, J. Wilson, & J. Williams, 2007; J. Kim, J. A. Wilson, & J. C. Williams, 2007; E. Leuthardt, Z. Freudenberg, D. Bundy, & J. Roland, 2009; E. C. Leuthardt, Z. Freudenberg, D. Bundy, & J. Roland, 2009; V Menon et al., 1996; V. Menon et al., 1996; Miller et al., 2007; M. Slutzky, Jordan, & Miller, 2008; M. W. Slutzky et al., 2010; Van Gompel et al., 2008; Worrell et al., 2008). These arrays have shown promise for decoding speech (S. Kellis et al., 2010; Leuthardt et al., 2011), arm movement (S. S. Kellis, House, Thomson, Brown, & Greger, 2009) and basic hand movements (E. C. Leuthardt et al., 2009).

ELECTRICAL STIMULATION

Cortical electrical stimulation needs to be both safe and effective, meaning the application need to minimize damage to tissue and electrodes while consistently evoking a physiological response in terms of the sensation perceived and the current threshold over time. The parameters affecting the safety and efficacy of cortical stimulation can be divided into electrical and physical. Electrical parameters in this context are those directly pertaining to the size, shape, intensity, and duration of an applied stimulus. Physical parameters are those relating to electrode characteristics, i.e. geometry, material, and placement.

Prior to determining the specifics of an electrical stimulus, it is necessary to understand the thresholds for damage. Traditional metrics of damage thresholds for electrical stimulation of nervous tissue focus on the charge density and charge per phase of an applied pulse. The Shannon equation can be used to describe the boundary between tissue damaging and non-damaging levels with a linear relationship between charge density and charge per phase (Cogan, Ludwig, Welle, & Takmakov, 2016). This is given by:

$$\log\left(\frac{Q}{A}\right) = k - \log(Q) \tag{1.1}$$

where Q is charge per phase (μC) and Q/A is the charge density per phase (μC/cm^2) (Merrill, Bikson, & Jefferys, 2005). This relationship was determined through experimentation with large scale surface electrodes with a geometric surface area (GSA) of .01cm^2 – .5cm^2 and predicts damage thresholds well for macroelectrodes. Current clinical applications generally impose a recommended limit on charge density of a stimulation pulse of 30μC/cm^2 out of a concern for tissue damage, however some studies have seen damage as low as 12 μC/cm^2 and other studies have reported no damage up to 60 μC/cm^2. Although a factor to consider, there are limitations of this predictive model and its applicability to micro-stimulation. Current density thresholds for damage have been shown to scale differently with microelectrodes (GSA<.01cm^2). The charge density to charge per phase relationship described by the Shannon model may not directly translate to microelectrodes. Charge per phase appears to be a stronger predictor of the damage threshold for microelectrodes with an approximate damage threshold observed around 4 nC/phase (Cogan et

al., 2016). The geometric surface area (GSA) of a stimulating electrode has non-trivial implications for the damage threshold and should be taken into account when determining the electrical parameters for therapeutic stimulation.

Charge injection can be either capacitive or faradaic. In capacitive charge injection charge is transferred via electron charging whereas faradaic charge transfer occurs through reduction and oxidization reactions at the electrode surface. Capacitive charging is considered more desirable from a safety perspective because no chemical species are created or consumed during the stimulation phase. However, neural stimulation often employs faradic charge injection because of its higher capacity for charge transfer (Cogan et al., 2016; Merrill et al., 2005). Manipulation of the material properties, specifically increasing the porosity, can increase the charge injection capacity of capacitive micro-stimulation. Sputtered titanium nitride intracortical microelectrodes are highly porous, with an electrochemical surface area several times larger than its geometric surface area, allowing for a charge injection capacity close to that of faradaic electrodes (Cogan, 2008). High dielectric constant coatings can also be used to increase charge-injection capacity for capacitive electrodes, as observed in tantalum/tantalum oxide electrodes (Cogan, 2008). Faradaic electrodes commonly use noble metal alloys (Pt, PtIr), however their charge-injection capacities are marginal for microelectrode stimulation and require coatings like iridium oxide to increase charge transfer (Cogan, 2008). Faradaic materials, because of their means of charge transfer, can induce irreversible processes that cause electrode or tissue damage. However, it should be noted that studies have not found statistically significant differences in cortical damage caused by faradaic and capacitive electrodes when equivalent charge balancing stimulation techniques are applied (Merrill et al., 2005). This suggests that current passage through tissue is a contributing factor to tissue damage, rather than damage being solely induced by electrochemical reactions at the electrode-tissue interface (Merrill et al., 2005). The parameters controlling the introduction of current become increasingly important. To minimize damaging effects, charge injection waveform parameters must be carefully considered.

Current injection is typically used to stimulate tissue as it maintains a consistent charge delivery despite variations in tissue impedance (Tsui, 2008). The safety and efficacy of this

stimulation depends largely on the parameters of the applied waveform. Pulses of electric stimulation can be delivered in either monophasic or biphasic shapes.. Monophasic stimulation involves the application of short duration pulses of constant current. Biphasic waveforms are typically charge balanced with cathodal and anodal phases of equal charge per phase such that there is no net charge delivered (Cogan, 2008). The leading or activating phase is used to elicit a response, and a following or reversal phase is used to remove the injected charge, and reverse electrochemical processes occurring during the stimulating pulse. Common practice uses a cathodal pulse for stimulation and an anodal pulse for reversal (Merrill et al., 2005). Although monophasic pulses are highly efficacious in action potential initiation and result in minimal electrode corrosion, they are not often employed for neural stimulation as it results in a larger degree of tissue damage than biphasic pulses with the same pulse width and frequency (Merrill et al., 2005).

A variety of waveform shapes have been proposed to balance excitation with damage. Arbitrary pulse shapes can be used; however, the application of rectangular pulses is common practice. Stimulation can be either cathodal or anodal. Cathodal stimulation activates tissue close to the electrode site and inhibits activation distant to the electrode site. Anodal stimulation creates a “virtual electrode” and activates tissue farther from the electrode and inhibits activation at the electrode surface (Cogan, 2008). Monophasic waveforms readily activate excitable tissue but are known to cause more tissue damage. Biphasic stimulation uses an activating phase followed by a reversal phase, which removes the charge from the tissue and is known to reduce tissue damage in comparison to monophasic stimulation, despite the higher amplitudes to activate tissue. Biphasic waveforms can either be cathodal- or anodal first, and are typically charge balanced, which means the product of the amplitude and the phase duration for the reversal phase is equal to that of the activating phase. A charged imbalanced biphasic applies an activating stimulus followed by a smaller amplitude reversal stimulus. The result is reduced tissue damage, compared to a monophasic waveform, and improved excitation capacity compared to charge balanced biphasic waveforms (Merrill et al., 2005; Cogan, 2008). Additional improvements to charge balanced stimulation have been seen with the addition of an interphasic delay or asymmetric stimuli. The interphase delay places a gap between the activating and reversal phases. The prolonged duration

before the stimulation is removed allows for increased tissue excitation, while the reversal still occurs within a short enough timeframe to ease damaging reactions (Merrill et al., 2005). An asymmetric waveform maintains charge balance by reducing the amplitude and increasing the pulse duration of the reversal phase of stimulation. The effect is rapid charge injection followed by a slower removal of charge.

Pulse duration and pulse frequency directly factor into the current density and charge per phase, the two primary determinants of tissue excitation and damage. The range of tissue excited by stimulation is thought proportional to charge per phase, while the proportion of cells excited within that range is modulated by the charge density (Merrill et al., 2005). The charge per phase *Q* is the product of the current intensity *I* and the duration of the pulse *W*. The charge threshold needed to evoke a response can be determined by applying this relationship to the threshold current:

$$\mathrm{b}Q_{th} = I_{th}W \tag{1.2}$$

A relationship also exists between the current threshold to activate tissue and the duration of an applied pulse such that the threshold decreases with increasing pulse width. The minimum constant current capable of initiating an action potential at a theoretically infinite pulse width is called the rheobase current. This relationship can be characterized by strength-duration curves, and mathematically by:

$$I_{th} = \frac{I_{rh}}{1-e^{-W/\tau m}} \tag{1.3}$$

where I_{th} is the threshold current, I_{rh} is the rheobase current, W is the pulse width, and τ_m is the membrane time constant (Merrill et al., 2005). The figure below summarizes the current and charge response to pulse width. The relationship between pulse width and threshold current or charge can be used to determine requirements for efficacious stimulation. Taking into account the increasing charge requirements with pulse duration and the relation between charge per phase and damage thresholds, a narrow pulse width should be maintained to minimize electrochemical reactions occurring at the electrode surface.5

CHAPTER 2

DISCRETE DECODING OF ARTICULATE MOVEMENTS IN HUMAN PATIENTS USING EPICORTICAL MICRO-ELECTRODES

ABSTRACT

Neural trauma or pathology can leave patients with limited means for communication and interaction with their environment. For these individuals, a direct cortical interface may provide rapid and intuitive control of communication or motor prostheses. Multiple studies have demonstrated that neural prosthesis can be controlled using intracortical micro-electrode arrays and epicortical electrocorticography grids. We implanted epicortical micro-electrocorticography grids over cortical areas involved in the control of articulate movements and demonstrate that such movements could be decoded from local field potentials recorded on these non-penetraing microelectrode grids. Articulate movements were classified from cortical local field potentials using a multiclass support vector machine. Using local field potentials recorded from face-motor cortex, ten words and silence were classified with and accuracy of 85.6%. Using local field potentials recorded from hand-motor cortex, three individual finger movements and rest were classified with an accuracy of 72.3%. These findings demonstrated that LFPs recorded by non-penetraing microelectrode grids contain sufficient information to classify articulate movements associated with speech or individual finger movements and could serve as the basis for a communication prosthesis for locked-in patients.

INTRODUCTION

Severe paralysis from conditions like spinal cord injury (SCI), Amyotrophic Lateral Sclerosis (ALS) or subcortical stroke can leave patients unable to communicate or interact with their environment in a condition known as locked-in syndrome(Smith & Delargy, 2005). Some patients with locked-in syndrome depend on small residual movements for slow, basic communication and physical interaction with their environment. This is often slow and requires considerable mental effort(Birbaumer, Ghanayim, & Hinterberger, 1999; Majaranta & Räihä, 2002). Directly interfacing with the cortex may provide more rapid and intuitive control over communication

or motor prostheses(Birbaumer et al., 1999), which has potential to dramatically improve patient quality of life. Therapeutic BCI systems transform neural activity related to intended movements into control signals for communication systems or assistive devices. Ideally, the neural activity will be acquired with the highest spatiotemporal resolution possible, while using the most minimally invasive electrodes to provide rapid, intuitive, and reliable control.

A variety of electrode types and recording methodologies have been evaluated for the use in BCIs including non-invasive techniques. Electroencephalography (EEG) is typically used because of its non-invasive electrode placement on the scalp. Functionality is generally limited due to a range of surface artifacts and the poor signal quality(T. Ball et al., 2008; Tonio Ball, Kern, Mutschler, Aertsen, & Schulze-Bonhage, 2009). EEG based BCI applications are dependent on event related potentials (ERPs) or learned control over lower frequency signals, which limits potential applications and require focused attention and effort to use(Padmavathi & Ranganathan, 2008). Despite improvements from advanced signal processing techniques(Kevric & Subasi, 2017; Kottaimalai, Rajasekaran, Selvam , & Kannapiran, 2013; Lange, Low, Johar, Hanapiah, & Kamaruzaman, 2016; Wen, Jia, Lian, Zhou, & Lu, 2016), EEG is unlikely to provide natural and intuitive control over a BCI system because of its low spatial and temporal resolution(Wolpaw, Birbaumer, McFarland, Pfurtscheller, & Vaughan, 2002).

Electrocorticography (ECoG) arrays have large (> 1 mm diameter) subdural electrodes and are used clinically to map cortical function and locate an epileptic focus prior to resection. ECoG has become common in BCI studies because of its clinical ubiquity in preparing patients for the surgical treatment of epilepsy. Because of the epicortical placement close to the physiological source, ECoG has higher spatial resolution and signal to noise ratio, broader bandwidth, and is subject to fewer physiological artifacts than EEG(Buzsaki, Anastassiou, & Koch, 2012; Cooper R, 1965; E. Leuthardt, Miller, Schalk, Rao, & Ojemann, 2006). Neural activity recorded from ECoG electrodes has been used in the classification of spoken words or phonemes (Blakely, Miller, Rao, Holmes, & Ojemann, 2008; Chang et al., 2010; Wang, Degenhart, Sudre, Pomerleau, & Tyler-Kabara, 2011) and classification of finger movements(C. Chestek et al., 2013; Kubanek, Miller, Ojemann, Wolpaw, & Schalk, 2009; K. Miller, Zanos, Fetz, den Nijs, & Ojemann, 2009; Pistohl,

Schulze-Bonhage, Aertsen, Mehring, & Ball, 2012). Using chronically implanted ECoG arrays in non-human primates 3-dimensional hand positions have been able to accurately predicted for several months(Chao, Nagasaka, & Fujii, 2010). ECoG electrodes are typically several millimeters in diameter with inter-electrode spacing on the centimeter-scale. With this geometry, recordings in human motor cortex are limited to signals being modulated by movements on only one or two electrodes(E. Leuthardt, Schalk, Wolpaw, Ojemann, & Moran, 2004; V Menon et al., 1996). Additionally, ECoG grids spatially integrate and under-sample the information represented at the scale of cortical columns (E. Leuthardt et al., 2004; V Menon et al., 1996).

High-impedance microelectrodes have small recording surfaces and acquire neural signals with high spatial resolution(Tsanov et al., 2011). Therefore, microelectrode arrays can have smaller inter-electrode spacing and avoid the issue of under-sampling cortical activity. Intracortical microelectrode arrays have been evaluated for use in neuroprosthetics as they can record both action potentials (APs) from individual neurons and local field potentials (LFPs) from small groups of neurons. While the spatial extent of LFPs is debated, they likely represent coordinated neural activity of cortical micro-circuits, such as cortical columns(Buzsaki et al., 2012; Mountcastle, 1978). Intracortical microelectrode arrays implanted over motor cortex have been used to rapidly decode continuous motor movements, predict speed and direction, and control computer cursors and prosthetic arms (Collinger et al., 2013; Gija et al., 2012; Golub, Yu, Schwartz, & CHase, 2014; Hochberg et al., 2006; Kim et al., 2011). Fewer studies have been conducted in which penetrating arrays are placed in language areas, however, intracortical arrays have been successfully used to decode phonemes (Brumberg, Wright, Andreasen, Guenther, & Kennedy, 2011). Intracortical arrays penetrate into the parenchyma of the brain and violate the blood-brain barrier causing local tissue damage and cellular disruption (Fernández et al., 2014). AP recordings, which may last for years, do eventually degrade limiting the functional lifetime of these BCI systems (Barrese et al., 2013; Simeral, Kim, Black, Donoghue, & Hochberg, 2011).

Epicortical microelectrode arrays, which use submillimeter electrode diameters and millimeter-scale inter-electrode spacing, were designed to record LFPs at high spatiotemporal resolution with an invasiveness equivalent to ECoG. The electrodes in these micro-

electrocorticography (micro-ECoG) arrays have a small surface area and high impedance and therefore record local field potentials rather than the macro-scale field potentials recorded on ECoG grids (Schalk & Leuthardt, 2011). Unlike intracortical microelectrode arrays, LFPs recorded from the surface of the cortex and may be less prone to signal degradation over time (Schendel et al., 2013). The smaller inter-electrode spacing of non-penetraing microelectrode grids provides the ability to sample the closely spaced areas of motor cortex that control different movement (C. Chestek et al., 2013; C. A. Chestek et al., 2013; Crone, 2006; Freeman, Rogers, Holmes, & Silbergeld, 2000; J. Kim, J. Wilson, & J. Williams, 2007; J. Kim, J. A. Wilson, & J. C. Williams, 2007; E. Leuthardt, Z. Freudenberg, D. Bundy, & J. Roland, 2009; E. C. Leuthardt, Z. Freudenberg, D. Bundy, & J. Roland, 2009; V Menon et al., 1996; V. Menon et al., 1996; K. J. Miller et al., 2007; M. Slutzky, Jordan, & Miller, 2008; M. W. Slutzky et al., 2010; Van Gompel et al., 2008; Worrell et al., 2008). Micro-ECoG arrays have shown promise for decoding speech (S. Kellis et al., 2010; E. C. Leuthardt et al., 2011), arm movement (S. S. Kellis, House, Thomson, Brown, & Greger, 2009) and basic hand movements (E. C. Leuthardt et al., 2009). This work builds upon and extends previous studies in which similar micro-ECoG grids have been shown to support high temporal- and spatial-resolution recordings for BCI-like applications (S. Kellis et al., 2012; Spencer Kellis et al., 2010; S. S. Kellis et al., 2009). The following study evaluates simple, discrete decoding to discern articulate and fine motor movements from micro-ECoG recordings, to support the case of BCIs interfacing at the cortical surface with micro-scale electrodes. It further evaluates the spatial decay of signal overlap with neighboring electrodes in consideration of optimal electrode density.

METHODS

Subject and Grids. Data was generated from human subjects undergoing clinical ECoG monitoring for medically refractory epilepsy in collaboration with the Department of Neurosurgery at the University of Utah under Institutional Review Board approval. Four patients were implanted with micro-ECoG grids (PMT Corporation, Chanhassen, MN and Ad-Tech Medical Instrument Corporation, Racine, WI; Table 2.1). Patients A was implanted with grids manufactured by PMT Corporation that consisted of 40 μm diameter platinum wire electrodes embedded in a thin layer of

silicone. Each wire terminated in a cylindrical protuberance that extended approximately 200 μm above the base of the grid (Figure 2.1) with 1mm inter-electrode spacing. Patient A was implanted with two 16 channel grids with 1 mm inter-electrode spacing over putative Wernicke's area (posterior aspect of the superior temporal gyrus) and face-motor cortex. Patients B, C, and D, were implanted with grids over hand-motor area manufactured by Ad-Tech Medical Instrument Corporation that consisted of 50 μm diameter platinum wire electrodes embedded in a thin layer of silicone. Each wire protruded above the base of the grid by approximately 80 μm with 3 mm inter-electrode spacing. Patients B and D were each implanted with a 32-channel grid. Patient C was implanted with a 64-channel. All grids were placed epicortically. Reference and ground were low impedance wires placed in the epidural space, nearest ECoG electrode, or an EEG electrode. Clinical constraints determined final electrode grid, reference, ground placement, and task.

Table 2.1

Patient and Grid Information

Subject	Sex	Task	Grid	Reference & Ground
A	M	Speech Arm Movement	PMT 2X16 channels 40 μm, 1-mm spacing	Epidural wires
B	F	Arm Movement	PMT 30 channels 40 μm, 2-mm spacing	On-grid low impedance electrodes
C	M	Finger Flexion	Ad-Tech 64 channels 50 μm, 3-mm spacing	EEG electrodes
D	M	Finger Flexion	Ad-Tech 32 channels 50 μm, 3-mm spacing	Nearest Subdural ECoG electrode EEG electrode
E	M	Finger Flexion	Ad-Tech 32 channels 50 μm, 3-mm spacing	Nearest Subdural ECoG electrode Epidural ECoG electrode

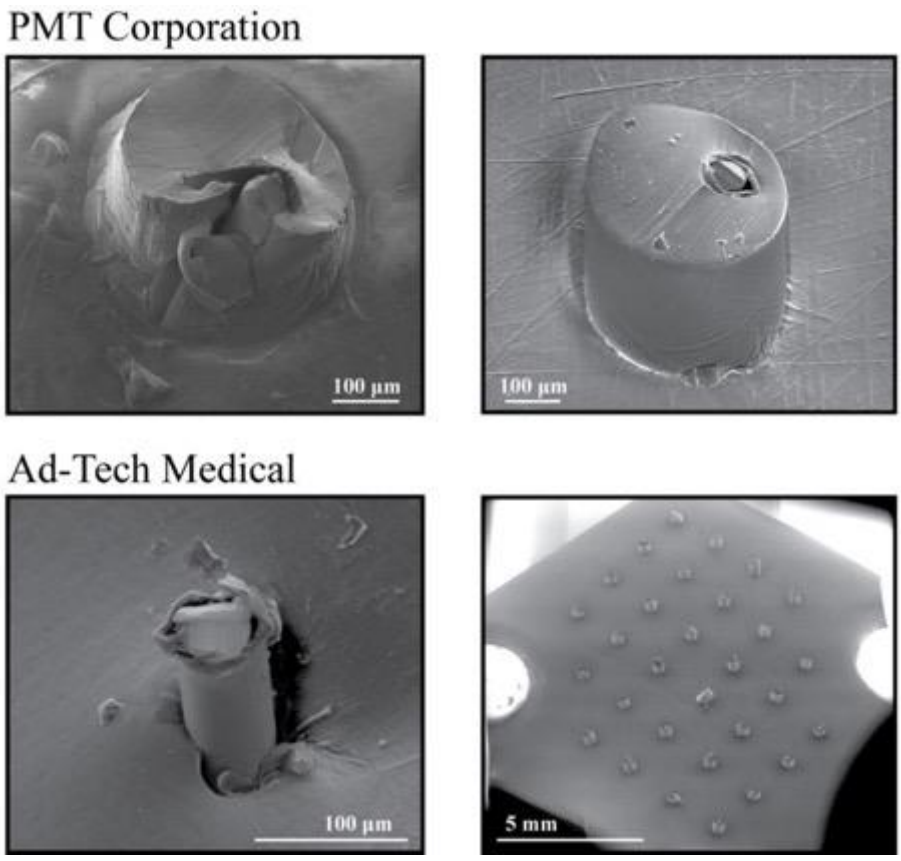

Figure 2.1. SEM pictures of micro-ECoG grids. Patients A and B were implanted with micro-ECoG grids manufactured by PMT Corporation. Each wire terminated in a cylindrical protuberance that extended ~200 µm above the base of the grid. Patients C and D were implanted with micro-ECoG grids manufactured by Ad-Tech Medical. Each wire protruded above the base of the grid by approximately 80 µm.

Experimental Paradigm and Data Acquisition. All behavioral and neural data was recorded with a NeuroPort system (Blackrock Microsystems, Salt Lake City, UT). A microphone recorded the patient's speech. Finger movement was monitored with three pressure sensors (Liberating Technologies, Holliston, MA). A task control system (LabVIEW, National Instruments, Austin, TX) was used to visually cue patients.

For the speech task the patient was verbally instructed then visually cued to repeat a given word multiple times with approximately one second intervals between trials. This was repeated for each of the ten chosen words at least once per session. The word list consisted of "yes", "no", "hot", "cold", "hungry", "thirsty", "hello", "goodbye", "more", and "less". Data was collected in multiple sessions across several days. Additional details regarding this experimental can be found in

previously published work{Kellis, 2010, Decoding spoken words using local field potentials recorded from the cortical surface}. The results presented here re-analyze this previously published speech data using different signal features and a different decoding algorithm. For the finger flexion task, the task control system visually cued patients to randomly flex their index, middle, and ring finger on the hand contralateral to the implanted electrodes.

Neural activity and speech were recorded at 30 kHz. Patients C, D, and E performed the finger flexion task. The task control system was used to cue all movements. Neural data was recorded at 10 kHz and behavioral data was recorded at 2 kHz. Neural and hand position or speech data were down sampled to 5 kHz (Patient A) or 2 kHz (Patients C, D, and E) to reduce data size for analysis. The neural data was also high-pass filtered at 1 Hz.

Data Analysis and Feature Extraction. Snippets of non-penetraing microelectrode data were generated for each trial by aligning the recorded voltages to the onset of intonation for speech or to the movement cue for the finger flexion. Speech trial snippets were created from the 100 ms preceding speech onset to 400 ms following onset. Trial snippets for the finger flexions were created from the 100 ms preceding the cue to the average time duration of the finger movements for each patient. For both the speech and finger flexion decode, three feature sets were evaluated as inputs to the decode algorithm.: 1) Time domain - The voltage time series was normalized across all trials for each channel, filtered (1-500Hz), and then downsampled to 500 Hz, 2) Frequency domain - The power spectra for each trial and channel were calculated for frequencies between 1-500 using the Chronux package (http://chronus.org) and log normalized, 3). Combined time and frequency domain – Both time and frequency domain features were concatenated for each trial (Figure 2).

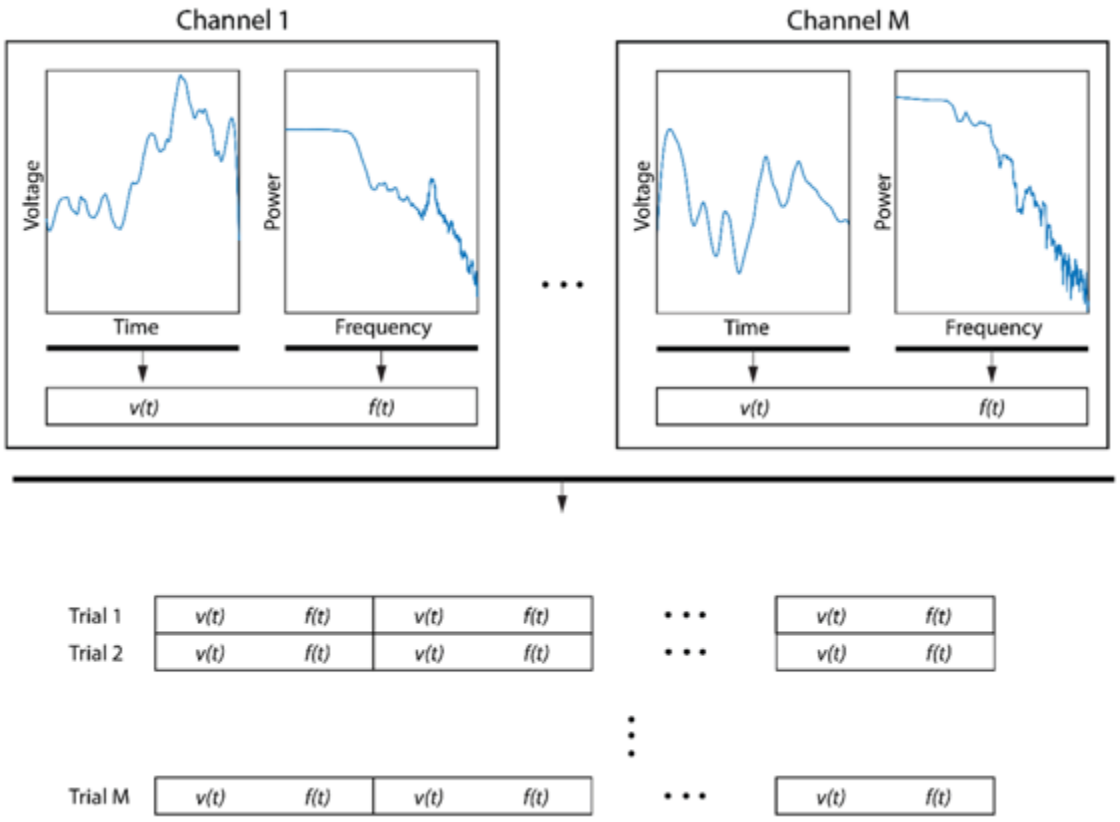

Figure 2.2. Time and frequency domain feature sets. Frequency domain features, generated by calculating power spectra for each trial and channel, were concatenated with downsampled voltage features for each trial. Trials were unwrapped to contain a vector of information for each channel and trial.

Discrete Decoding. Speech and finger flexion decoding was performed on the time, frequency, and combined feature sets using a support vector machine (SVM) classifier with radial basis function kernel. SVM models were constructed for each class and combination using a one-versus-one multiclass implementation. In this setting a binary classifier is created for each possible pairing in the training set. The decode features are passed through each classifier with the class selected most often given as the final prediction. A radial basis function (RBF) kernel was employed with parameters c and gamma optimized using leave-one-out cross validation and minimizing k-fold loss. For each implementation of the classifier, the same amount of trials was used to train and validate testing performance. Validation trials were novel to the classifier and different than those used in training for any case presented. For the speech dataset recorded from Patient A, 40 trials

per spoken word class were used to train the classifier with 40 additional used to verify the outcome. Predictive accuracy was analyzed for each array individually as well as performance with all 32 channels. The dataset from Patient C used 64 channels and 38 trials per flexion class to train and 38 new trials to test. For Patient D, 32 channels were used, with 35 trials per flexion class used to train and an additional 35 trials used to test the classifier. The finger flexion dataset derived from Patient E employed all 32 channels and used 40 trials per flexion class to train and 40 trials to test. Trials used for training and decoding were randomized to reduce the potential temporal bias of directly neighboring trials. Classification for the speech data consisted of eleven classes, one for each of the ten spoken word classes and an additional "silence" class. Classification for finger flexion sets consisted of four stats, one each for "index", "middle", and "ring" fingers and an additional non-movement state.

Discrete Decode Evaluation. Classification accuracy was measured against the level of chance, which was determined by assuming a uniform distribution for each class assignment. Classification accuracies above the level of chance indicates that the LFP features applied to the classification were correlated to the behavior measured. Confusion matrices were also computed for classification decodes. Each value on a given row and column of a confusion matrix represents the normalized number of times that a class was predicted by the decoder. If the decoding is perfect, the confusion matrix should be an identity matrix, i.e. have entries equal to one along the main diagonal and zero everywhere else.

Continuous Decode of Arm Movement. For the continuous decode of arm movement, different types of LFP features were selected as the decode input to explore dynamics in the time domain as well as the time varying power in the frequency domain. To examine the time domain, the voltage time series was averaged for each 100 ms time bin. LFP multi-taper spectra were generated using the Chronux package and were log-normalized across trials for each channel. To examine the time varying frequency domain, the spectral power at 1-5 Hz, 10-15 Hz, 25-30 Hz, 50-55 Hz, 100-105 Hz and 250-255 Hz was estimated for each 100 ms time bin. Frequency bands were chosen because the spectrogram of the raw data showed increased power with arm movement distributed between 1-255 Hz.

To continuously decode arm movement, a standard Kalman filter was implemented. The likelihood model was defined as:

$$z_k = H_k x_k + Q_k \quad (2.1)$$

where H_k linearly relates the arm kinematics x_k to the LFP features z_k. Q_k represents noise in the observation, assumed to be zero-mean and normally distributed. The final feature vector z_k consisted of LFP features for each channel.

$$x_k + 1 = A_k x_k + W_k \quad (2.2)$$

The state transformation matrix A_k was defined to model how the arm kinematics, varied over time, with W_k, a noise term, also assumed to be zero-mean and normally distributed. The arm kinematic state x_k comprised of x and y position, velocity, and acceleration for k = 1, 2, ... M, where M was the number of time bins in the data set. The parameters A, H, W, and Q were directly calculated from the training data as described in {Wu, 2006, Bayesian population decoding of motor cortical activity using a Kalman filter} and were assumed to be constant, e.g., $A_k = A$.

The LFP and arm kinematic data was segmented into 100 ms time bins and the decode updated the estimated position each 100 ms time bin. The Kalman filter was performed with z_k as the time domain features and the time varying frequency domain features separately and in combination. An offset of 200 ms was introduced between the movement data and the LFP feature set to account for the delay between neural activity and motor output. The Kalman filter was trained and then tested on subsequent non-overlapping segments of data.

For Patient A, the LFP features were selected from 32 channels. The training set was 112 seconds long (31 reaches) and the testing set was the subsequent 89 seconds (25 reaches) after 225 seconds of the patient resting. For Patient E, the LFP features were selected from 30 channels. The training set was 55 seconds long (19 reaches) and the testing set was the subsequent 65 seconds (28 reaches) after 15 seconds had passed. For Patient C, the LFP features were selected from 64 channels. The training set was 180 seconds (70 reaches) long and the testing set was the subsequent 180 seconds (68 reaches). For Patient D, LFP features were selected from 26 of the 32 channels. The training set was 180 seconds long (52 reaches) and the testing set was the

subsequent 120 seconds (36 reaches). For Patient B, LFP features were selected from 30 channels. The training set was 120 seconds (20 reaches) long and the testing set was the subsequent 120 seconds (25 reaches).

For Patient C, the Kalman filter was also implemented online in real-time. LFP and kinematic data were segmented into 100 ms time bins, with an offset of 200 ms between neural data and kinematics. 18 channels were selected for the decode. These channels were chosen because the LFPs demonstrated the highest correlation coefficient with arm movement. For the selected channels, spectral data in the beta band, 20 to 30 Hz, was averaged. The beta band was selected because there was a visual increase in power between 20 to 30 Hz when the patient made reaching movements. For other studies decoding arm movement, power in frequencies above 100 Hz has been shown to have higher mutual information with kinematic data, but power in the beta band had a moderate value of mutual information with the kinematic data {Zhuang, 2010, Decoding 3-D reach and grasp kinematics from high-frequency local field potentials in primate primary motor cortex}. The decode was trained using one minute of data. The position of the cursor during online decoding was restricted within the space of the tablet and monitor, but no algorithmic constraints were applied to trajectory. Patient C received visual feedback while the task control system updated the cursor position based on the Kalman filter output every 100 ms. A trial was considered successful immediately after the patient crossed the perimeter of the 50 mm diameter target. The target remained on until the trail was successful.

Task-specific signal spatial decay. A cross correlation-based analysis was conducted to evaluate whether micro-ECoG arrays over sample neural activity, particularly in a task-specific contex. Signal similarity across electrodes was evaluated by calculating the normalized cross correlation for each electrode pairing on a given array for broadband signals (0-500Hz), as well as within each frequency band associated with neural activity, delta (0-4Hz), theta (4-8), alpha (8-12), beta (12-30), gamma (30-80), chi (80-150), and two high frequency (150-300Hz and 300-500Hz). The maximum coefficient was used as the metric for each pairing. Samples were taken from the trial windows used in classification for two 16 channel arrays from Patient A and one 64 channel array from Patient D, with maximum values averaged across all trials and by category. Within an

array, coefficients were grouped by distance from the source electrode to determine general trends. This analysis was used to evaluate the spatial dynamics of signal similarity at the millimeter range of high density µECoG arrays.

RESULTS

Discrete decode.

Spoken word decode.

Feature sets. Combining features from the time and frequency domain improved performance relative to using either feature set alone. The time domain feature set yielded a median accuracy of 91.67% for two-word pairs and 66.06% accuracy for eleven words. Frequency domain features increase accuracy for two-word pairs to 95% and 67.58% for eleven simultaneous words. Using LFP features from both time and frequency domain increased classification accuracy to 98.33% for two-word classes and 85.45% for eleven categories (Figure 2.3). In all cases, the median accuracy for each number of simultaneous classes was above chance level. Two population t-tests conducted for each number of simultaneous classes between either the frequency-only and time domain-only feature sets against the combined feature sets revealed significant population differences in decode performance ($p<.01$). The confusion matrix shows the number of times each word or silence was predicted from the frequency and time domain features (Figure 3D). The word “no” was classified with the highest accuracy (97.67%), followed by “yes” and periods of silence (93.33%). The decoder performed worst with the word “more” (70%), most often confusing it with “no”.

Electrode/Array Accuracy. Features taken from all electrodes over FMC performed similarly in accuracy to features taken from electrodes over Wernicke’s area. Both Wernicke’s area and FMC electrodes produced a median accuracy of 95% for two classes, but Wernicke’s area held 69.39% accuracy to the 63.64% accuracy rate for eleven classes (Figure 2.3B).

Frequency bands. Of the frequency bands analyzed delta, theta, gamma, and chi were consistently above chance for each number of simultaneous classes. The frequency bands that held the highest ability to consistently classify words were gamma, with 84.82% for two classes

and 50.61% for eleven classes, and chi, with 91.33% accuracy for two classes and 60.3% for eleven classes). High LFP bands consistently yielded better decode accuracy, with accuracy falling off at higher and lower frequencies (Figure 2.3C).

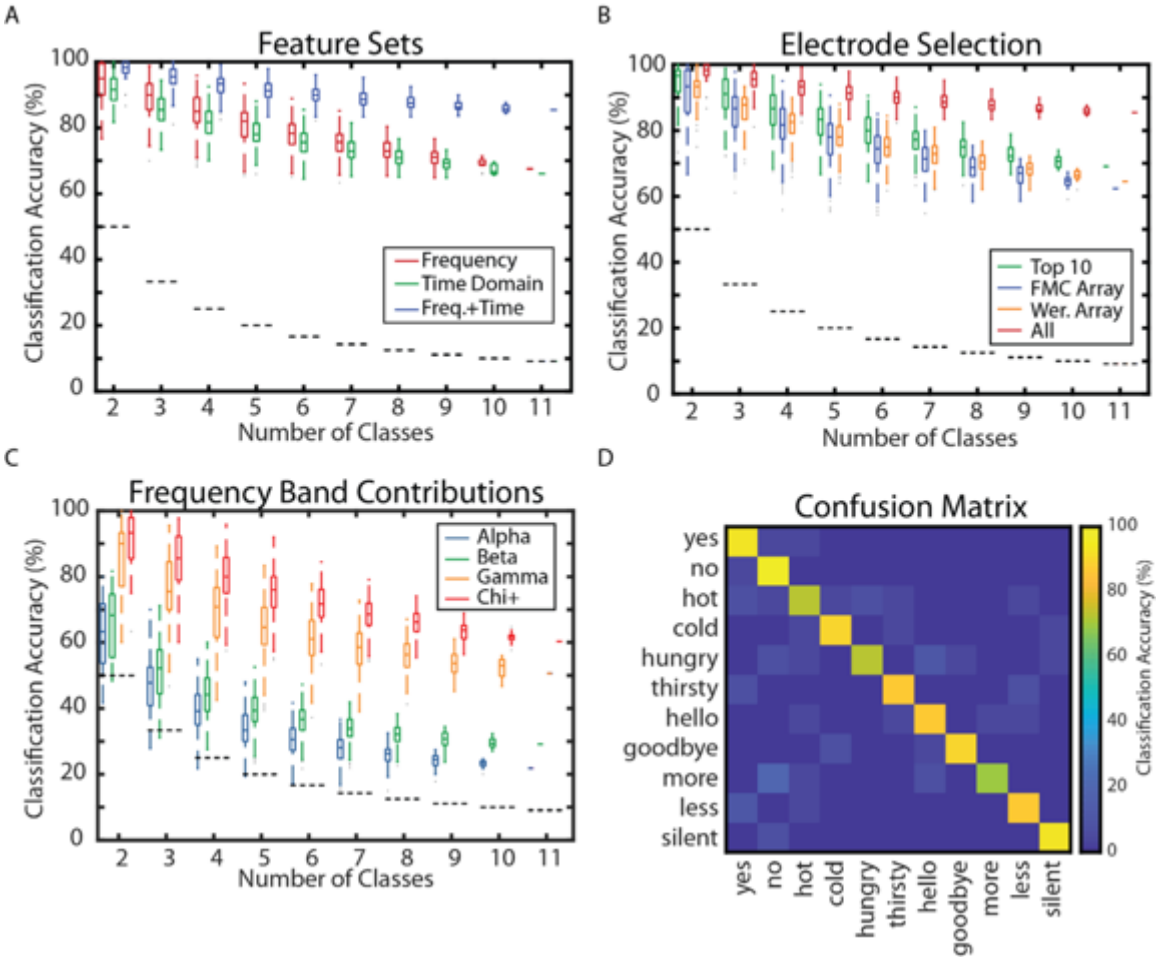

Figure 2.3. Comparing classification performance for each feature set, electrode group, and frequency band for two through eleven classes (Patient A). (A) Decode accuracy based on feature set. Time and frequency domain feature sets produced equivalent accuracies, combined features showed significant increase in reliability in cases with seven or more concurrent categories. (B) Features taken from each array provided decodes significantly above chance. Features taken from all active electrodes provided highest accuracy. (C) each frequency band contained sufficient information to represent each spoken word above chance. The frequency bands that most accurately correlated with each spoken word were Gamma (40-80 Hz) and a wide band high frequency (80-300 Hz). Decodable information was present in higher frequencies, however the contribution was significantly lower. (D) Confusion matrix for the spoken word decode of eleven simultaneous classes, using combined features and all channels from each array (FMC and Wernicke's area). The words "hot", "hungry", and "more" were the least accurately classified.

Finger flexion classification. For finger flexion classification, combining features from the time and frequency domain improved performance relative to using frequency domain features, but not compared to time domain features. Statistically significant population differences using a 2-smaple t test were noted for each patient for classes 2-4, between accuracy from the frequency feature decode and the combined feature decode ($p = .05$). The decode performed on the data from Patient D for two classes of finger flexion had a median classification rate of 80% with time domain features, 76.67% for frequency domain features, and 83.33% for combined features. Median decode performance with four simultaneous features was 70.83% for time domain features, 65% for frequency domain features, and 73.33% for combined features (Figure 4A). For Patient B, the accuracy for four classes of movements was 45% using time domain features, 40.83% using frequency domain features, and 53% using combined features. For Patient C, the decode accuracy for four states of movements was 47.37% with time domain features, 42.24% with frequency domain features, and 52.63% using both time and frequency domain features. While results tended to have higher mean and median accuracy for combined feature sets, results were not considered statistically significant. For each patient and feature set, the median classification rate was above the rate of chance. The confusion matrix in Figure 4B shows rate at which each movement was predicted by the decoder using combined features for Patient D. Middle finger flexion was the most accurately classified (88.33%), while ring finger flexion had the lowest classification accuracy (74.4%). Results for each subject and feature set tested are presented in Table 2.2 below.

Table 2.2

Four-Class Decode Accuracy of Finger Flexions

		Subject			
		B	C	D	Chance
Feature	Time	45.00%	47.37%	80.00%	25%
	Frequency	40.83%	42.24%	76.67%	25%
	Combined	53.00%	52.63%	83.33%	25%

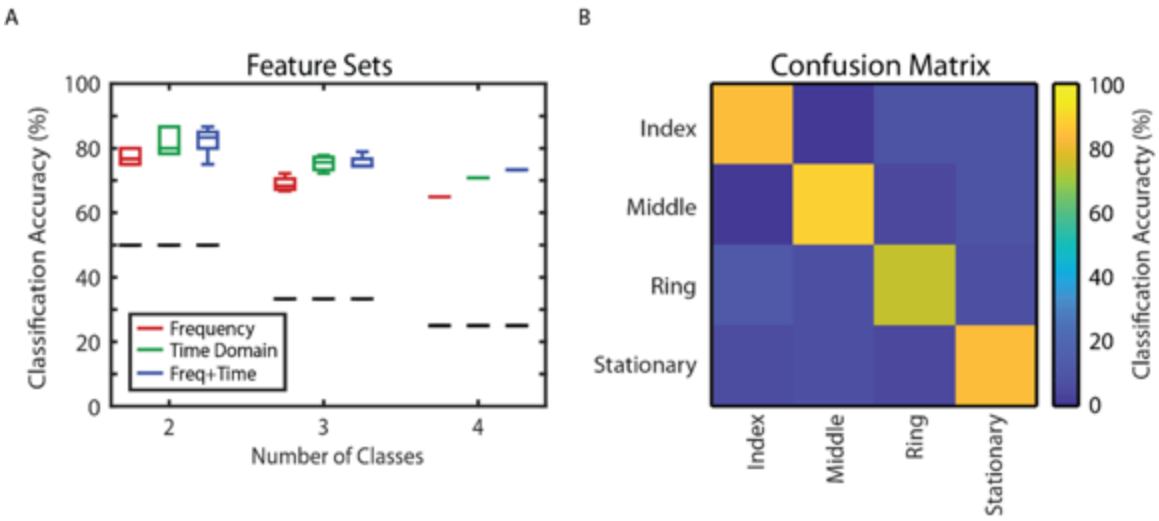

Figure 2.4. Classification performance for each feature set used to simultaneously classify finger flexion for two through four finger movements (Patient D). (A) Classifier performance using time, frequency, and combined features to simultaneously decode two through four classes of finger flexion. The combined feature set provided the highest accuracy. (B) Confusion matrix for four simultaneous classes, using combined features and all 32 channels.

Continuous arm movement decode.

Offline decode. For the continuous decode of arm movement, the performance of the decode was quantified offline by calculating the correlation coefficient between the actual arm position, velocity and acceleration and the estimated arm position, velocity and acceleration. Applying LFP features from both the time and frequency domain, the Kalman filter decode was able to estimate the arm movements for Patient B with the highest correlation (Figure 5). The estimated position and the actual position of the arm had correlation coefficients of 0.82 in the X direction and 0.76 in the Y direction. The estimated velocity and the actual velocity of the arm had correlation coefficients of 0.45 in the X direction and 0.51 in the Y direction. The estimated acceleration and the actual acceleration of the arm had correlation coefficients of 0.10 in the X direction and 0.32 in the Y direction. Using LFP features from the time and frequency domain, the decode performed well above chance for X and Y position, velocity, and acceleration for all patients (Table 2). The correlation coefficients between the actual and estimated kinematic variables were averaged together to compare decode performance for the three possible LFP feature sets (time, frequency, and time-frequency). Combining features from the time and frequency domain improved performance slightly from using only the time domain or frequency domain features (Table 2.3).

The decode had the lowest correlation coefficients for Patients A and E which may be due to a less ideal positioning of the grid over the arm area of cortex or decreased contact with the cortex.

Table 2.3

Correlation Coefficients Between Actual and Estimated Arm Kinematics For All Patients.

	A	B	C	D	E	Chance
X Position	0.32	0.82	0.66	0.53	0.35	0.10
Y Position	0.39	0.76	0.54	0.45	0.25	0.12
X Velocity	0.17	0.45	0.43	0.39	0.30	0.09
Y Velocity	0.32	0.51	0.36	0.36	0.16	0.05
X Acceleration	0.12	0.10	0.40	0.19	0.16	0.03
Y Acceleration	0.20	0.32	0.21	0.08	0.10	0.03
Average (time + frequency domain)	0.25	0.49	0.43	0.33	0.22	0.07
Average (time domain)	0.18	0.31	0.41	0.24	0.13	0.07
Average (frequency domain)	0.24	0.39	0.32	0.24	0.16	0.07

Online decode. For the online experiment, Patient C controlled the movement of a computer cursor via motor imagery using the real-time Kalman filter. The patient moved the cursor between two targets, which were visually cued for 21 minutes (Figure 2.6). The patient required a median of 2.15 seconds (Interquartile Range of 3.78) to start moving in the direction of the target, and a median of 6.24 seconds (Interquartile Range of 14.29) to acquire each target. All presented targets were successfully reached since the task condition set was for the target to remain visible reached.

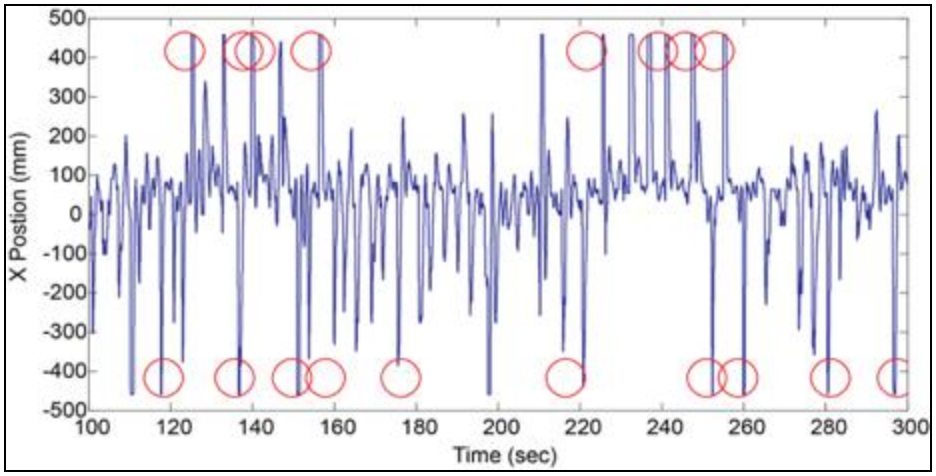

Figure 2.5. X position of a computer cursor controlled by Patient C with a real-time Kalman filter decode on LFP data. A 300-second representative sample of performance of the real-time Kalman filter decode is shown. The blue line represents the x position in millimeters of the cursor as Patient C was randomly cued to move to two targets (red circles) horizontally separated on the monitor. A single feature was used from 18 channels, consisting of the average power between 20 and 30 Hz. The real-time Kalman filter was trained on 60 seconds of data and was implemented with 100 ms time bins and a 200 ms time lag.

Task-specific cross correlation and spatial variation. To evaluate whether non-penetraing microelectrode arrays over sample neural data and whether this interface operates at an appropriate scale for fine motor prosthetics, cross correlation analysis looked at three different arrays across two scales of inter-electrode spacing evaluated for patients A and C across frequency bands typically analyzed in electrophysiology regimes. Patient A was implanted with two 16 channel arrays (A1 and A2) with 1 mm spacing. Patient D was implanted with one 64 channel array (D1) with 3 mm inter-electrode spacing. Arrays A1 and A2 had similar trends of decay with distance and increasing frequency. Lower frequency signals, 0-4Hz and 4-8Hz showed the least decay over distance, with the correlation coefficient dropping to 0.95±0.003 and .93±0.001 respectively for A1 and 0.95±0.002 and .94±0.001 for A2 at 4 mm. Higher frequency signals decayed more rapidly over the same space, with 150-300 Hz dropping to 0.51±.08 for A1 and 0.53±.08 for A2 by 1 mm of separation and further to 0.33±0.01 and 0.33±0.02 by 4 mm of separation (Figure 2.6A-B). Array D1 also had a general trend of correlation decreasing with distance, but had a less linear relation with frequency (Figure 2.6A-B). This array held the strongest correlation with signals in the frequency range of 80-150Hz, with a correlation of 0.84±0.47 at 3mm of separation and 0.71±0.001

at 30 mm, with a peak of 0.81±0.46 at 22 mm. The lowest frequency band at 3 mm was 0-4Hz with an average coefficient of 0.59±0.10 and the lowest band at 30 mm was 00-500Hz with 0.34±0.008. The broadband signal correlation (0-500Hz) showed a similar decay for overlapping distances between arrays A1-2 and array D1, with D1 continuing the trend of decreasing correlation with distance. Minimum values for broadband signal correlation observed on A1 and A2 were nonlinear, but linear for D1, with a slope of 0.009 and intercept of .029±0.01 (Figure 2.6C).

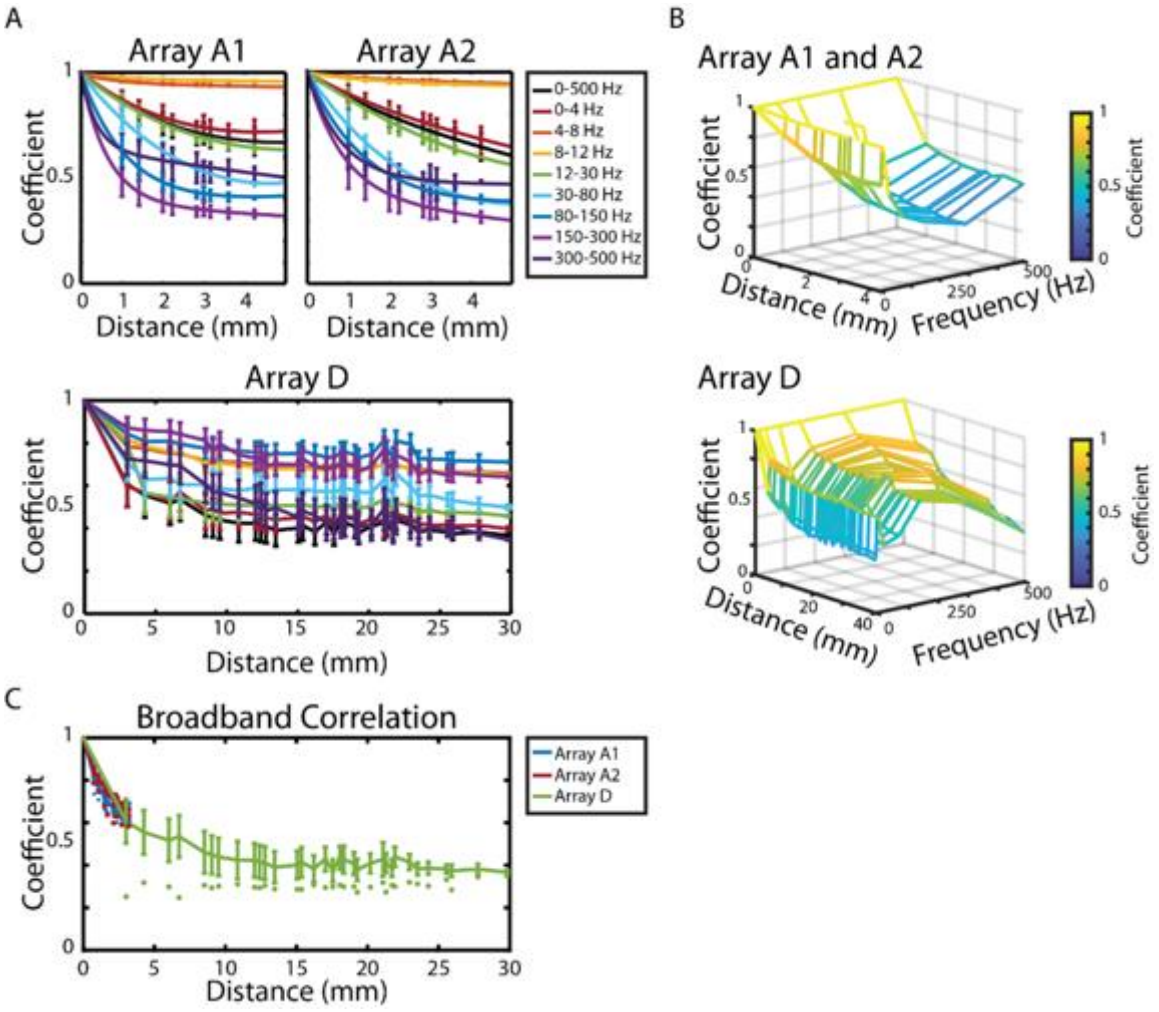

Figure 2.6. Cross correlation for signal spatial dynamics. A. Average cross correlation by frequency band over increasing distance from source for two 16-channel, 1mm interelectrode spaced arrays (A1 and A2) and one 64-channel, 3mm interelectrode spaced array (D). B. Mesh-style representation showing general trends across frequency and distance from source for arrays A1 and A2 (top) and array D (bottom). Arrays A1 and A2 observe rapid decay in correlation with higher frequency signals and slow, steady decrease for lower frequencies. Array D has an initial trend of more rapid decay with distance and increasing frequency, followed by peak between 80-150 Hz, as well as around 30 mm of separation. C. General trends for broadband (0-500Hz) signals across

distance for arrays A1, A2, and D. Arrays overlap and show continuous trend of initial decay followed by plateau. Minimum correlations for each distance are represented by colored dots.

DISCUSSION

This study evaluated whether neural signals recorded from micro-scale surface electrodes could be used to decode articulate movements. Both discrete and continuous decodes were applied with results supporting the use of non-penetraing microelectrodes in BCI applications, with specific examples in decoding spoken words, finger flexions, and hand position. Decode performance was also based on signals evoked with minimal subject instruction or training time. As such, trials captured a range of varied pronunciations in the case of the spoken word task, and variations in the extent of finger position in the flexion task. Greater consistency of intonation by the subject across trials would likely improve accuracy, the level of decode maintained may reflect that the signals collected represented broad enough activity to capture some generalizability but maintain sufficient specificity to correlate with subtle movements. For the online Kalman filter decode, Subject C had minutes of exposure to the decode, with a short duration for training. Performance would likely to improve with more exposure as the patient adapts to the filter (Carmena et al., 2003). However, given the subject was still able to control the cursor despite havening limited exposure, suggests some capacity for intuitive usage. Decoding studies that used neural signals acquired with either EEG or ECoG reported more user training to achieve similar levels of accuracy.

Modulation in LFP gamma band is correlated with motor actuation and is commonly explained as a representation of synchronous processing within cortical columns (Crone, Sinai, & Korzeniewska, 2006; Neuper & Klimesch, 206). Gamma band modulations were expected as activity in this frequency range such has previously been observed and used in decoding a variety of activities, including semantic information (Flint et al., 2014; S Kellis, House, Thomson, Brown, & Greger, 2009; Onaran, Ince, & Cetin, 2011; Wang, Degenhart, Sudre, Pomerleau, & Tyler-Kabara, 2011). The use of both time and frequency domain features increased performance in decoding spoken words, suggesting that combining time and frequency domain features provided additional

independent information to the decode algorithm. The temporal evolution of the signal, particularly the slower oscillations from the frequency components that account for the larger magnitude deflections observed, as well as the broadband frequency components contribute to distinguishing articulate movements.

People comfortably hear and vocalize words in the range of 150–160 words per minute (Williams, 1998). The 500 ms snippets used to classify spoken words translate to a maximum of 120 state selections per minute. This study evaluated up to eleven simultaneous states, with which the classifier performed with an accuracy of 85.45%. The relatively flat shape of the performance curve suggests that decoding a longer list is feasible without a large decrease in performance. In the case of communication prostheses, applying discrete decoding with a more ubiquitous set list, like English phonemes, may allow for a significant degree of linguistic expression. Compared to similar approaches, like thought typing, which either focus on individual letter production or cursor control to select a letter using a virtual keyboard (Vansteensel et al., 2016), discrete decoding approaches may improve on speed and ease of usability, provided classification accuracy can be maintained.

A group of studies using intracortical electrodes has succeeded in maintaining a continuous regression decode based on single unit activity for controlling 3-dimentional movement of a robotic arm or computer cursor (Woodlinger et al., 2015). Accurate 3-dimentional position estimations have been achieved in nonhuman primates and in humans, with some demonstrating more arbitrary and novel control by the user (Collinger et al., 2013). Motor decoding studies have had success in implementing comprehensive regressive systems that can account for arbitrary and complex behaviors; more difficulty has been encountered in continuous language decoding. Studies have been able to moderately regress to passive listening of complex speech patterns, or continuously classify vowel production (Herff et al., 2015). This may be in part to these studies being performed with macro-ECoG, rather than the intracortical microelectrodes employed in those decoding arm position. It is also likely in part do the complexity and intricacy involved in language decoding. Approaching it from a motor-output standpoint, the degrees of freedom expand from the tongue, lips, jaw, and larynx and add to more than the ten DOF achieved several more degrees of freedom

than more than the seven degrees of freedom for the arm (Beautemps, Badin, & Bailly, 2001). A communication prosthesis approach using cursor control and point-and-click methodology rather than regressing on linguistic motor output, and acquiring control signals with intracortical MEAs reported better speed and accuracy (Pandarinath et al., 2017).

Regression approaches typically base analysis on single unit activity due to the density of information the signals contain. However, it has been demonstrated that local field potentials collected with both surface electrodes and intracortical electrodes can support regression based analyses (Degenhart et al., 2018; Stavisky, Kao, Nuyujukian, Ryu, & Shenoy, 2015). This study demonstrated a continuous decode of arm movement using non-penetraing microelectrode-recorded LFPs. Accuracy was lower in comparison to results reported from intracortical studies (Gilja et al., 2012), likely in part due to the recording methodology and to the comparatively less sophisticated decoding approach. Considering other studies have shown success in maintaining high accuracy control during a 3-dimetional cursor control tasks from macro-ECoG recorded LFPs (Degenhart et al., 2018), it is likely refining the decode technique could lead to significant improvements in performance. The information content represented by microelectrode-collected surface LFP is similar in quality and specificity to LFPs recorded by intracortical microelectrodes (S. Kellis et al., 2016; Watanbe, Sato, Nambu, Kawato, & Isa, 2012). It is possible that similar levels of decode performance may be achieved with non-penetraing microelectrodes as intracortical MEAs, while being less invasive.

The cross-correlation analysis reveals discernable millimeter-scale signal variations across the micro arrays, that would be unobservable on larger ECoG arrays. Patterns varied between the 1 mm center-to-center spaced and 3 mm spaced arrays. The smaller, more tightly spaced arrays both showed a general trend of correlation decreasing with both distance and frequency. The gamma and chi bands, which are often used for decoding information, showed low correlation between signals collected as close as 1 mm, indicating separate and potentially meaningful information collected at this scale. Comparatively, the larger array D1 had less generalizable trends in relation to frequency. This may be related to the increased size and coverage area of the 64-channel D1 array as well as correlation being assessed during task specific behavior. Populations

of neurons can become tightly coupled during computation (Cain, Iyer, Koch, & Mihalas, 2016), particularly with higher frequencies in the gamma range. As the larger D1 array covered more cortex, it had a higher likelihood of collecting signals from separate populations of neurons within a linked network, whereas the smaller A1 and A2 arrays maintained a higher level of specificity and reflect more localized population activity. The higher average correlation observed in the gamma band range on D1 array may be explained by the increased range of coverage and comparative sparsity. The minimum correlation observed at each frequency depicts a similar pattern to those observed on A1 and A2. A study evaluating spatial properties of signals collected with different scales of electrode interfaces showed a similar pattern seen with A1 and A2 correlations with coherence decreasing with distance and frequency for non-penetraing microelectrode arrays with a maximum spacing of 15 mm. However, for the standard ECoG array tested, which covered a distance of 90 mm, coherence was reduced for signals in the range of 0-80 Hz and was slightly increased for the range of 80-400Hz (Kellis, 2016, Multi-scale analysis of neural activity in humans: Implications for micro-scale electrocorticography). By comparison, the array D1 has less of a clear-cut pattern and showed increased fluctuation across frequency bands. Patterns observed on all three arrays were dynamic and varied compared to larger, more spatially segregated signals, such as ECoG (Kellis, 2016, Multi-scale analysis of neural activity in humans: Implications for micro-scale electrocorticography) or EEG, which have reported cross-correlation is linearly correlated with distance (Bhavsar, 2018, The Correlation between EEG Signals as Measured in Different Positions on Scalp Varying with Distance).

The spatial complexity of the signals collected at this millimeter resolution supports the claim that standard ECoG, operating with centimeter spacing, will inherently under sample the neural activity of interest for BCI applications. Furthermore, the high impedance of the micro-electrodes, resulting in part from the small radius, maintains the specificity of the recording. Using larger diameter and lower impedance electrodes increases the range from which signals are collected. The data collected with macro electrodes integrates activity from larger populations of surrounding neurons, missing the intricate variations of cortical column activity and reflecting broader more coordinated activation across many columns. However, the computational and

bandwidth restrictions need to be considered. Standard clinical ECoG, while less able to resolve micro-scale fluctuations in neural activity, does provide increased coverage area, increasing likelihood of having electrodes placed over a relevant cortical area. To maintain a similar coverage area with micro-ECoG would require either an increase in channel count or a reduction in electrode density. Increased spatial coverage of the grid by adding more electrodes would increase the number of relevant neural signals and allow better decoding accuracy. Larger coverage area would increase the probability of placing the grid in the optimum location given patient-to-patient variability and possible cortical reorganization due to neurological disorders. Increasing the number of electrodes would require a recording system with higher bandwidth and storage for the larger volume of data. Ideally, thinner and larger wireless nonpenetrating microelectrode arrays would be implanted chronically in patients with severe paralysis or locked-in syndrome to provide control signals for highly articulate prosthetic devices.

Generally, the decode performance for patients implanted with grids manufactured by PMT was higher than the decode performance for patients implanted with grids manufactured by Ad-Tech. The wires forming the electrodes in PMT grids terminated in small protuberances of silicone, which may have pushed against the arachnoid layer resulting in better contact with the cerebral cortex and stabilizing the position of the grid relative to the cortex. The wires forming the electrodes in Ad-Tech grids terminated flush with or slightly protruding from the silicone base, which may have allowed cerebrospinal fluid to accumulate between the electrode and the cerebral cortex. The accumulation of cerebrospinal fluid increases electrical shunting between electrodes and a higher correlation of neural signals between electrodes (S. Kellis, Greger, Hanrahan, House, & Brown, 2011). Due to the silicone protuberances and the micro-wires extending above the silicone base of the grids, great care was taken to not slide the grids along the surface of the cortex. This study demonstrates while the size of electrodes is well suited to record relevant information, improvements can be made with these devices. Manufacturing grids that either protrude slightly in a safe way or are made of a material that conforms to the cortex surface may prevent grid movement and cerebrospinal fluid from accumulating between the cortex and the grid. Thinner

grids are currently being designed to have increased flexibility using materials such as polyimide (Thongpang et al., 2011; Viventi et al., 2011) or PDMS (Ochoa, Wei, Wolley, Otto, & Ziaie, 2013).

This study contributes evidence towards there being significant motor information represented on the cortical surface at the microscale, and micro-ECoG arrays can acquire LFP signals at this scale. Furthermore, signals collected on tightly spaced electrodes exhibit limited correlation in the frequency bands of interest to most decoding studies. By providing high spatial and temporal resolution recordings of cortical activity, non-penetrating microelectrode arrays are a promising neural interface for providing articulate and intuitive control for prosthetic devices.

CHAPTER 3

MODELING NON-PENETRATING STIMULATION OF STRIATE CORTEX: IMPLICATIONS OF ELECTRODE SCALE ON TISSUE ACTIVATION

ABSTRACT

A physiologically representative model of cortex was devised to evaluate complex and spatially varying interactions between externally applied currents and the electrophysiology of the tissue. The model geometry was comprised of stacked layers of tissue with an electrode array placed on the surface of the cortex model. To evaluate efficacy, the model was fitted to tissue properties of striate cortex and used to estimate current thresholds to activate layer 3 of cortex via surface stimulation with microelectrodes and compared to values collected form in vivo experiments. During the experiments electrical current was applied to surface electrodes placed over primary visual cortex and incremented until a visual sensation was perceived. This paradigm yielded results in close approximation to the thresholds expressed with the model. Validity and robustness were further evaluated by surveying literature of striate cortex stimulation, applying electrode properties used, and then comparing the modeled values to experimental. All values surveyed were in close relation to the computed thresholds.

INTRODUCTION

Over the past few decade, there has been a push to develop neural prosthetics that not only provide naturalistic control over a device, but also encode sensory information to the user. The functionality of sensory encoding relies on the principle that electrical stimulation of neural can be used to influence populations of neurons and induce a pattern of activation in such a way that a sensation is perceived by the subject. It is assumed that this pattern directly correlated with the evoked percept and that the sensation experienced can be manipulated by controlling the pattern of activation.

Functional level phenomena are built on the basis that externally applied electric fields can be used to depolarize or hyperpolarize the excitable cell membrane, either activating or inhibiting

the cell. Selectively activating or inhibiting localized regions can be used to manipulate the evoked sensation. Electric fields act on neural tissue by inducing a change in the extracellular potential, modulating transmembrane potential (Merrill, Bikson, & Jefferys, 2005; Ye & Steiger, 2015). Charge transfers across the membrane via passive membrane properties and active ion channels. Under cathodal stimulation, the electrode's negative charge locally redistributes, causing depolarization near the electrode site and hyperpolarizing tissue distal to the electrode site, suppressing activation (Merrill et al., 2005). Conversely, anodal stimulation hyperpolarized the area near the electrode and causes a distant depolarization. In practice, stimulation paradigms frequently employ pulse trains of charge-balanced biphasic stimuli. This serves to reduce charge accumulation in the tissue and reduce electrically induced tissue damage. Cathodal or anodal leading waveforms can be used. Taking into account the spatial variations in activation noted with either cathodal or anodal stimulation, cathodal-first waveforms may be more appropriate when targeting cell populations proximal to the electrode site, and anodal-first waveforms may be more appropriate when targeting cell populations distal to the stimulating electrode.

Interfacing with populations of neurons, the first factor to consider is the relationship between the applied current and the extent of activated tissue. Ideally, in the case of brain computer interfaces (BCIs), the volume influenced must be large enough to evoke the desired perception, but sufficiently localized to maximize the number of discrete points to interface with tissue. Improving the focal nature of a stimulus allows neighboring stimulation sites to be placed in close proximity without necessarily interfering with each other; a higher number of discrete points of interface per square area of tissue allows theoretically for a finer resolution and encoding of more complex or nuanced snesations. The sphere of activated neurons around an electrode site increases with current amplitude (Stoney, Thompson, & Asanuma, 1968; Tehovnik, 1996). The lower and upper limits for therapeutic stimulation are bounded by the perception threshold and tissue damage threshold. The extent of an electrode's influence and both bounding thresholds are determined in part by its geometry and surface area. Large diameter electrodes are low impedance and require higher currents to generate an electric field strength sufficient to active nervous tissue, but also generate a larger field and influence a larger population of neurons. Reducing electrode

size increases impedance and reduces both the current required to generate an electric field of similar strength and the extend of activated tissue.

Thresholds for tissue damage are also known to scale differently with electrodes of different sizes. A review of stimulation studies indicates charge density provides a more accurate indication of tissue for stimulation with macro-scale electrodes and charge per phase a stronger metric of tissue damage for stimulation via micro electrodes (Cogan, Ludwig, Welle, & Takmakov, 2016). The Shannon equation is often used to describe the boundary between damaging and non-damaging levels with the relationship between charge per phase and charge density given by:

$$\log\left(\frac{Q}{A}\right) = k\log(Q) \tag{3.1}$$

where *Q* is charge per phase (μC) and *Q/A* is the charge density per phase (μC/cm^2) (Merrill et al., 2005), whereby below this line, a stimulation paradigm is not indicated to damage tissue. This relationship was developed through experimentation with large electrodes (GSA of .01cm^2 – .5cm^2) and, while it tends to reflect damage thresholds well for large electrodes, it may not be a reliable indicator of tissue damage for stimulation with micro-scale electrodes. Current clinical applications generally impose a recommended limit on charge density of a stimulation pulse of 30μC/cm^2 out of a concern for tissue damage, however some studies have seen damage as low as 12 μC/cm^2 and other studies have reported no damage up to 60μC/cm^2. Although a factor to consider, there are limitations of this predictive model and its applicability to micro-stimulation. Current density thresholds for damage have been shown to scale differently with microelectrodes (GSA<.01cm^2). The charge density to charge per phase relationship described does not directly translate to microelectrodes. Charge per phase appears to be a stronger predictor of the damage threshold for microelectrodes with an approximate damage threshold observed around 4nC/phase(Cogan et al., 2016). The geometric surface area (GSA) of a stimulating electrode has non-trivial implications for the damage threshold and should be taken into account when determining the electrical parameters for therapeutic stimulation. Given the central role electrode size plays in effective therapeutic stimulation, this study seeks to directly compare activation patterns of surface level cortical

stimulation under a range of electrode diameters. Of specific interest is optimizing surface electrode size for use in cortical visual prosthetics.

Electrical stimulation of primary visual cortex has been shown to elicit visual sensations and its proper implementation may be used to create a functional visual prosthesis. For sensory prostheses to remain viable, they must interface at a biologically relevant level and consistently evoke visual percepts without impairing visual processing. Research on restoring vision by cortical stimulation has historically focused on stimulation via large subdural electrodes with diameters greater than 1mm in diameter, or via intracortical microelectrodes, penetrating electrodes with <200μm^2 stimulating sites that reach 0.5-1.5mm into cortex. Epicortical macroelectrodes are less invasive, but require high levels of current to evoke a visual percept, yielding unnatural sensations and a concern for initiation of seizure activity. Intracortical microelectrodes allow for greater spatial resolution and lower stimulation thresholds. However, the intracortical placement of a microelectrode array presents surgical limitations on placement and may engender a greater tissue response than epicortical placement. While a potentially viable option for providing stimulation at the occipital pole, the geometries of both the array and brain prevent placement at most cortical visual field representations. Epicortical microelectrodes, like their macro counterparts, sit flush on the surface of the brain, while maintaining an interface with cortex at a similar scale to intracortical microelectrodes (Kellis et al., 2016). This interface may provide therapeutic stimulation that strikes a balance between spatial resolution, surgical access, and longevity that maximizes utility to patients.

For an epicortical microelectrode array (EMEA) to act as a viable basis requires confirmation that surface stimulation at this scale can sufficiently activate cortex to evoke visual percepts. Experimental data suggests micro electrodes are capable of targeting tissue 2-5 times the largest exposed electrode dimension (Cogan et al., 2016). Ideally, an approach will use the smallest diameter at which percepts can be elicited so that the benefits of microscale electrodes can be maximized. With this, there is a necessary trade-off between electrode diameter and depth of tissue activation. Larger electrodes will be able to activate deeper cortical layers but require higher currents to maintain charge density, whereas smaller electrodes will have higher specificity

but electrodes with too small of diameter may not be able to sufficiently activate the target population. Intracortical studies typically target cortical layers II-IV (Davis et al., 2012; DeYoe, Lewine, & Doty, 2005; Normann, Maynard, Rousche, & Warren, 1999; Schmidt et al., 1996; Torab et al., 2011; Troyk, 2017), as direct stimulation of these layers have the lowest threshold for evoking visual percepts (DeYoe, Lewine, & Doty, 2005) and because these layers could be useful for restoring vision as they include the termination of the geniculo-cortical projections (Layer IV) and the origins of the cortico-cortical projections to higher level visual processing areas (Layers II/III) (Purves et al., 2008). Surface level microstimulation will likely be able to target the more superficial cortical Layers II/III.

There is an additional tradeoff between effective resolution and electrode size. EMEAs interface with cortex on similar scale to intracortical microelectrodes (Kellis et al., 2011), and therefore likely provide more precise activation than their macro counterparts. Smaller electrodes, influencing smaller volumes of cortex, can be placed in closer proximity before their electric fields interact. Studies using microwire electrodes have reported smaller distances at which simultaneous stimulation evoked separate percepts (G. S. Brindley & Rushton, 1974; DeYoe et al., 2005; Lewis & Rosenfield, 2016), compared to larger surface electrodes (Bosking et al., 2017; Dobelle, Quest, Antunes, Roberts, & Girvin, 1979; Winawer & Parvizi, 2016). Stimulating with too little separation between sites can modulate the quality of and threshold to evoke a percept (G. Brindley & Lewin, 1968; DeYoe et al., 2005). Furthermore, there is a correlation between intensity of the applied current and the volume of activated tissue (Bosking et al., 2017). If minimizing electrode diameter can also significantly reduce current threshold, this should aid in localizing activation. Without excessive testing it is impossible to determine the ideal separation and how it may scale with electrode diameter. However, modeling approaches may be able to constrain the parameter space.

This study proposes a 3D finite-element bidomain model with FitzHugh-Nagumo membrane equations. Bidomain models approximate behavior of active tissue by evaluating electrical potentials of intra- and extracellular domains occupying the same region of space and continuously coupled by a membrane (Henriquez, 1993). Underlying ionic mechanisms can be taken into account in defining the active membrane and modulated to fit a given cell type. Initially

developed for modeling cardiac tissue, the approach has since been applied to full scale modeling of brain tissue (Sadleir, 2010). It has shown use in evaluating neuro-stimulation paradigms for large scale applications like TCDS (Dougherty, Turner, & Vogel, 2014), and more localized nerve stimulation studies (Meffin et al., 2014), as well as modeling activation of retinal tissue (Dokos, Suaning, & Lovell, 2005). This approach was chosen for its capacity to account for the spatial extent of activation of tissue and evaluate activation at multiple scales of interface. Additionally, simplified equations to represent membrane activity were chosen to account for spiking behavior while minimizing computational load. The focus of this study is on comparing micro- and macro- scale surface stimulation of cortex; this model can be used to describe activity at the at both scales without a large increase in computational intensity.

This study looks to compare the range of tissue activation under threshold-level stimulation across electrode scales, establish current thresholds for perception, and estimate tissue damage at therapeutic levels. Herein we propose a continuum model of striate cortex to evaluate cortical activation patterns under different stimulation paradigms and the spatial extent of stimulation with various electrode diameters ranging from micro to macro scale.

METHODS

Geometry and Setup. Simplified cortex geometry was generated in COMSOL 5.3 and consisted of square-shaped laminar partitions to account for variations across striate cortex layers. The total cortex thickness was 1.96mm and accounted for the six layer of cortex, with layer IV further subdivided. One active electrode was set in the center of the model, with two large returns set in opposite corners. Surface electrodes were modeled by flat cylinders of platinum embedded in a 0.1 mm sheet of polyimide (Figure 3.1). Model was scaled to increase with electrode diameter.

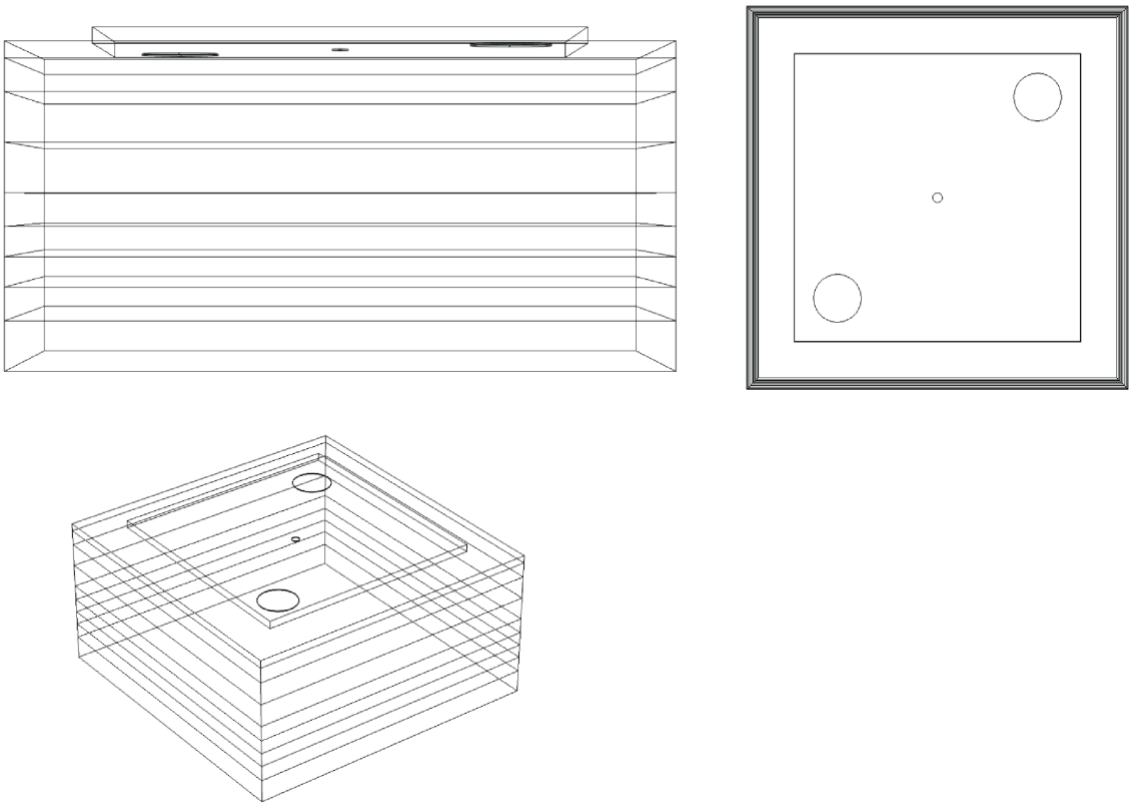

Figure 3.1. Model geometry for 200μm electrode configuration. Top, side and isometric view of model. Geometry consists of nine layer representing the six layers of cortex, with layer IV subdivided into IVa, IVb, IVcα, and IVcβ. Model a single active electrode in the center of the model and two large return electrodes embedded in a polyimide array layer. The surface array Is surrounded by a CSF layer and topped by a cortical bone layer.

Model equations. T The equations governing the electrophysiology of the tissue were adapted from a full brain-scale model with applied tDCS (Dougherty et al., 2014) and fit to this laminar cortex approach. The bidomain equations are given by the following system of partial differential equations:

$$\nabla\cdot(\sigma_i\nabla V_m+\sigma_i\nabla\phi_e)=\beta\left(C_m\frac{\partial V_m}{\partial t}+I_{ion}\right) \tag{3.2}$$

$$\nabla\cdot\left((\sigma_i+\sigma_e)\nabla\phi_e+\sigma_i\nabla V_m\right)=0 \tag{3.3}$$

$$\frac{\partial\vec{s}}{\partial t}=F(\vec{s},v,t) \tag{3.4}$$

where V_m is the transmembrane potential, and ϕ_e is the extracellular potential. This formulation uses V_m in place of ϕ_i, the intracellular potential, where $\phi_i = V_m + \phi_e$. Intracellular and extracellular membrane conductances are represented by σ_i and σ_e. C_m is the membrane capacitance, β is the

surface to volume ratio, and $\mathrm{I_{ion}}$ represents the total ionic current between intra- and extracellular domains, with the boundary condition:

$$\nabla \cdot \sigma_{ext} \nabla \phi_{ext} = 0 \tag{3.5}$$

FitzHough Nagumo equations were used to model transmembrane voltage dynamics.

$$\frac{\partial V_m}{\partial t} = \frac{c_1}{V_{amp}^2}(V_m - V_{rest})(V_m - V_{th})\left(V_{peak} - V_m\right) - c_2 W_m + I_{app} \tag{3.6}$$

$$\frac{\partial W_m}{\partial t} = b(V_m - V_{rest} - c_3 W_m) \tag{3.7}$$

All parameter values and units used with the model configuration implemented are presented in Table 3.1 with brief descriptions for each parameter. The transmembrane and extracellular potentials during an action potential modeled by the Fitz-Hough Nagumo configuration used are presented (Figure 3.2).

Table 3.1

Parameter Values

Parameter	Value	Units	Description
V_{amp}	$V_{peak} - V_{rest}$	V	Spike amplitude
V_{th}	$V_{rest} + aV_{amp}$	V	Threshold to fire
V_{peak}	0.04	V	Peak membrane potential
V_{rest}	-0.07	V	Resting membrane potential
σ_i	0.638	S/m	Intracellular conductivity
σ_e	1.538	S/m	Extracellular conductivity
σ_{CSF}	2.14	S/m	CSF conductivity
σ_B	0.0014	S/m	Bone conductivity
σ_{PtG}	$4X10^6$	S/m	Electrode conductivity
β	126000	$1/m$	Surface to volume ratio
C	0.0001	F/m^2	Membrane capacitance
b	130	S/m^2	Tune deactivating amplitude
c_1	260	S/m^2	Tune membrane potential
c_2	10000	S/m^2	Tune deactivating influence

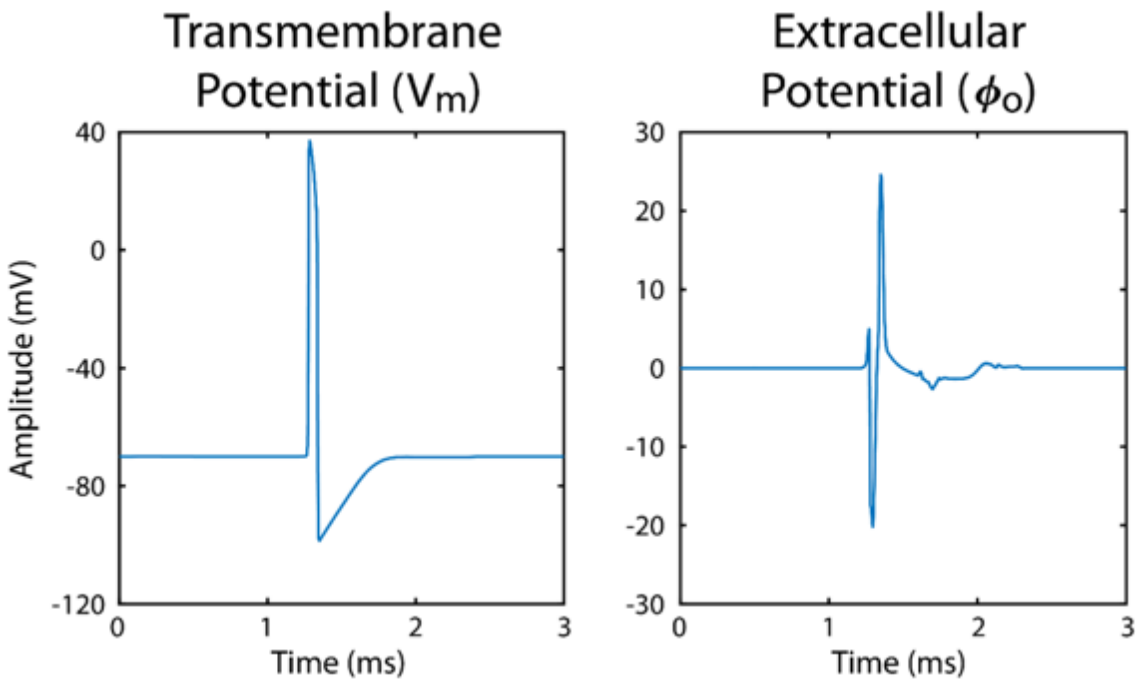

Figure 3.2. Action potential behavior with Fitz-Hough Nagumo implementation. Left depicts the time course of transmembrane potential during an action potential in this model. Right displays the calculated extracellular potential during the same time course as the action potential.

Tuning model to striate cortex. Cortex is traditionally divided into six layers that segregate neuronal populations with distinct connective patters; visual cortex is further subdivided to account for laminar complexity (Purves et al., 2008). Limited information regarding laminar variations in tissue conductivity exist, with some sources indicating impedance and tangentially conductance can be considered homogeneous within a localized area of grey matter (Logothetis et al., 2007). Under this assumption, conductance values were established by layer, and assumed isotropic. The model was tuned to striate cortex by manipulating intra- and extracellular conductivity ratios based on laminar variations in volumetric cell density. Metrics of cell density by layer in striate macaque cortex listed in Table 3.2 were taken from (Weber, Keller, J., & Logothetis, 2008) and applied as the assumed ratio of intra- to extracellular space and implemented as follows:

$$\sigma_i^0 = f_{Li}\sigma_i \tag{3.8}$$

$$\sigma_e^0 = (1 - f_{Li})\sigma_e \tag{3.9}$$

where f_{Li} is the fractional fill volume of cells for a given layer. The derived macroscopic conductances σ_i^0 and σ_e^0 were then substituted for the original intra- and extracellular conductance values.

Table 3.2

Fractional Fill Volume

Tissue Layer	f_{Li}
I	0.2
II	0.5
III	0.4
IVa	0.45
IVb	0.3
IVcα	0.4
IVcβ	0.5
V	0.3
VI	0.4

Electrical stimulation. The stimulation paradigm used mimics that used in in vivo experiments. The applied stimulus was a cathodal-first, charge-balance, biphasic waveform, with 400μs phase duration and 100μs interphase interval and implemented via a boundary current source normal to the electrode surface.

$$n \cdot J = Q_j(t) \tag{3.10}$$

The amplitude of the current density Q_i is defined by the applied current divided by the geometric surface area, GSA of the electrode

$$Q_i = I_{app}/GSA \tag{3.11}$$

$$Q_j(t) = Q_i * \big(Rect1(t) + Rect2(t)\big) \tag{3.11}$$

The applied boundary current Q_j is a function of time, scaled by Q_i. The biphasic waveform is generated in COMSOL by the summation of two time shifted rectangular functions $Rect1(t)$ and $Rect2(t)$. The width for each function is set to 0.4 ms with a 0.2 ms transition zone and two continuous derivatives. The centers of the two rectangles are offset by 0.7 ms. For cathodal-first stimuli, the leading rectangle function is given a unitless amplitude of -1 and the following rectangle has an amplitude of 1. For anodal first paradigms the aplitudes are reversed. The resulting

waveform is a close approximation to a single pulse biphasic waveform with 0.6 ms pulse width (Figure 3.3).

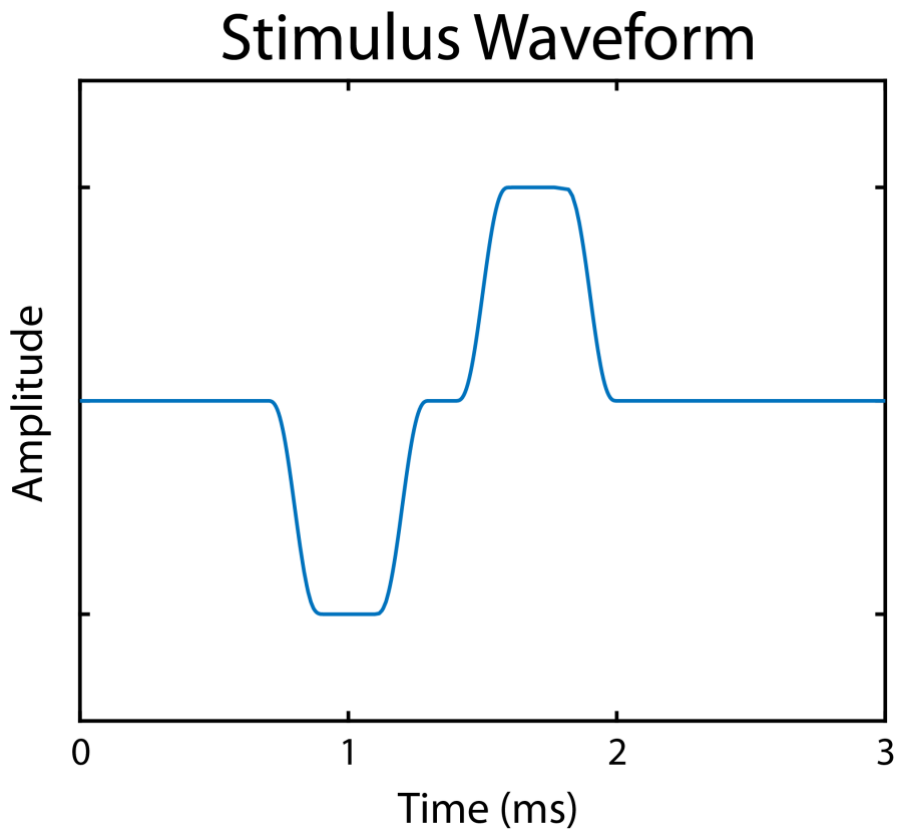

Figure 3.3. Stimulus waveform applied to excite tissue. Charge balanced, biphasic waveform used in modeling study, similar in form to the .4-.6ms phase duration waveforms used to for in vivo studies.

Electrode diameter. To compare tissue activation patterns across size of electrode-tissue interface, simulations were conducted with surface electrodes at the following diameters: 100μm, 200μm, 300μm, 500μm, 700μm, 1mm, 2mm, and 3mm. This accounts for electrode interfaces ranging from micro-scale to macro. Each simulation involved distant grounds, placed in opposite corners of the array, with one electrode in the center of the array applying stimulation.

Determining sufficient activation for perception. Criteria to determine perception threshold was based on charge density requirements to evoke a response from intracortical microstimulation. A charge density of 30μC/cm^2 in the middle of layer II/III generated by stimulation

was selected based on lower charge density limits for visually evoked percepts and evoked motor responses reported in literature (Brunton et al., 2015; Schmidt et al., 1996; Tehovnik, 1996).

Model Validation.

Multi-physics engine. Initial model verification for proper physics engine functionality was conducted by comparing model derived near field charge density to that calculated from the electrode geometric surface area and applied current.

$$\rho_s = \frac{I*W}{A} \tag{3.12}$$

where ρ_s is the charge density per phase near the electrode cite, I is the stimulating current, W is the time duration of pulse width, and A is the geometric surface area of the electrode. The model chare density, ρ_m was determined by integrating the normalized current density J_n over the duration of the phase with respect to time at each point in the model. For the purpose of near field charge density validation, the point in the center of the electrode on the top layer of tissue was used.

$$\rho_m = \int_0^W J_n \, dt \tag{3.13}$$

Threshold prediction. The model and its ability to predict perception thresholds and activation patterns was validated by comparing the current amplitudes determined by the model with values for evoking visual percepts reported in literature for available diameters. Diameters available in literature are 1-3mm, reported from human studies. Additional validation for the 200µm diameter electrode model was conducted in house with a nonhuman primate study.

Calculating activated cortex and phosphene size. The metric to determine activated cortex for each model parameter evaluated was a volume integration for points at which the current density exceeded 140 µA/mm^2 at maximum current density spread. This metric was chosen as it aligns within the range of current density for neuronal excitability (Tehovnik, 1996) as well as lower limits for excitability found for this model. An estimation of activated cortex where the radius of activated cortex is based on applied current (Stoney et al., 1968) provided by equation 3.14 was adapted to include electrode size in addition to applied current (Equation 3.15).

$$R = \left(\frac{I}{K}\right)^{1/2} \tag{3.14}$$

$$R = \left(\frac{I}{K} + r_e^2\right)^{1/2} \quad (3.15)$$

where R is the radius of activated cortex, K is the current-distance constant, and r_e is the radius of the stimulating electrode. From this, the activated volume of cortex $V_c$can be reasonable predicted for a surface electrode by the following:

$$V_c = \left(\frac{2}{3}\right)\pi R^3 \quad (3.16)$$

This predictive metric was compared with the actual volume of activated cortex derived from the model measurements.

The extent of activated cortex can be used to approximate the size of a phosphene evoked by stimulation, based on a model provided by (Bosking et al., 2017), whereby:

$$PS = AC * 1/M \quad (3.17)$$

$$1/M = (Ecc + e2)/A \quad (3.18)$$

where PS is phosphene size, AC is the diameter of the activated cortex, M is the linear cortical magnification factor, Ecc is the eccentricity, $e2$ is the eccentricity at which M falls to half foveal of its value, and A is a cortical scaling factor. The model was developed experimentally in human cortical stimulation studies, with additional information regarding the process available in the cited work (Bosking et al., 2017).

RESULTS

Model validation.

Spiking waveform shape. The simulated electrophysiology provided a simple approximation of a biological action potential. An example of the spike shape generated from the model parameters is presented observed from transmembrane potential (V_m) as well as the extracellular potential (Φo) evoked. Model parameters provided a signal that is quasi-biological in appearance from the perspective of the both membrane potential and activity patterns generally observable from tissue surrounding a spiking cell (Figure 3.3).

Near field charge density. Initial model verification for proper functionality was conducted by comparing model derived values for change density measured at the electrode-tissue interface

with the expected value calculated by equation 3.13. Modeled charge density near the electrode surface aligned with the expected charge density for each electrode diameter and current value evaluated (Figure 3.4). The mean square error of the log of expected verses model generated values was 0.001. The model accurately generated expected charge density values at the simulated electrode-surface interface.

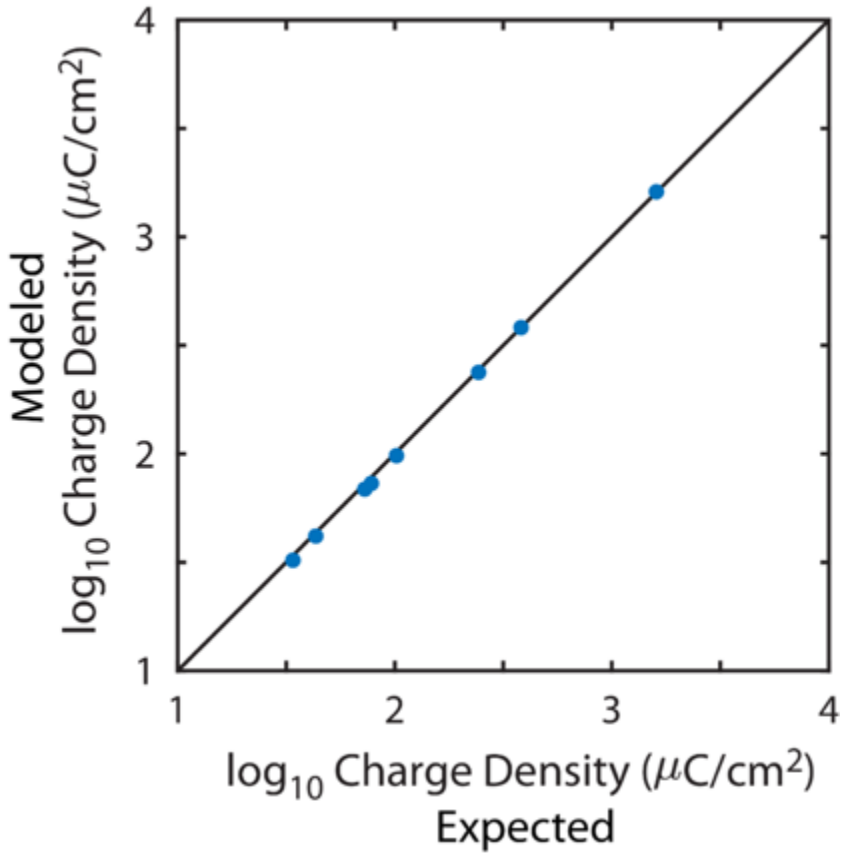

Figure 3.4. Near-field charge density model validation. Charge density measured from model compared to calculated charge density per phase. Model derived values plotted against their expected values reflects a high degree of match, indicating proper physics engine and model functionality.

Electrode diameter

Perception threshold. The model developed was able to adequately predict current thresholds for evoking a visual percept. Compared to the data available in literature, the model was within the range of reported values for macro electrodes, and in range for the 0.2 mm electrode with a small error from the array averages. The same was also true for 0.5 mm electrode when

appropriately adjusted for matched pulse width. The adjustment was conducted by multiplying the threshold by a scaler provided by (Tehovnik, 1996) (Schmidt et al., 1996) to account for the variance between the pulse width used in the model and that used in the study reporting in vivo values. Likewise, threshold values for evoking phosphenes with electrode diameters of 1 – 3 mm were within the range of reported values for evoking phosphenes from stimulation of visual cortex. Values for each diameter examined are reported in Table 3.3.

Table 3.3

Model Determined Thresholds Compared to In Vivo Results

Diameter (mm)	Model Threshold (mA)	Reported Threshold Range (mA)	Reference
0.2	0.25	0.15 – 0.49	
0.5	0.79*	0.81**	(Bosking et al., 2017)
1	0.98	1 – 4	(Dobelle et al., 1979; Winawer & Parvizi, 2016)
2	3.12	2 – 4	(Dobelle et al., 1979)
3	7.00	2 – 12	(Dobelle et al., 1979)

* Value adjusted by scaler multiplier for difference in phase durations
** Only mean value reported

The model predicted thresholds rise with electrode diameter (Table3.4) and are accurately described in accordance with a sigmoid function (R^2 = 0.999, MSE = 0.25). Thresholds begin low with minimal variations for small diameter electrodes 0.1 and 0.2 mm and begin to rise sharply over 0.7 mm in diameter to create sufficient charge density mid layers II/III to meet the threshold criteria (Figure 3.5). An upper plateau begins to emerge following 3 mm.

Table 3.4

Model Determined Thresholds

Electrode Diameter (mm)	Current Threshold
0.1	0.29
0.2	0.29
0.3	0.42
0.5	0.52

0.7	0.67
1.0	0.98
2.0	3.12
3.0	7.00

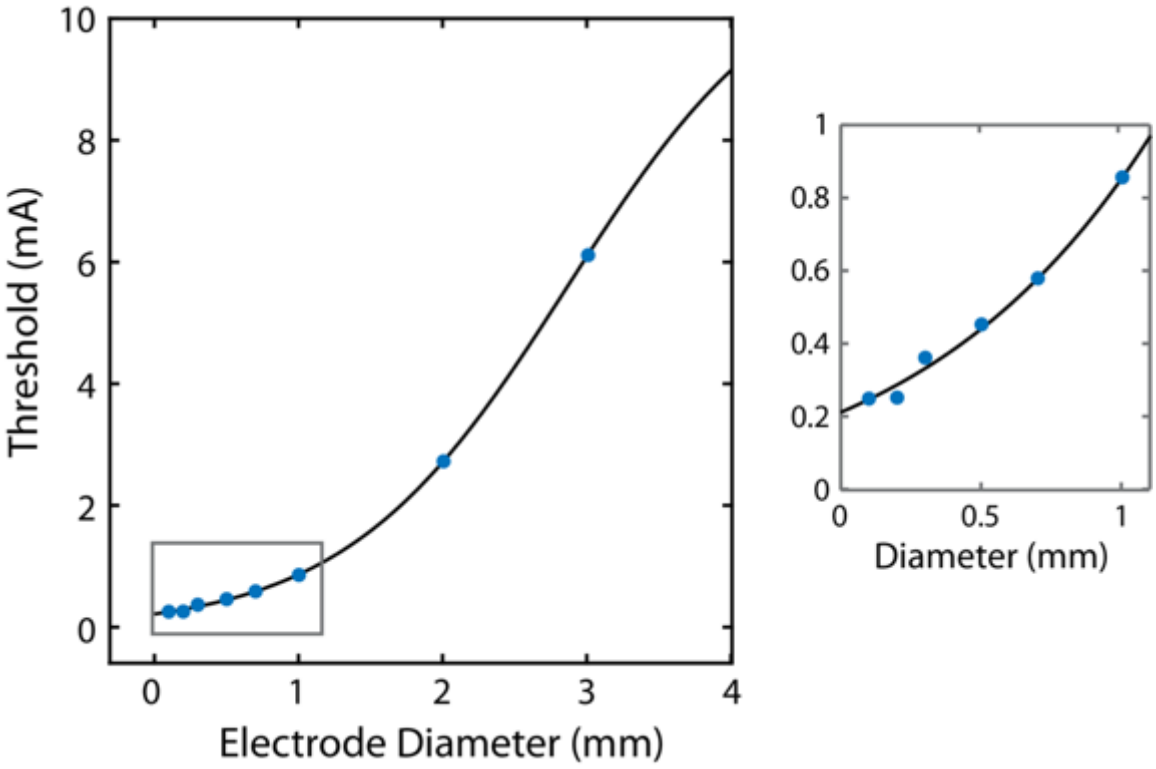

Figure 3.5. Predicted current thresholds for electrode diameter. Model predicted current thresholds to evoke a visual percept for each electrode diameter evaluated. The left plot indicates all values tested with a sigmoid curve fit to the data (R^2 = 0.999, MSE = 0.25). The smaller portion boxed in grey is presented on the right for improved detail and visibility.

Charge density profiles. The spatial dynamics of the charge density in tissue varied with electrode diameter. Smaller diameter electrodes tended to have a high initial charge density at the surface of the tissue, at the center of the electrode-tissue interface, followed by a sharp decay both laterally and with increasing depth. As electrode diameter increases, charge density profiles show a tendency to have a more gradual rise and decay in charge density across the surface and towards the lower layers of tissue (Figure 3.6). Increasing electrode diameter results in a larger radius of tissue for which charge density is sufficient to cause activation or damage. Little difference was noted between 0.1 and 0.2 mm diameter electrodes in their respective charge density profiles. Both maintained a radius of activation of 0.37 mm. The remaining electrodes, 0.3, 0.4, 0.5, 0.7, 1, 2, and

3 mm electrodes observed activating radii of 0.44, 0.49, 0.57, 0.86, 1.31, 1.89 mm respectively. The range activated increased rapidly for electrode sizes above 0.7 mm.

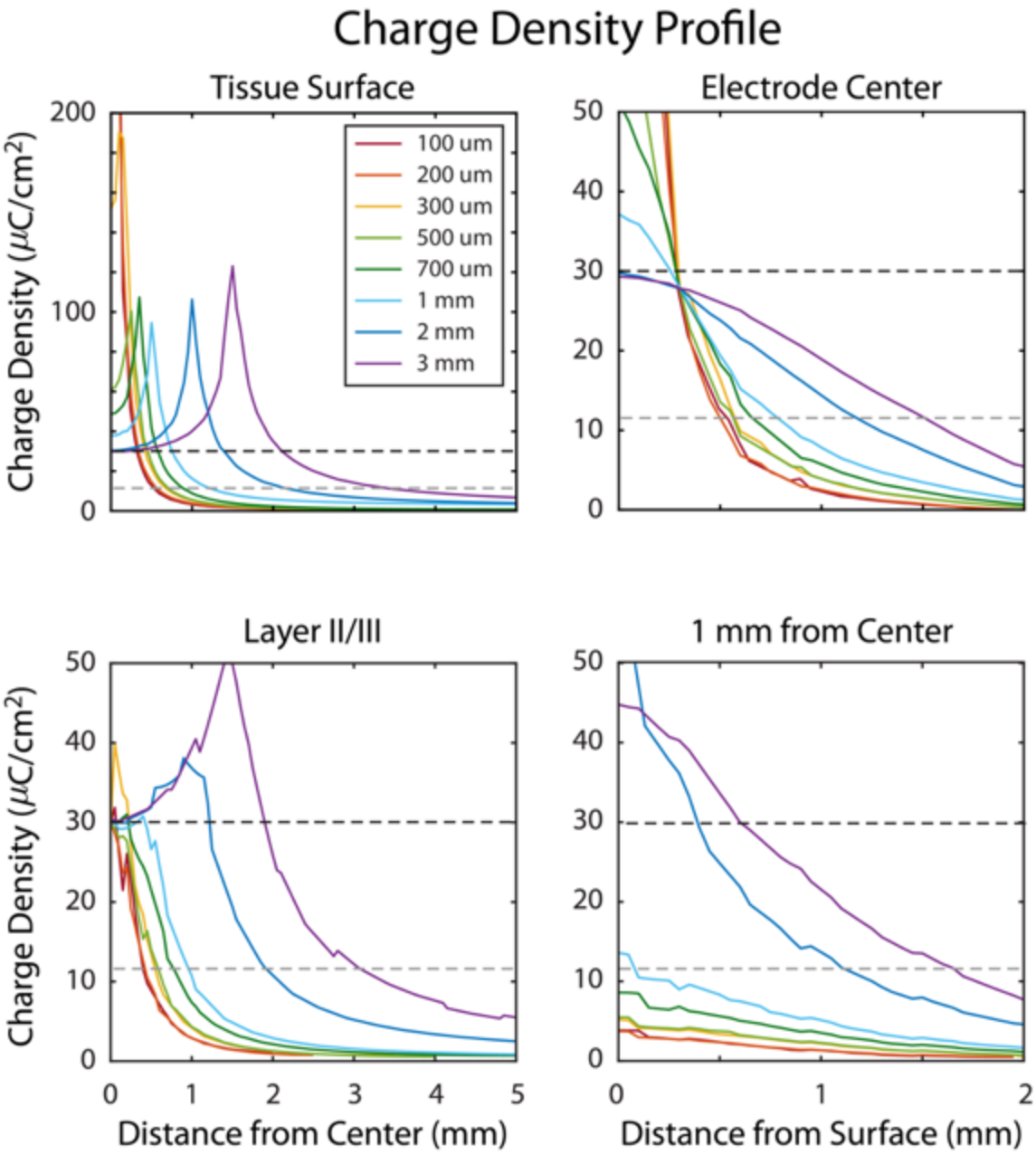

Figure 3.6. Tissue charge density profiles with distance from source. Model derived charge density values measured at different points in space. Left plots show charge density in plane with tissue lamina and moving perpendicular to the orientation of the electrode. The top plot indicates values on the surface of the tissue at the electrode tissue interface from 0, the point at the center of the electrode, to 5 mm linear distance from the electrode center along the tissue surface, parallel to the tissue lamina. The lower left plot shows a similar travel paradigm with values collected in plane with tissue lamina but collected in the middle of Layers II/III. The plots on the right present charge

density as it decays through space, perpendicular to tissue layers and in line with the orientation of the electrode. The top plot shows values collected at the center of the electrode with distance increasing linearly from the surface of the tissue into the deeper layers. The lower plot shows the same movement trajectory collected in a line 1 mm from the electrode center.

Activation patterns. A cross section of the extracellular potential visible at the center of the model, directly beneath the stimulating electrode, generated following termination of the stimulus can be used to compare spatial patterns of activation across electrode sizes. The spatial extent, both in depth and laterally increase with electrode size. Furthermore, the extent of "rippling" behavior created by virtual sources and sinks reveals the extent to which tissue surrounding the electrode cite can be affected. For the smaller electrodes, 0.1 and 0.2 mm sizes in particular, activation remains local to the electrode surface. However, larger electrodes further extend modulation through the full depth of tissue, observed most notably in the 3mm diameter electrode (Figure 3.7).

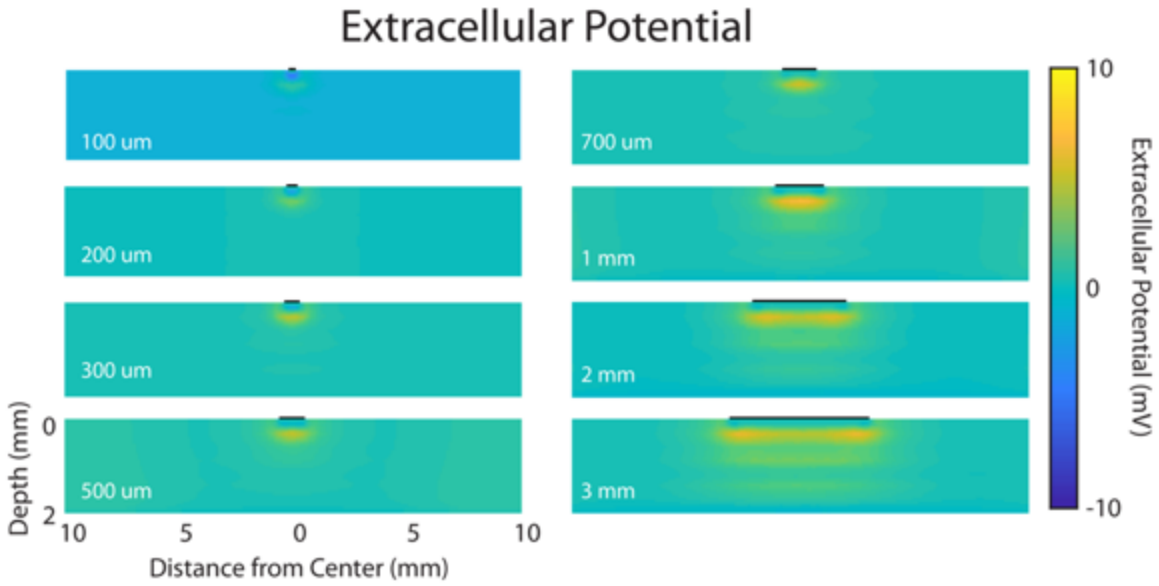

Figure 3.7. Cross section of evoked extracellular potential for each electrode size evaluated. Extracellular potential measured in a cross section of the model at the center of the stimulating electrode. Presence of virtual sources and sinks increases in extent and intensity with increasing electrode size.

Activated cortex. Activated cortex at threshold increased rapidly with electrode diameter. The three smallest electrodes (0.1, 0.2, and 0.3 mm) maintained similar volumes of activation.

Volume increased at a gradual rate from 0.37 mm^3 for 0.1 and 0.2 mm electrodes to 1.59 mm^3 for 0.7 mm electrode, the rose sharply to 5.29 mm^3 for 1 mm, 18.52 mm^3 for 2mm, and 56.23 mm^3 for 3 mm (Figure 3.8).

A metric for calculating volume of cortex activated for surface electrodes has been proposed in order to account for electrode diameter in addition to applied current. The method described by Equations 3.15 and 3.16 reduces mean-square error to 0.68, compared to 3.52 when calculated with the traditional method (Figure 3.9).

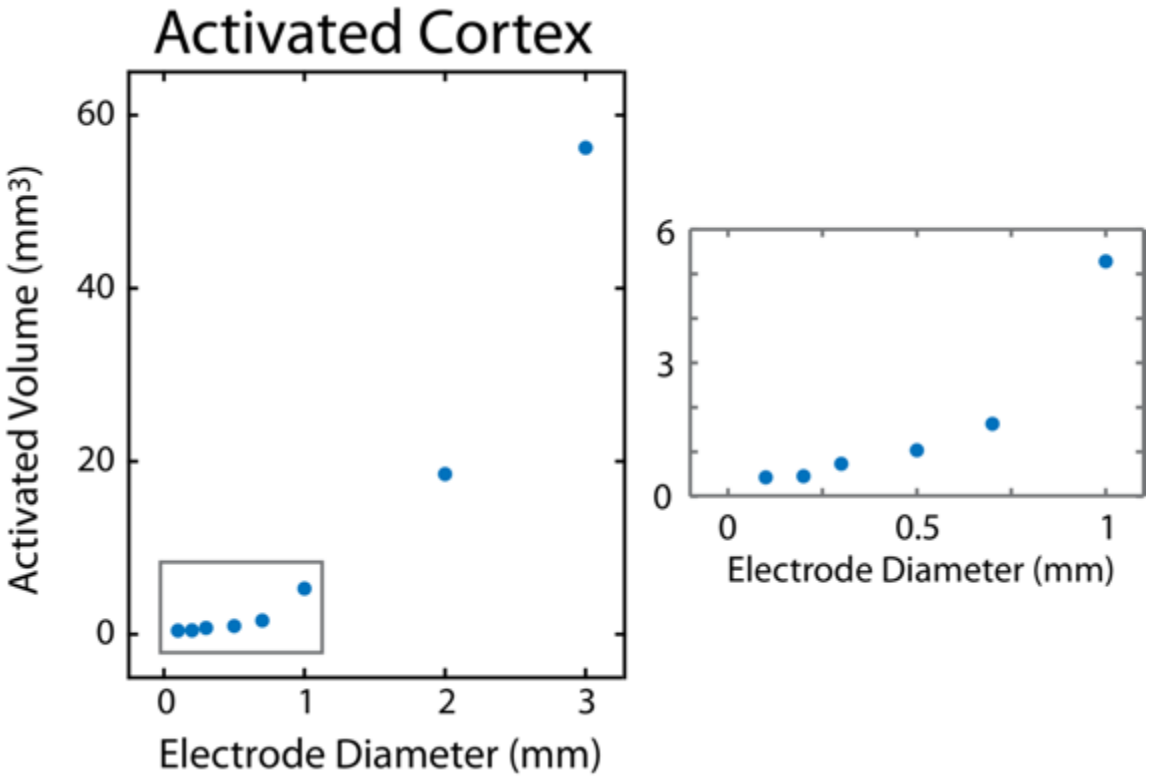

Figure 3.8. Volume of activated cortex during stimulation at threshold. The volume of tissue influenced by the applied stimulus for each electrode size evaluated is presented on the left. The grey box indicates the region inflated for viewing ease on the right.

Predicted phosphene size. A comparison of the range of predicted phosphene sizes at threshold is presented for 0.2 and 2mm diameter electrodes across increasing eccentricity. Evaluating the upper limits for shows a large discrepancy in expected percept size between the two electrodes (Figure 3.9). With the 0.2 mm electrode, evoked percepts are comparatively

punctate, even at more peripheral eccentricities. The size of the theoretical percept evoked at 15° of eccentricity with the 0.2 mm diameter electrode is approximately the size of a percept evoked foveally with a 2 mm diameter electrode.

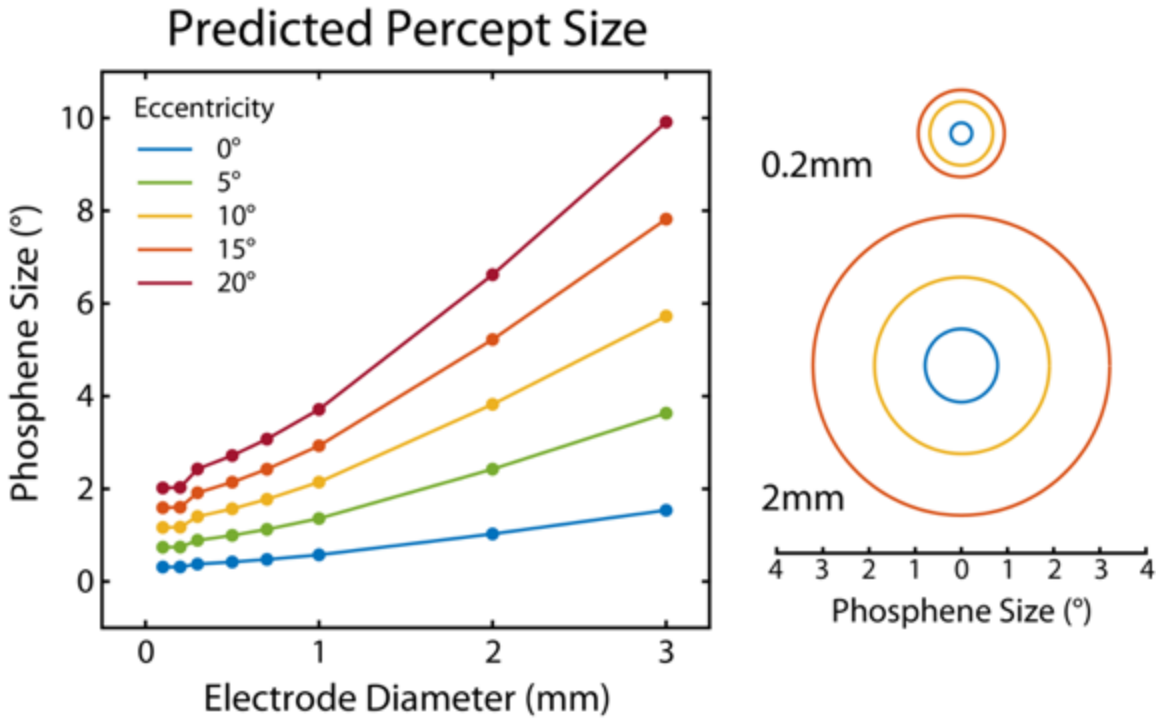

Figure 3.9. Predicted phosphene sizes to be evoked under threshold level stimulation. The plot on the left indicates the upper limit of expected phosphene size that may be evoked with stimulation with a given electrode size and different eccentricates. The right figure provides an example the compares the expected phosphene dimensions at 0, 10, and 15° of eccentricity for electrodes with diameters of 0.2 mm (top) and 2 mm (bottom).

Effects of applied current.

Activated volume. The effect of the amplitude of applied current on activated volume of cortex can be isolated by varying applied current on a static electrode size. This was conducted for an electrode diameter of 0.2 mm (Figure 3.10). At 0.1 mA above threshold the activated volume began to rise sharply. At much higher applied currents, above 0.8 to 1 mA, the extent of activated tissue was found to plateau. Rather than following the trend predicted by Equation 3.14, the volume of activated cortex followed a sigmoid curve with respect to applied current, with a curve fit R^2 of

0.999 and root mean square error of 0.004. The plateau or saturation effect is consistent with repots of saturation in activated current and phosphene size reported in literature (Bosking et al., 2017).

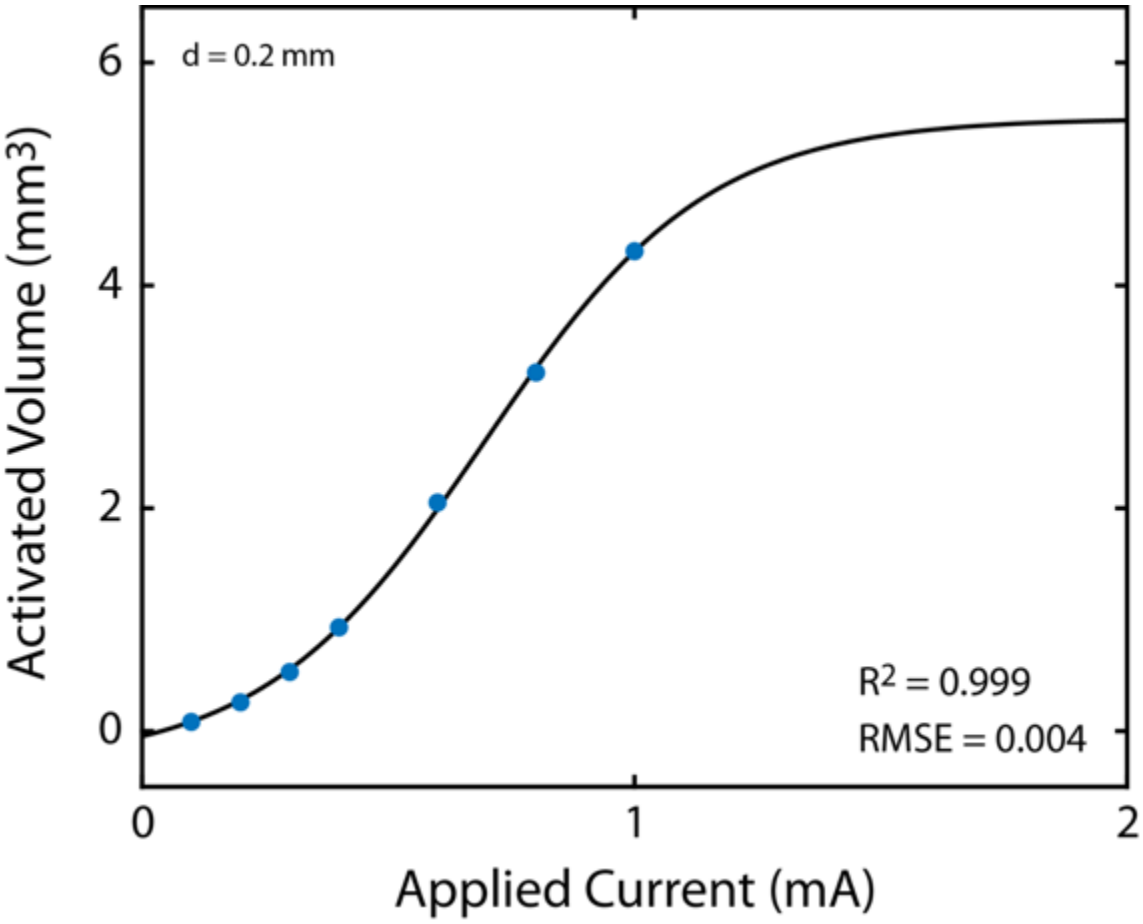

Figure 3.10. Tissue activation in response to applied current. The model predicted measure of tissue volume activated with increasing applied current for a 0.2 mm diameter electrode. Volume of activation spiked rapidly over 0.4 mA and began to plateau for applied currents above 0.8 to 1 mA.

Predicted percept size. With a constant electrode diameter, the upper limits of percept size increased with applied current. However, there is overlap in the expected range of sizes that may be evoked at the range of current evaluated. When current is applied at the threshold range of 0.3 mA, the upper bound of percept sizes maintain relatively punctate nature from foveal to more peripheral eccentricities, with a percept size of 0.24° at center and 0.99° at 15° of eccentricity. With 3.3 times the amount of current, at 1 mA, results in the maximum percept size approximate double

that at threshold, with a 0.48° percept at center and 1.99° percept at 15° of eccentricity (Figure 3.11).

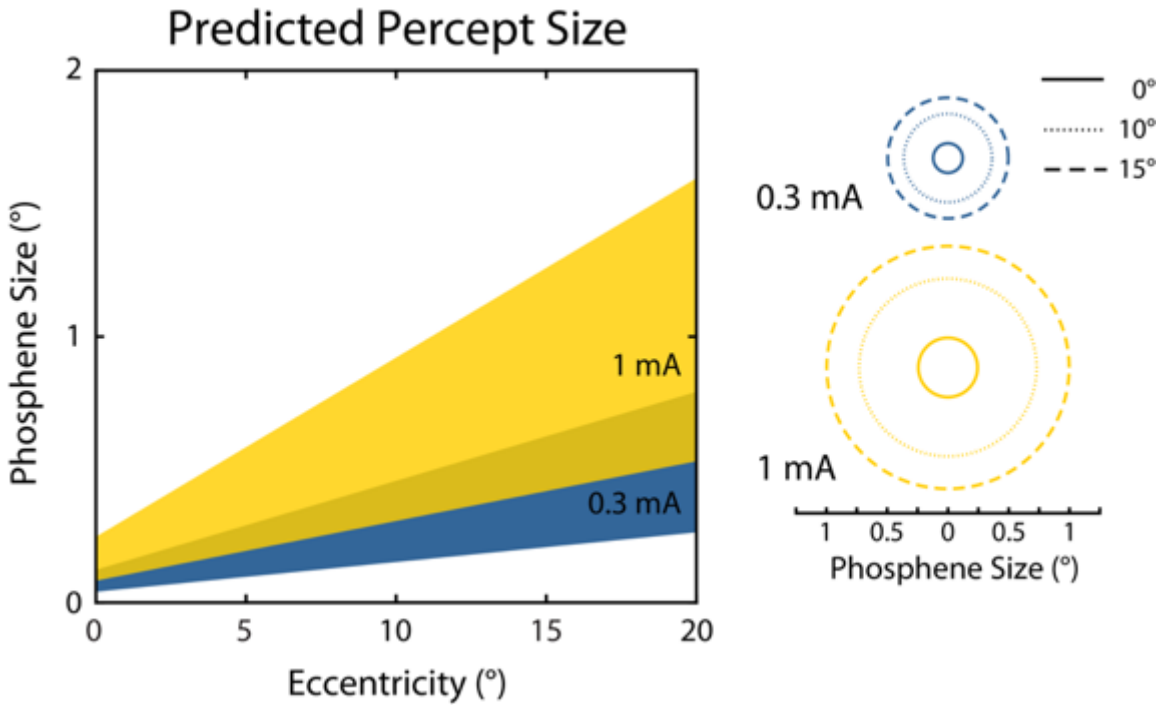

Figure 3.11. Range of predicted phosphene size to be evoked under peri- and supra-threshold stimulation. The plot on the left indicates the upper and lower bounds for expected phosphene size that may be evoked with stimulation on a 0.2 mm electrode at 0.3 (blue) and 1 mA (yellow). The figure on the right provides a comparison of expected phosphene dimensions at 0, 10, and 15° of eccentricity at 0.3 mA (top) and 1 mA (bottom) of applied current.

Cathodal- versus anodal-first stimuli. The polarity of the leading or "activating" phase of the stimulating waveform affects the pattern of activation observed in tissue, despite consistently applied charge density per phase. Observing extracellular potential in tissue as a metric of activation during the cathodal and anodal portions of the stimulus, cathodal-first waveforms tend to activate more tissue proximal to the electrode surface, whereas anodal-first stimuli tend to show more depression proximal to the electrode site and greater activation in a near distal region with slightly increased depth (Figure 3.12).

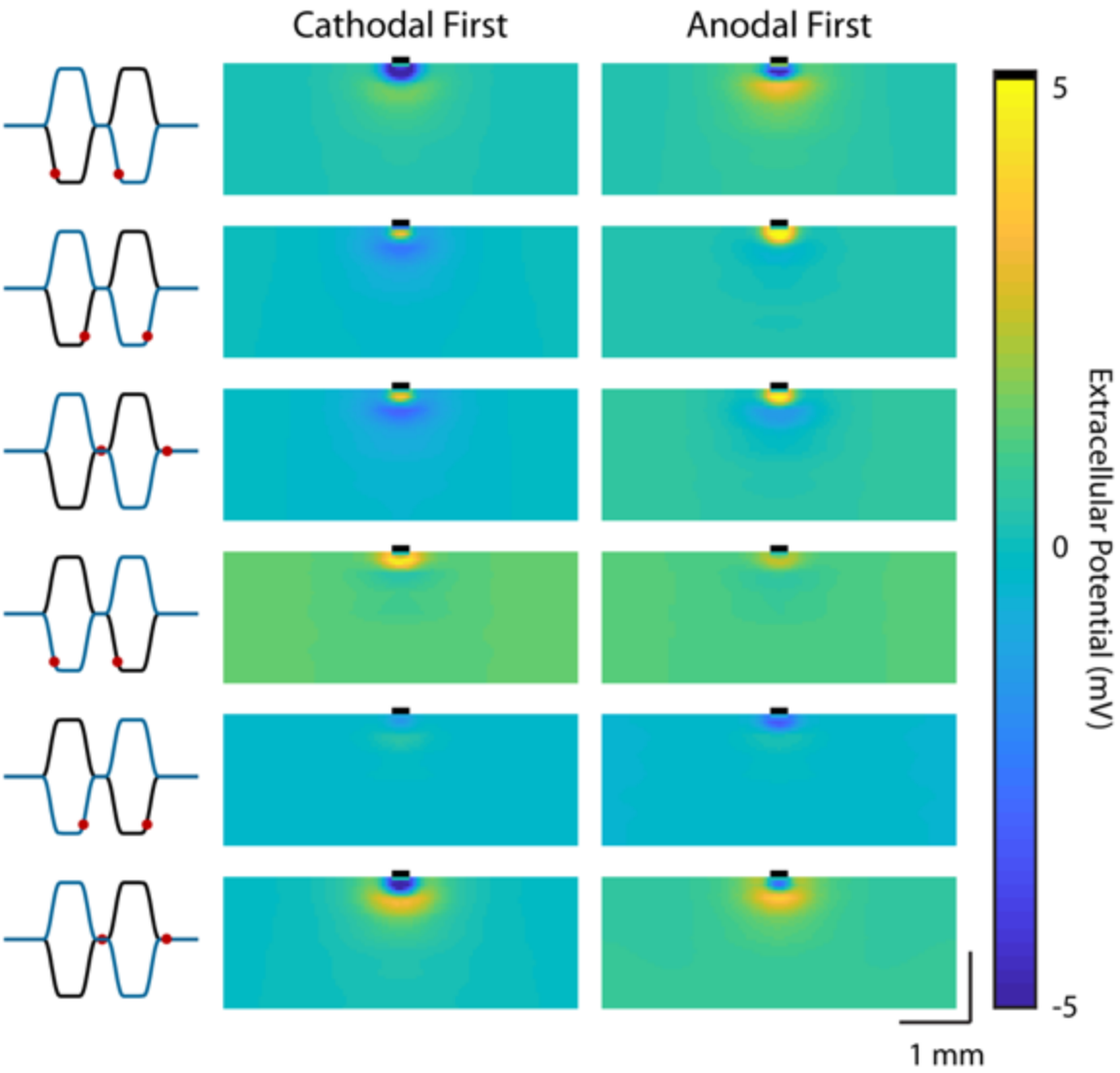

Figure 3.12. Leading phase polarity effect of extracellular potential. Cross sections of extracellular potential during different time points of the applied stimulus. Leftmost column indicates the time course of both cathodal-first (black) and anodal first (blue) stimuli applied in the model with the red dots on either trace indicating the time point reflected in the cross section to the right. Second column shows cross sections during the indicated time points for a cathodal first stimulation paradigm. The right most column provides cross sections of extracellular potential at the indicated time points during the anodal-first stimulation paradigm.

DISCUSSION

Electrode diameter.

Thresholds. To assess whether this model was an accurate representation of epicortical stimulation of striate cortex, model derived perception thresholds were compared with available values reported in literature. The model presented and the threshold selection criteria used could

accurately predict perception thresholds with various electrode diameters. The selection criteria used to predict perception threshold here was a charge density of 30 $\mu C/cm^2$ in Layer II/III. This tracked well with the applied currents known to evoke perception for the larger diameter electrodes (1-3mm) and remained viable for smaller electrode diameters 0.2 mm and 0.5 mm as well. This supports charge density as central determinant in evoking percepts.

Similar charge densities can be achieved within layers II/III for each electrode diameter tested, with the current required to reach that charge density consistently lower for smaller electrodes until the lower plateau in values between 0.1 and 0.2 mm electrodes. Threshold was shown to vary with electrode diameter in accordance a sigmoid function, indicating both upper and lower limits. For smaller electrode diameters, this translates to no additional reductions in current threshold below a certain electrode diameter. The results here suggest this occurs around 0.2 mm in diameter.

Electrodes of size 0.1 and 0.2 required similar current levels to generate sufficient charge density in the desired region while 0.2 mm maintained a lower surface charge density due to the increased surface area. Charge density is known to factor into tissue damage (Cogan, Ludwig, Welle, & Takmakov, 2016), thus minimizing surface charge density is often prioritized when possible, resulting in some industry preference for larger electrodes. However, spatial characteristics of charge density show a comparatively gradual decay in space, thus the extent of tissue subject to potentially damaging levels of charge density is substantially larger with bigger electrodes, particularly over 1 mm. Furthermore, the gradual decay yields heightened activation and more intense virtual sources and sinks throughout the full depth of the simulated tissue, which will likely increased interference with endogenous visual processing occurring in the lower layers of cortex. The smaller electrodes, particularly in the 0.1 to 0.3 mm range, have much larger peak values at the electrode-tissue interface, charge density rapidly drops below both damage and activating thresholds as distance from the electrode increases. The spatial decay of charge density as observed in this model indicates improvements in specificity and extent of tissue damage can be achieved by reducing electrode diameter.

Additional support for safety and specificity improving with reduced electrode size can be inferred from the activated volume. The volume of recruited tissue sees a codependence on electrode diameter and applied current. As current threshold increases with diameter, a sharp increase in activated volume was observed with increasing electrode size. A larger volume activated translates to less focal activation and markedly reduces specificity. Furthermore, larger volumes of tissue simultaneously recruited increases the risk of ictal or seizure-like behavior. This risk is inherently heightened with larger electrodes over 1 mm as the volume of tissue recruited at threshold is substantially larger than that of electrodes smaller than 1 mm. Previous in vivo studies stimulating visual cortex have reported the occurrence of seizure activity following stimulation in the range of 0.75 to 3 mA on 1 mm electrodes (Pudenz, 1993). Minimizing the likelihood of seizure activity is an imperative in the development of stimulating cortical interfaces. Given the relationship between electrode size and affected volume, the more focal sphere of influence with smaller electrodes is advisable.

The predicted percept size increased with electrode diameter, since its metric is dependent on the amount of cortex activated with a given current. At threshold levels, percepts were several times smaller with 0.2 mm electrodes than 2 mm diameter electrodes. This is particularly relevant for a visual prosthesis as smaller percepts can create higher resolution and ego more complex images than possible with a larger percept. Taking into account the cortical magnification factor additionally means percepts evoked at threshold in the periphery will likely be larger than those evoked in the foveal region. Adaptive stimulation may be applied where modulation of the applied current can be used to create more uniform percepts across the visual field space.

Current amplitude. The volume of cortex activated for a given electrode size increased in accordance with a sigmoid function, revealing the initial portion of a plateauing effect at suprathresold current values. Activated cortex is considered proportional to evoked percept size; the plateauing effect between activated cortex and applied current observed in this model is consistent with the saturation in phosphene size reported in an in vivo study (Bosking et al., 2017). With applied current modulating the extent of activated tissue, predicted percept size also ranged with applied current. The model used to predict percept size predicts upper and lower bounds for

a given activated volume and eccentricity. These ranges overlap for peri-threshold and suprathreshold currents. Percept size may be modulated to some extent by manipulating the applied current, with specific current control likely necessary to evoke more normalized percepts across the eccentric range targeted by the prosthetic device.

Waveform leading polarity. The polarity of the leading phase was observed to impact the distribution of activated tissue. The intensity of the responsiveness to either phase was modulated by the sequence in which it was applied. The cathodal leading stimulus saw increased activation proximal to the electrode site, while the anodal leading stimulus evoked increased activity distal to the electrode site, by comparison. The polarity of the activating phase may influence which layers of cortex are more likely to be activated by stimulation. This may allow for improved selectivity in targeting of either the middle or more superficial layers. Whether this translates to any notable change in the evoked perception is not known and will require testing in vivo.

CHAPTER 4

EVALUATION OF CHRONIC EPICORTICAL MICRO-STIMULATION FOR ELICITING VISUAL PERCEPTS IN A BEHAVING PRIMATE

ABSTRACT

Non-penetrating microelectrodes have demonstrated merit for use in decoding neural prosthetics; they may also function well for encoding sensory information. Epicortical microelectrodes cause minimal tissue damage and operate at a behaviorally-relevant cortical column scale. Two consecutive epicortical arrays were implanted in primary visual cortex of a nonhuman primate to evaluate the efficacy of surface level micro stimulation to evoke visual sensations. Current thresholds were notably lower than macro-electrode approaches and maintained consistency across multiple implants and over several months. Photic perception was not observed to be impaired by the consecutive implants or stimulation, indicating no significant deficit from explanation, re-implantation, or stimulation-induced neurotoxicity. Epicortical microelectrode interfaces may provide a stable interface for interacting with neural tissue and provide a viable option for bi-directional BCI applications.

INTRODUCTION

There are an estimated 39 million people in the world living with blindness (Pascolini & Mariotti, 2010). Damage along the visual tract from either trauma or disease results in a variety of deficits with limited treatment options. Fortunately over the last few decades, strides have been made in the realm of retinal prostheses with a slew of devices reaching preclinical and clinical testing, as well FDA and CE approval (Ayton, 2014; Cheng, Greenberg, & Borton, 2017; Humayun et al., 2009; "Intelligent Medical Implants GmBH. IRIS PILOT Extended Pilot Study With a Retinal Implant System," ; Stingl et al., 2017; Troyk, 2017; Winter, Cogan, & Rizzo, 2007). Prostheses interface epiretinally, subretinally or in the suprachorodal space and have been used to restore some limited functional sight in patients with retinitis pigmentosa (RP) and age-related macular degeneration (AMD). These approaches have been shown to increase acuity and improve quality

of life (M. Humayun et al., 2013), however patient populations are limited to those with functional retinal ganglion cells the degradation of which is common in many retinal diseases (Marc & Jones, 2003). Patients with damage upstream from the retina, along the retino-geniculo-cortical tract are also excluded from a retinal approach. A neural prosthetic device providing stimulation of the visual cortex may restore some visual function to the profoundly blind when retinal stimulation in not a viable option.

The cortical approach for a vision prosthesis relies on the capacity for electrical stimulation of primary visual cortex (V1) to consistently evoke the perception of phosphenes. The foundation for this concept has been previously validated in studies using large epicortical electrodes with surface areas .47 – 3 mm^2 (G. Brindley & Lewin, 1968; G. S. Brindley & Rushton, 1974; Dobelle, Quest, Antunes, Roberts, & Girvin, 1979; Lewis & Rosenfield, 2016). While these studies were able to evoke phosphene and in some cases simple patterns of light (Schmidt et al., 1996), certain fundamental limitations could not be overcome. The large electrode surface area of the electrodes used resulted in high current thresholds, some electrodes required currents up to 8.1 mA (Dobelle, Quest, Antunes, Roberts, & Girvin, 1979). Stimulation sometimes resulted in pain felt on the scalp or deep in the head. The sensations evoked were described as unnatural and in cases with high currents applied, multiple spots of light occurred, or the sensation lingered for minutes following cessation of stimulation. The relatively large cortical areas being stimulated at high current levels also brought about concerns of evoking seizures (Goddard, McIntyre, & Leech, 1969), additionally limiting their capacity for concurrent multi-site stimulation.

For a visual prosthesis to be clinically relevant necessitates the use of high density electrode arrays that can consistently and safely induce phosphene patterns representative of a visual scene (Christie, Ashmont, House, & Greger, 2016). High-count microelectrode arrays, which interface with cortex at a physiologically relevant cortical column scale, could provide an effective platform for this purpose. Recent approaches in neural prosthetics have employed intracortical microelectrodes for their low current thresholds and high specificity in targeting cell populations (Davis et al., 2012; DeYoe, Lewine, & Doty, 2005; Normann, Maynard, Rousche, & Warren, 1999; Schmidt et al., 1996; Torab et al., 2011; Troyk, 2017). Intracortical arrays like the Utah array

(Blackrock Micorsystems, Salt Lake City, Utah) consist of closely spaced penetrating electrodes and directly target deeper cortical layers (Rousche & Normann, 1998).Since intracortical arrays terminate directly near their targeted cell population they can provide more directed and localized stimulation at lower levels compared to surface stimulation. Surface electrodes will need to stimulate a larger volume of cortex to reach activate the targeted populations of neurons in similar layers of cortex, as such larger currents will be required. Previously studies reported visual percepts evoked with intracortical simulation as low as 1.9-25μA (Schmidt et al., 1996; Torab et al., 2011), however, stimulation of a few hundred micro-amps via several electrodes was routinely required, with thresholds increasing after several months of implantation before maintaining consistency (Davis et al., 2012; Torab et al., 2011). This decline is likely related to encapsulation and tissue damage associated with intracortical arrays. Greater tissue damage has been reported with intracortical than epicortical electrode arrays. Observed damage includes tissue dimpling, inflammation, foreign body response and encapsulation, decreased neural density near the electrode site, and persistent activation of microglia, potentially leading to neurotoxicity (Polikov, Tresco, & Reichert, 2005). This effectively reduces the long-term viability of penetrating arrays and contributes to the increase in current required to evoke perception after chronic implantation. There is comparatively less documentation of the tissue response to chronically implanted epicortical arrays; however, because they do not penetrate the pial surface it is likely the foreign body response will be reduced (Christie, Ashmont, House, & Greger, 2016). Epicortical stimulation will likely be capable of evoking photic responses after a longer duration in vivo at more consistent thresholds. This is supported by analogous studies with chronically implanted epiretinal microelectrode arrays that have seen functional responses to stimulation after five years of implantation inhuman subjects (Humayun et al., 2013).

Array geometries pose additional considerations for damage and accessibility. Implanting intracortical arrays requires delicate manipulation as it pierces the parenchyma. Current intracortical arrays can be placed manually, but are more commonly placed with a pneumatic inserter (DeYoe, Lewine, & Doty, 2005; Normann, Maynard, Rousche, & Warren, 1999; Polikov, Tresco, & Reichert, 2005). Even with carful insertion, implantation typically causes tissue damage

(Polikov et al., 2005), which likely affects thresholds and tissue response. Conversely, epicortical arrays are more easily placed and repositioned, and cause comparatively minimal tissue damage (Christie, Ashmont, House, & Greger, 2016; Matsuo et al., 2011). For these prosthetic systems surgical implantation techniques are further complicated by the geometry of primary visual cortex. A large portion of V1 exists within the calcarine sulcus and sagittal fissure. Successful sulcal implantation of penetrating arrays is unlikely, limiting potential visual field representations. Flat epicortical arrays can be readily placed in the sagittal fissure and potentially within the calcarine. Access to these cortical surfaces could allow more complete representation of the parafoveal and peripheral visual field (Christie et al., 2016).

While intracortical microelectrodes provide optimal localization of activation and low current thresholds, successful sulcal implantation of penetrating electrodes is unlikely. Although the specificity and current thresholds for an epicortical array are inherently higher than an intracortical approach, using microscale electrodes will likely provide a significant improvement over macroscale electrodes while allowing access to cortical structures inaccessible to intracortical arrays. Epicortical microelectrode arrays can have similar spacing a form factors as intracortical microelectrode arrays but terminate in disk electrodes that sit on the cortical surface. These nonpenetrating microeelctrodes have been shown to interface with cortex at a similar scale to intacortical microelectrodes (Kellis, et al., 2016) and may provide a viable alternative for chronic micro-stimulation. While studies have evaluated the efficacy and limitations of intracrotical microsimulation (Torab, et al., 2011; Normann, Maynard, Rousche, & Warren, 1999; Davis, et al., 2012; DeYoe, Lewine, & Doty, 2005; Bartlet, et al., 2005), none have thoroughly explored the capacity for efficacious treatment via epicortical microstimulation (ECMS).

Experimental data suggests micro electrodes are capable of targeting tissue 2-5 times the largest exposed electrode dimension (Cogan, Ludwig, Welle, & Takmakov, 2016). With this, there is a necessary trade-off between electrode diameter and depth of tissue activation. Larger electrodes will be able to activate deeper cortical layers but require higher currents to maintain charge density, whereas smaller electrodes will have higher specificity but electrodes with too small of diameter may not be able to sufficiently activate the necessary layers. Intracortical studies

typically target cortical layers within the range 2-4 in part because direct stimulation of these layers have the lowest threshold for evoking visual percepts (DeYoe, Lewine, & Doty, 2005) and primarily because these layers could be useful for restoring vision as they include the termination of the geniculocortical projections (layer 4) and the origins of the cortico-cortical projections to higher level visual processing areas (layers 2/3) (Purves, et al., 2008). Surface level microstimulation will likely be able to target the more superficial cortical layers 2/3. Ideally, the smallest smallest diameter at which percepts can be elicited with be used, so that the benefits of microscale electrodes can be maximized.

Given the potential benefits of a non-penetrating, micro-scale approach, this study proposes a systematic verification and validation of the capacity for surface level microstimulation to evoke visual percepts with chronic implantation.

MATERIALS AND METHODS

Grid design. An epicortical array featuring concentric rings was designed and produced in tandem with Second Sight Medical Products (Sylmar, CA 91342, USA). The array consists of 46 electrodes. The center electrode for each grouping has an exposed area of 200μm. Each concentric ring is composed of these 200μm electrode pads electrically tied together. The concentric rings are composed of 6, 12, or 18 electrode pads, creating effective diameters of 750μm, 1500μm, and 2100μm. The array has a length of 13.84 mm and height of 9 mm. Groupings have a spacing of 2.12mm from ring center to center. Four rings with increasing eccentricity across the midline of the array contain each of the four electrode diameters; all remaining groupings contain the center electrode, the 6-ring, and the 12-ring (Figure 3). The array was potted to a titanium base with ZIF clip connector. The pedestal base is used as ground.

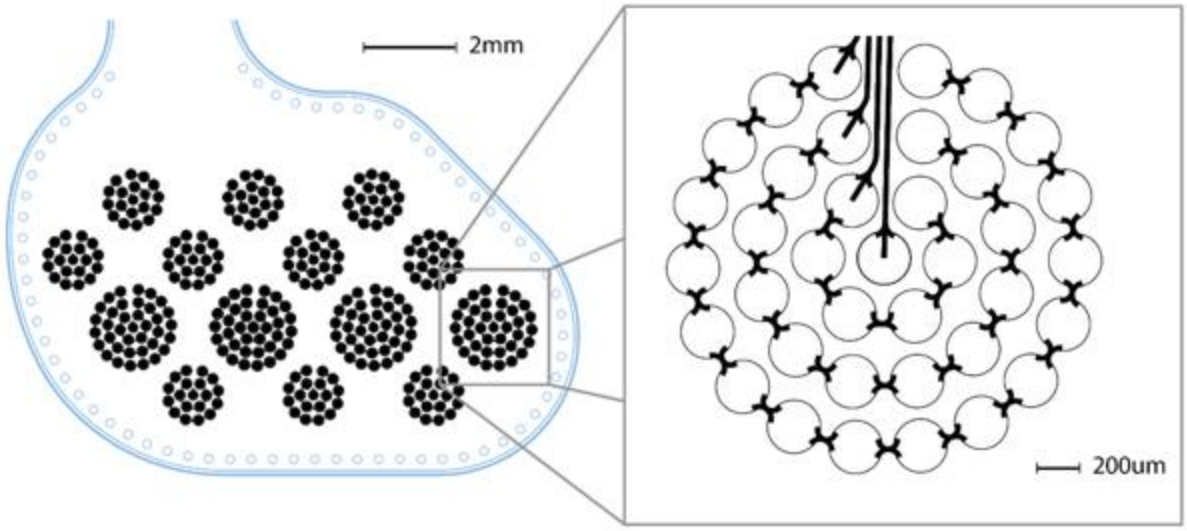

Figure 4.1. Custom array design with concentric rings. Array allows for probing thresholds and percept characteristics while accounting for variations with eccentricity and maximizing spatial landscape of the array. Rings made up of 1-, 6-, 12-, 18-disk groupings and provide electrode diameters of 200, 800 1400 and 2000μm.

Subjects and surgery. One adult male rhesus macaques (Macaca Mulatta) will be used in this study, NHP1. NHP1 was implanted with the epicortical array described above. The array was placed in the sagittal fissure facing the right hemisphere, with the caudal-most point of the array placed in close approximation to the pole, superior to the calcarine fissure. Human protocols were followed during surgery and post-operative care.

Threshold detection task. This task is used to determine the luminance threshold for detection of photic stimuli as well as current thresholds for perception of electric stimuli. The NHP is placed in a primate chair inside of a dark chamber, facing a CRT monitor. The subject is required to place each hand on a capacitance switch, one to the left and the other to the right. A small red dot (.1X.1 visual degrees) at the center of the CRT screen was used for a fixation point. Once the NHP directs its gaze within one degree of the center point, an auditory tone signals the start of the trial. The NHP must maintain eye fixation for 400ms before a stimulus, either photic or electric, is presented. Electric stimuli are described below. Photic stimuli were round, monochromoatic Gaussian shapes with a diameter of one visual degree. Luminance levels are varied between 10 and 60 cd/m^2 in 5 cd/m^2 increments and presented on a screen with background luminance of 10

cd/m^2. Photic stimuli are presented for 300ms. Following a hold duration of an additional 300ms, a second, unique auditory tone cues the NHP to respond. The NHP responds by removing its right hand to indicate that it did not perceive, or its left hand to indicate that it did perceive a stimulus. Photic threshold trials are rewarded with a bolus of water 50% of the time regardless of response. Clearly visible or invisible catch photic trials are used to ensure that the animal is responding correctly; rewarded is given only if the correct response is made. Catch stimuli are presented in 30% of trials. LabView (National Instruments, Austin, TX) is used to control task flow and monitor session progress. Visual stimuli are generated using a real-time visual stimulator (ViSaGe, Cambridge Research Systems, Rochester, Kent, England) and displayed on a CRT monitor (G90fb, ViewSonic, Walnut, CA). The NHPs are head-fixed using a minimally invasive technique and eye positions is tracked with an infrared camera (EyeLink 1000, SR Research, Mississauga, ON, Canada). Behavioral and neural data are collected using a Cerebus NeuroPort System (Blackrock Microsystems, Salt Lake City, UT, USA) at 10kHz. Data collection is conducted daily in 2 hour sessions.

Two-point discrimination task. This task is used to determine whether certain parameters evoke more than one percept as well as evaluate the distance at which stimulation on neighboring electrode produces separate percepts. The task will proceed with in a similar sequence to the threshold task previously described. The subject will place both hands on capacitive switches to indicate trial start. Following fixation within 1 degree of the fixation point displayed, either photic or electric stimuli will be presented. Photic stimuli will be Gaussian pulses presented on a CRT screen. Each trial will present either one or two pulses of light, the latter having a randomized variable distance between stimuli centers. The minimum distance at which photic pulses can be differentiated will be determined. Electric stimuli will be presented simultaneously on two electrodes or simultaneously on two groups of concentric electrodes. The animal will respond to indicate one stimulus observed by lifting his left hand and respond to indicate two observed percepts by lifting his right hand.

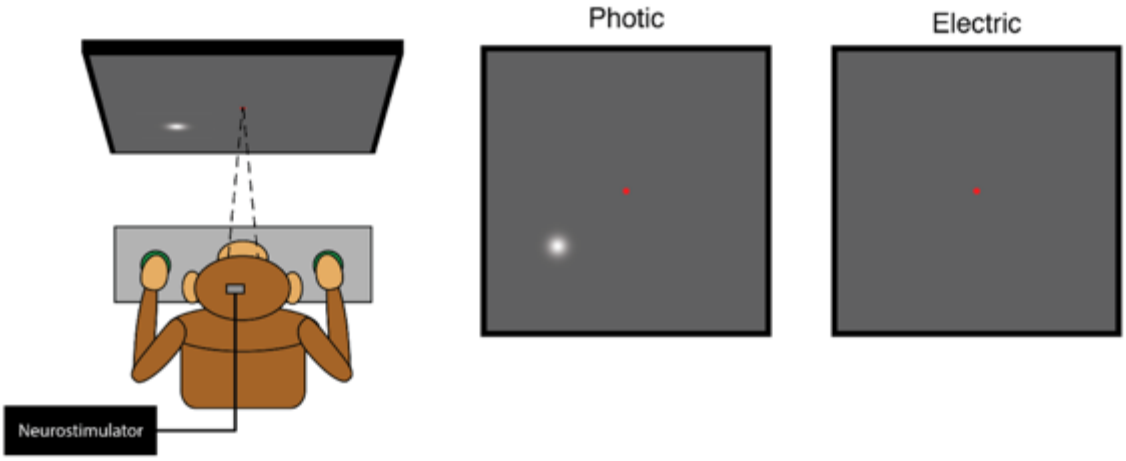

Figure 4.2. Task setup for all experiments. Non-human primate subjects are seated, head-fixed, facing a CRT monitor. Photic stimuli are present on monitor. Electric stimuli are delivered via an IZ2 neurostimulator with no photic stimuli presented on monitor, fixation point is maintained.

Recording and stimulation. Recordings were conducted with a 128-channel Neural Signal processor (Blackrock Micro Systems). Stimulation experiments use an IZ2-128 stimulator (Tucker-Davis Technologies, Alachua, FL). The stimulator is capable of delivering 300μA to 128 channels. To achieve higher current levels, up to 3mA, a custom adder box was developed. Pulse trains consisted of symmetric, cathode-first, biphasic waveforms. The initial interphase interval and phase duration are set at 100μs and 600μs respectively, with pulse frequency and train duration set at 300Hz and 300ms.

Determining electric thresholds. Electric stimuli were applied at 100μA increments from 0-900μA and consisted of 5-40% of trials within a daily session, the reminder consisting of photic trials. At least one photic trial separated each electric trial to limit the effect of prior stimulations on the raw threshold collection. The amplitude of the current was applied randomly between the specified values. For each session, responses to stimulation were fitted with a sigmoid curve, with the threshold determined to be the point at which the fitted curve passed 80%.

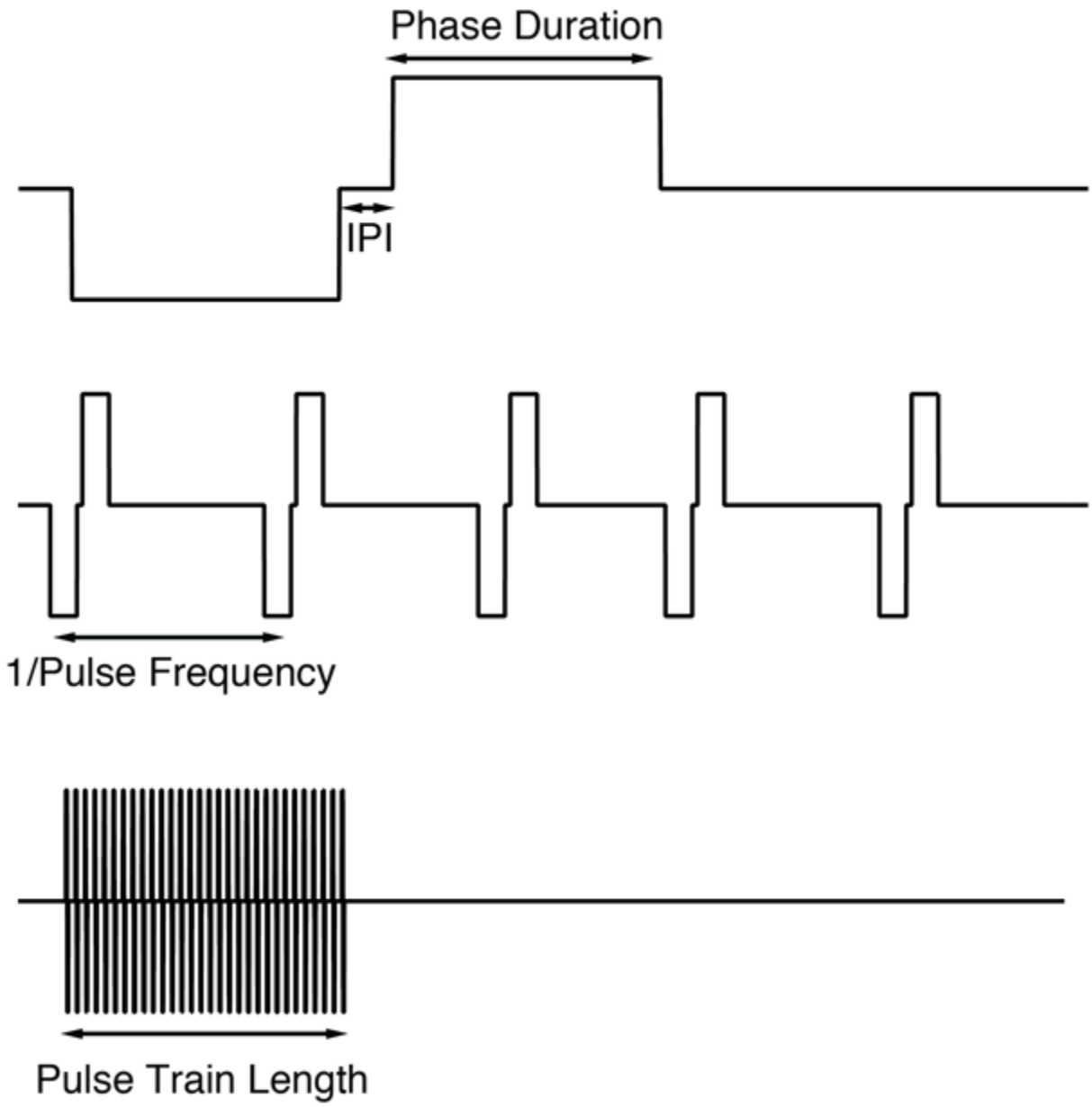

Figure 4.3. Waveform Parameters. Definitions of waveform parameters used, phase duration, pulse frequency, and pulse train length.

Data collection. Data was collected daily in sessions lasting up 3.5 hours. Sessions including electric stimulation were conducted most days, with gaps occurring for collection of receptive field data and photic behavioral data baselines.

Tissue damage metric. The Shannon model for tissue damage was used a baseline determinant of whether threshold level stimulation would result in damage. Charge per phase Q is

determined by the product of the pulse width pw and the current amplitude I of the determined threshold value.

$$Q = I * pw \quad (4.1)$$

The charge density CD is the calculated by dividing the charge per phase by the geometric surface area A of the stimulating electrode.

$$CD = Q/A \quad (4.2)$$

The damage threshold is set by a logarithmic relationship between the charge density and the charge per phase, modulated by a constant k. The k value chosen as a commonly accepted damage limit was 1.86 (S. Cogan et al., 2016).

$$\log\left(\frac{Q}{A}\right) = k - \log(Q) \quad (4.3)$$

The equation was rearranged to calculate Shannon k values for the determined perception thresholds to determine whether individual stimulation combinations would be considered to cause tissue damage.

RESULTS

Perception thresholds and behavioral responses to stimulation. Epicortical micro-stimulation on individual 200µm electrodes consistently evoked behavioral responses indicating perception of visual stimuli. Thresholds were collected on eleven of fourteen electrodes on implant one. A failure on the percutaneous connector limited further testing. For implant 2, thresholds were collected for thirteen of the fourteen 200µm electrodes on the array, as one electrode (D2) was non-functional. Initial thresholds were calculated from twelve of the thirteen functional electrodes, since one electrode (B1) did not evoke any behavioral responses at the time of initial threshold collection. This electrode did begin evoking responses later in the study and is included in the terminal averages. The average 80% threshold across the arrays were 441µA for implant 1 and 324µA for implant 2, based on data collected during sessions from two to four weeks post implant. Data collected from 8 to 8.5 months post implant yielded an array average of 316µA for implant 2 (Figure 4.4).

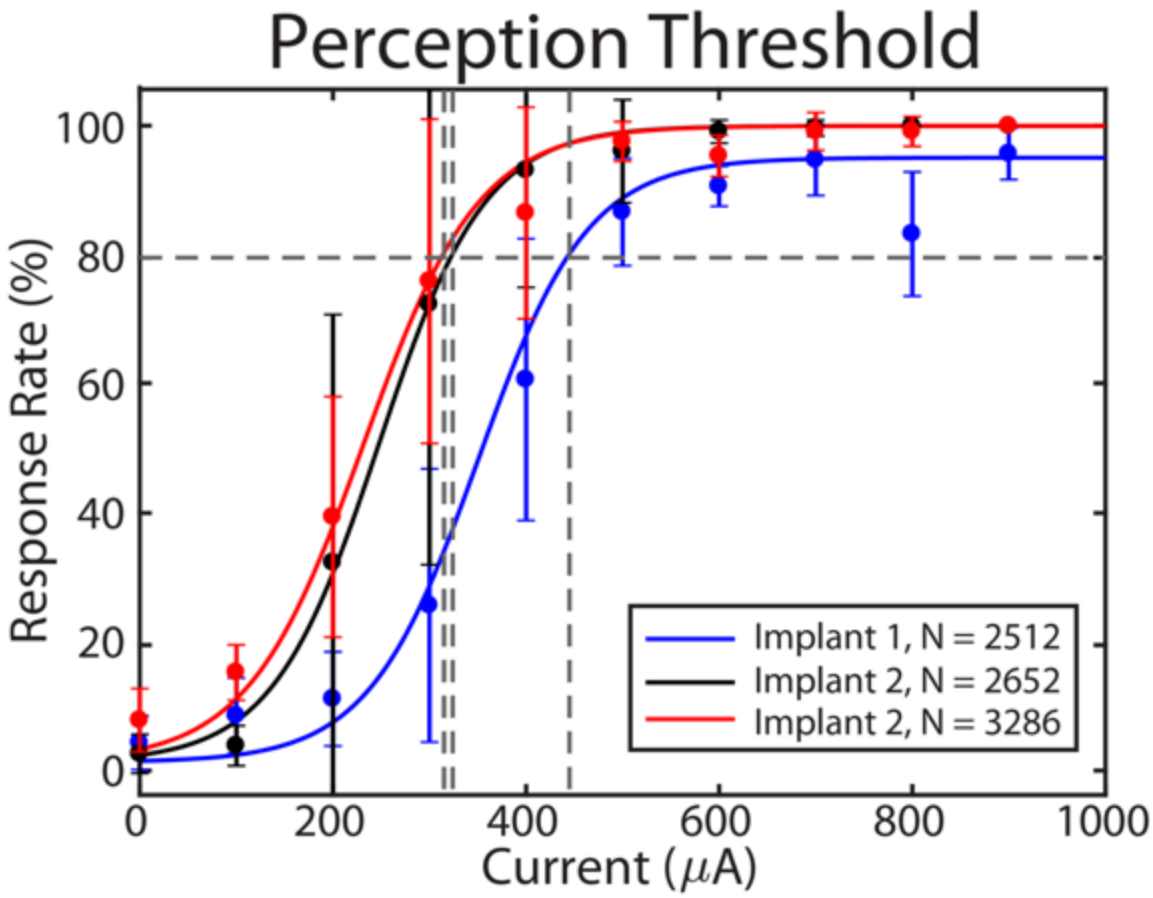

Figure 4.4. Perception thresholds at 80% detection rate for 200µm electrodes. A. Thresholds for perception, determined by fitting sigmoid to data and finding 80% point, presented for 200µm electrodes. Red trace represents array thresholds for the first implant, black and blu are both thresholds collected for implant 2. Black indicates thresholds collected within the month following implantation, blue represents thresholds collected between 7 and 8 months post-implant.

Parameter variation. Systematic parameter variation was conducted to validate basic electro-physiological relationships and establish a range of working parameters for functional stimulation to evoke visual sensations. Threshold results for all parameter variations conducted are available in Table 1. Pulse frequency in the range of 100-400 Hz showed a slight trend of increasing threshold with decreasing frequency, threshold increased and overall response rate decreased with a pulse frequency of 50 Hz. No significant correlations were noted with varying inter-phase interval. A clear and expected positive correlation phase duration and threshold was observed.

Table 4.1

Parameter Variation Effect on Threshold

Pulse Frequency

Frequency	Threshold (μA)	Count
100	368	232
200	268	220
300	287	177
400	269	109

Inter-Phase Interval

IPI (ms)	Threshold (μA)	Count
0.1	287	177
0.3	297	157
0.4	342	224
0.5	313	231

Phase Duration

Phase Duration (ms)	Threshold (μA)	Count
0.1	800	159
0.2	500	212
0.3	366	195
0.4	282	205
0.5	290	249
0.6	287	199
0.9	287	177

Stability over time. ECMS on the array consistently evoked visual percepts without large increases in perception threshold. Semi-monthly thresholds collected on implant 2 electrode C2 showed consistent perception thresholds over a 8-month period, with an average of 307.3±22.7μA (Figure 4.5). The initial threshold was 287μA and final threshold was 289μA. The lowest threshold collected for this electrode was the first point, the highest threshold was 344μA, collected 198 days post implant, and 59μA larger than the initial threshold collected. Initial and end-point thresholds across all electrodes on the array were not significantly different (two sample t-test, $p<.05$).

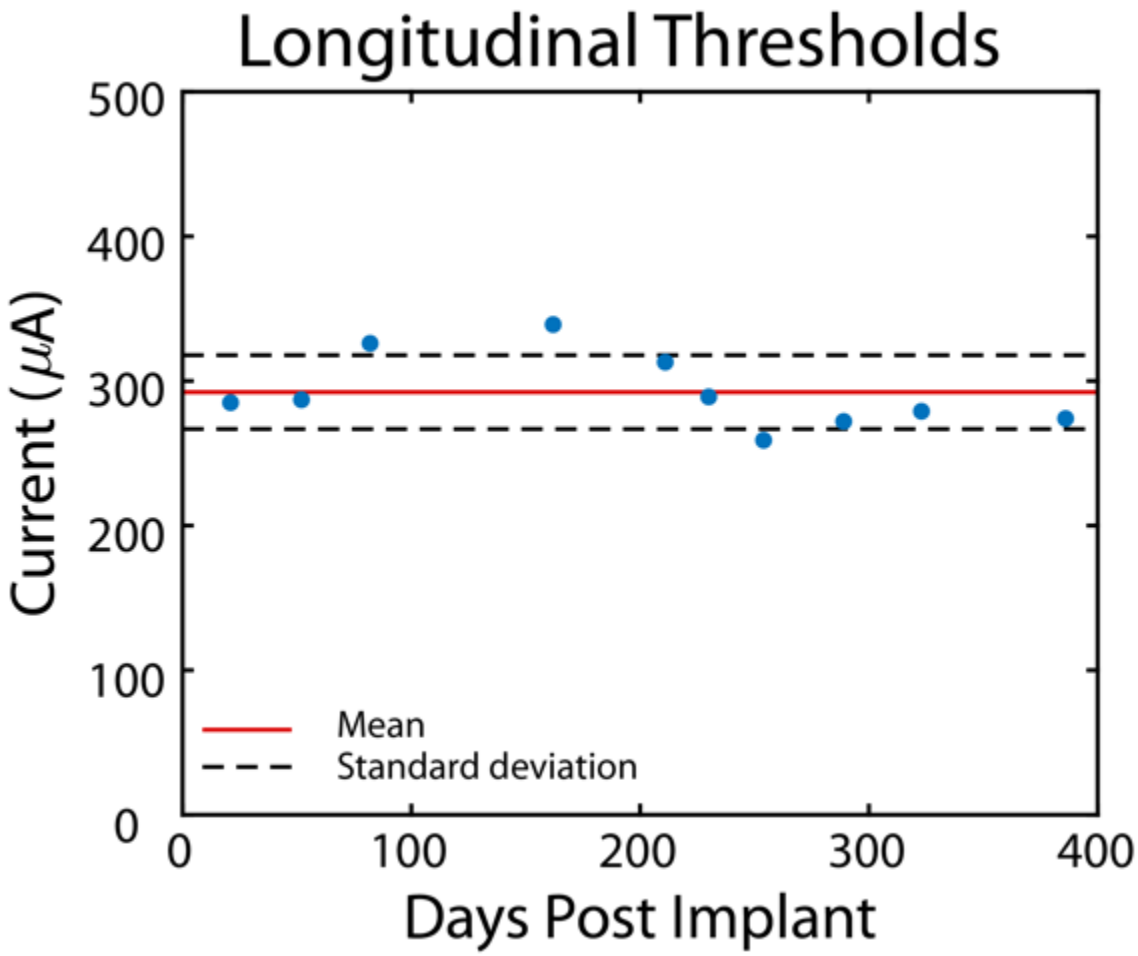

Figure 4.5. Threshold stability over time for NHP1 implant 2. Data reported for electrode C2 on implant 2, with thresholds collected up to 416 days after the date of implant of the second array. The final threshold collected was 4μA more that the initial threshold. The highest threshold collected was 59μA more than the lowest threshold collected for this electrode.

Neural recordings collected at various time points over several months post-implant reflect consistent signal quality over time. Traces reflecting signals collected 10, 55, and 175 days post implant and their corresponding frequency spectrums indicate no notable decline in electrode or neural viability (Figure 4.6). Presented traces each collected from a ten second window during which the NHP was awake but not actively performing the task.

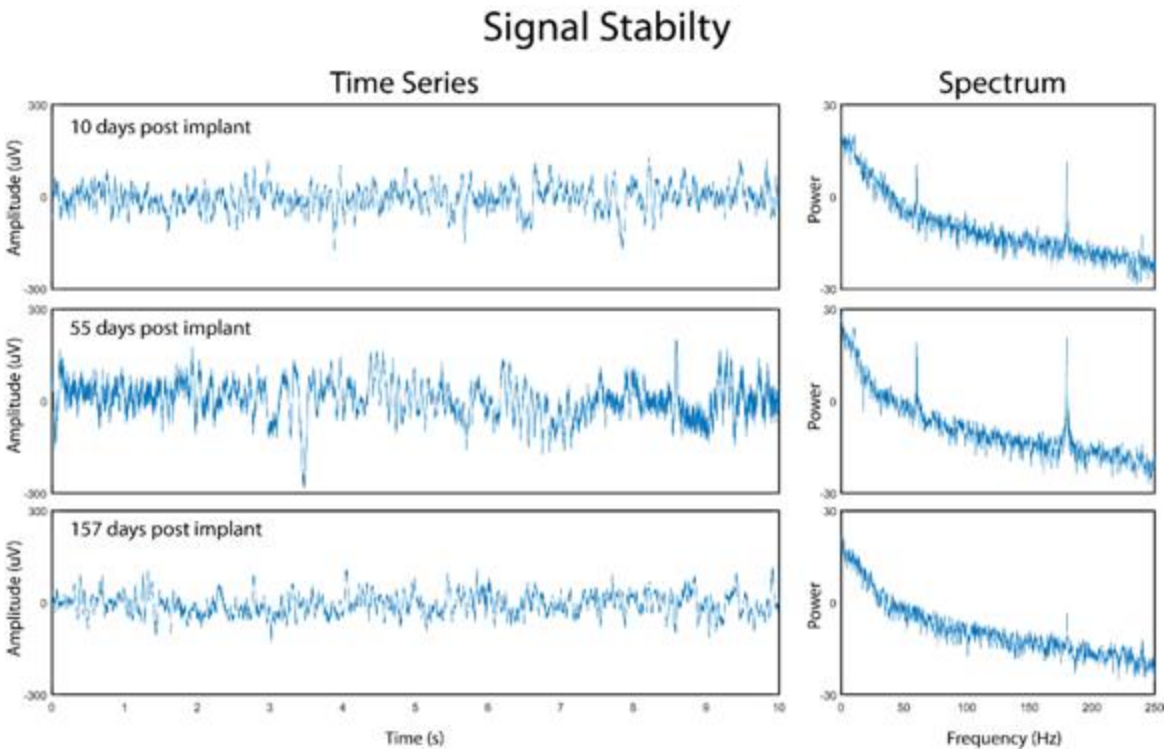

Figure 4.6. Signal stability over time for NHP1 implant 2. Voltage traces and the corresponding spectrum taken from a single 200µm electrode (channel 5) at several points in time post implant 2. Signals taken from resting a period between trials on each day shown.

Impedance values were consistent over time and across both implants. Daily impedances values collected for both implant 1 and implant 2 show a slight increase in impedance over the first month to 40 days of implants, followed by level values for the remaining duration of implant (Figure 4.7). Data was collected for 150 days post implant 1 and 160 days post implant 2. The average impedance across all 200µm electrodes over all days of collection was 14.5±1.11kΩ for implant 1 and 13.37±1.14kΩ for implant 2.

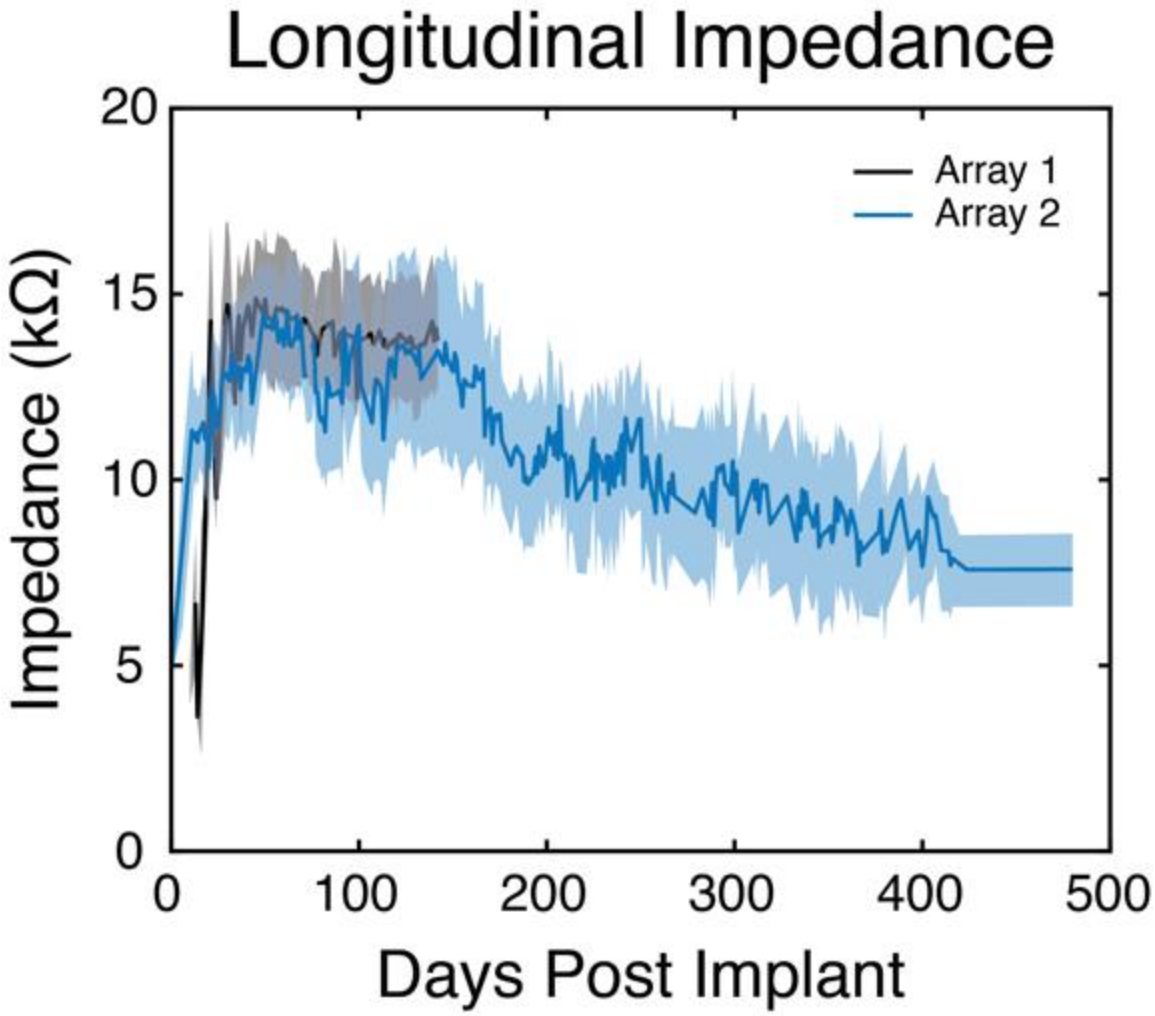

Figure 4.7. Impedance values over time for NHP1 implant 1 and implant 2. Values shown in red for Implant 1 and blue for Implant 2. Impedances were collected at the end of most experimental sessions. Data represents up to 150 days post implant 1 and 160 days post implant 2. Both arrays maintain similar impedance values for 200μm electrodes and follow similar temporal trends.

Charge-based safety factors. Thresholds collected for pulse width durations from 0.1 ms to 0.8 ms were used to create perception level strength and charge duration curves for stimulation trains pulsed at 300Hz for 300ms on one electrode (Figure 4.8). Rheobase was determined to be 502μA, and chronaixe at 0.185ms. Minimum charge was 82nC.

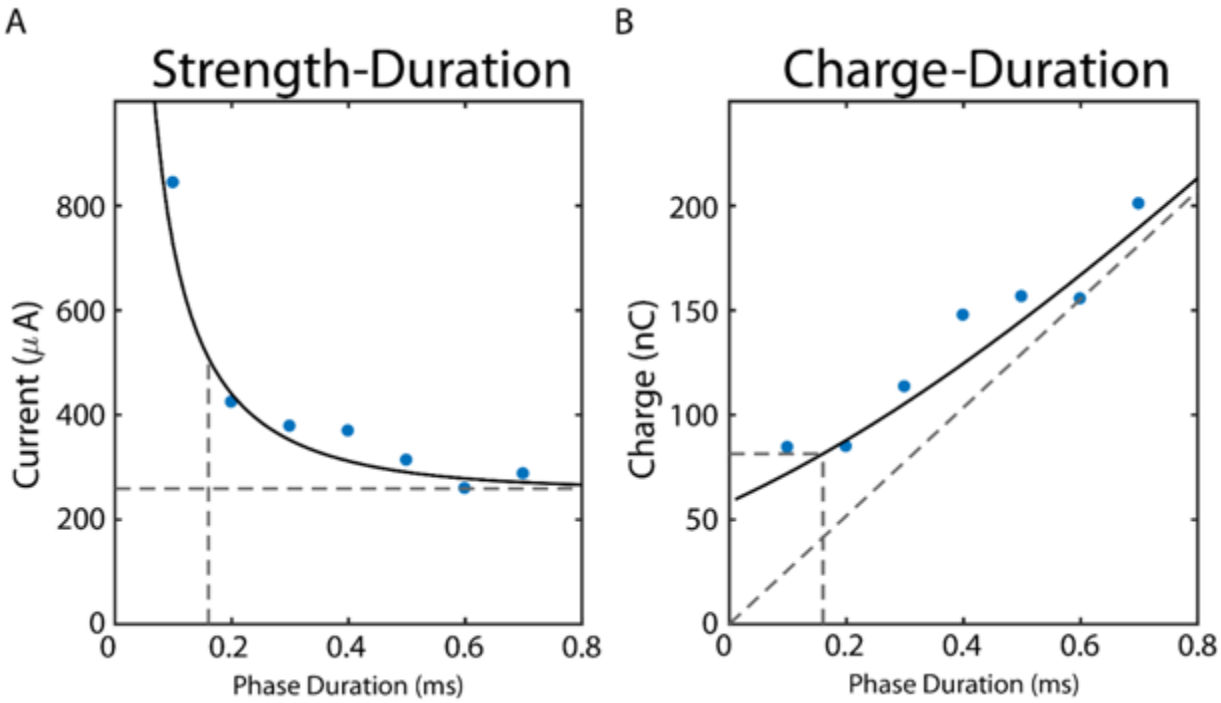

Figure 4.8. Strength and charge duration curves collected based on 80% perception thresholds. A. Current thresholds for each tested phase duration. Solid black line is the current threshold calculated in accordance to its relationship to measure rheobase and an assumed time constant. B. Charge duration curve at threshold values with calculated minimum current. Each trial conducted consisted of 300 Hz pulse frequency and 300ms train duration.

Shannon model values for charge per phase – charge density based metric of tissue damage for 200μm diameter electrodes are shown in Figure 4.9. The charge per phase to charge density relationships for perception thresholds fell below damaging levels for stimulaiton with pulse widths less than 0.5ms in duration, for a k of 1.86. Stimulation with both 0.6 and 0.9 ms duration pulse widths had threshold currents that exceeded the Shannon safety metric. The calculated k values rise with pulse duration. The increase in k value between 0.2ms to 0.4m sis incremental. The remaining changes in k value are quasi-linear and larger in amplitude.

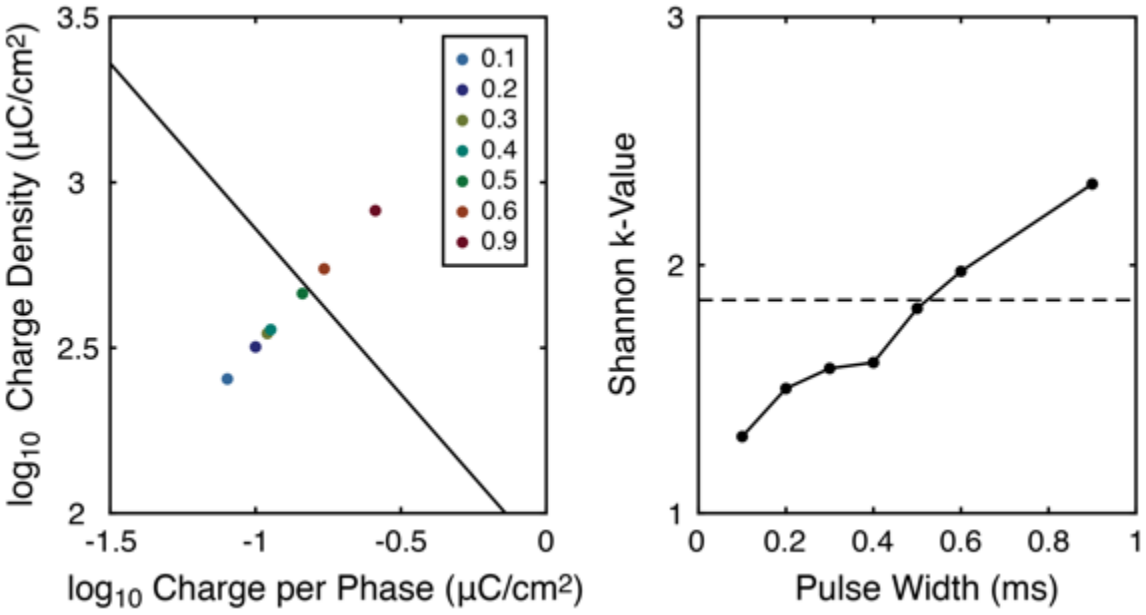

Figure 4.9. Shannon model comparison for visual percept threshold values with varied pulse widths. The left plot indicates the charge per phase to charge density relationship for perception thresholds at different pulse widths. Stimulation with pulse widths less than 5ms in duraiton did not exceed damage metrics with a k of 1.86. Right indicates calculated k values for thresholds colelcted at each pulse width. Stimulaiton with pulse widths less than 0.5ms resulted in k values below the 1.86 damage level.

Interference with endogenous visual processing. As this is a continuing study, no histological data has been collected at this point. In lieu of histology, responsiveness to photic stimuli in and around the area of implant has been used as a metric of gross damage. While this does not provide cellular level indicators of tissue health, it does provide a baseline in terms of functional deficits. Pre-study values were collected before the first array was implanted. Post-study values were collected after 16 months of stimulation and implantation of two arrays, before explanation of the second array. Pre and post study values were each averaged from five sessions, with values weighted by session counts for each luminance. At all luminance values tested, NHP1 responsiveness was not reduced after the study (Figure 4.10).

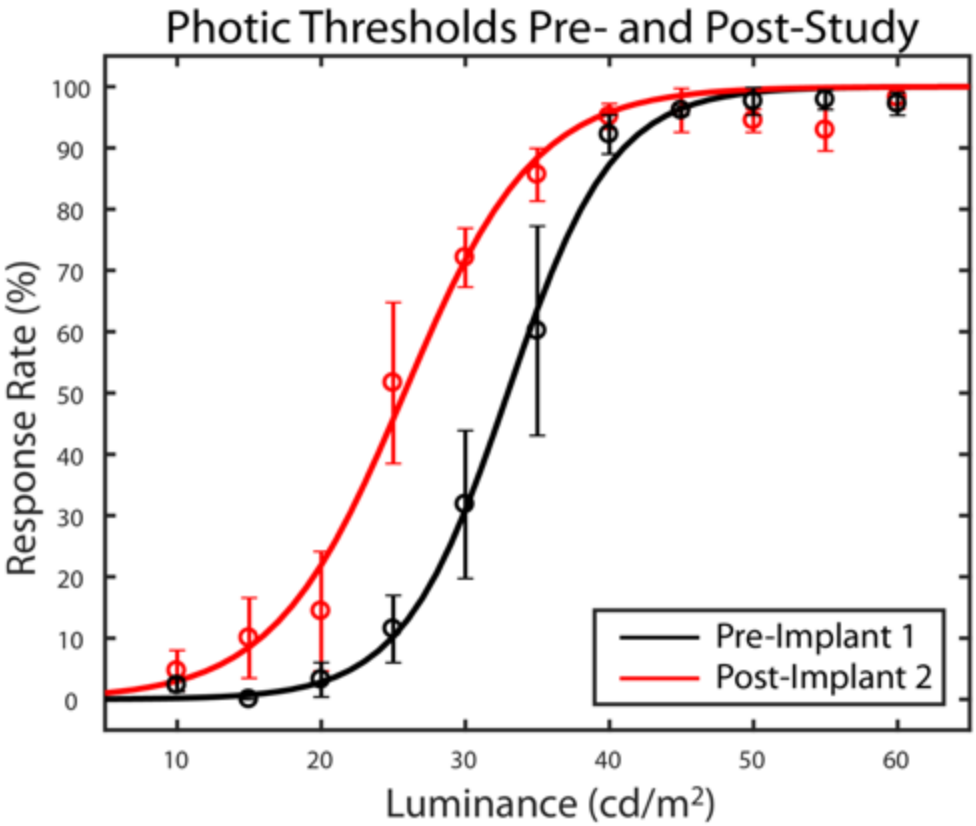

Figure 4.10. Photic psychophysics pre- and post-study for NHP0 and NHP1. A. NHP0 photic responses pre and post study, showing no significant changes in photic perception. B. NHP1 responses to photic stimuli with varied luminance. Significant changes observed in middle ranges of luminance, with perception of lower intensity values perceived at greater rates at the end of the study.

Responsiveness to photic stimuli in 500ms following cessation of electric stimulation was used to characterize the temporally lingering effects of stimulation on endogenous visual processing. Psychophysics indicates no significant divergence in responsiveness to photic stimuli when electrical stimulation is applied at peri-threshold to twice threshold amplitude. Reduction in responsiveness was noted in the condition operating around three times the threshold in amplitude (Figure 4.11).

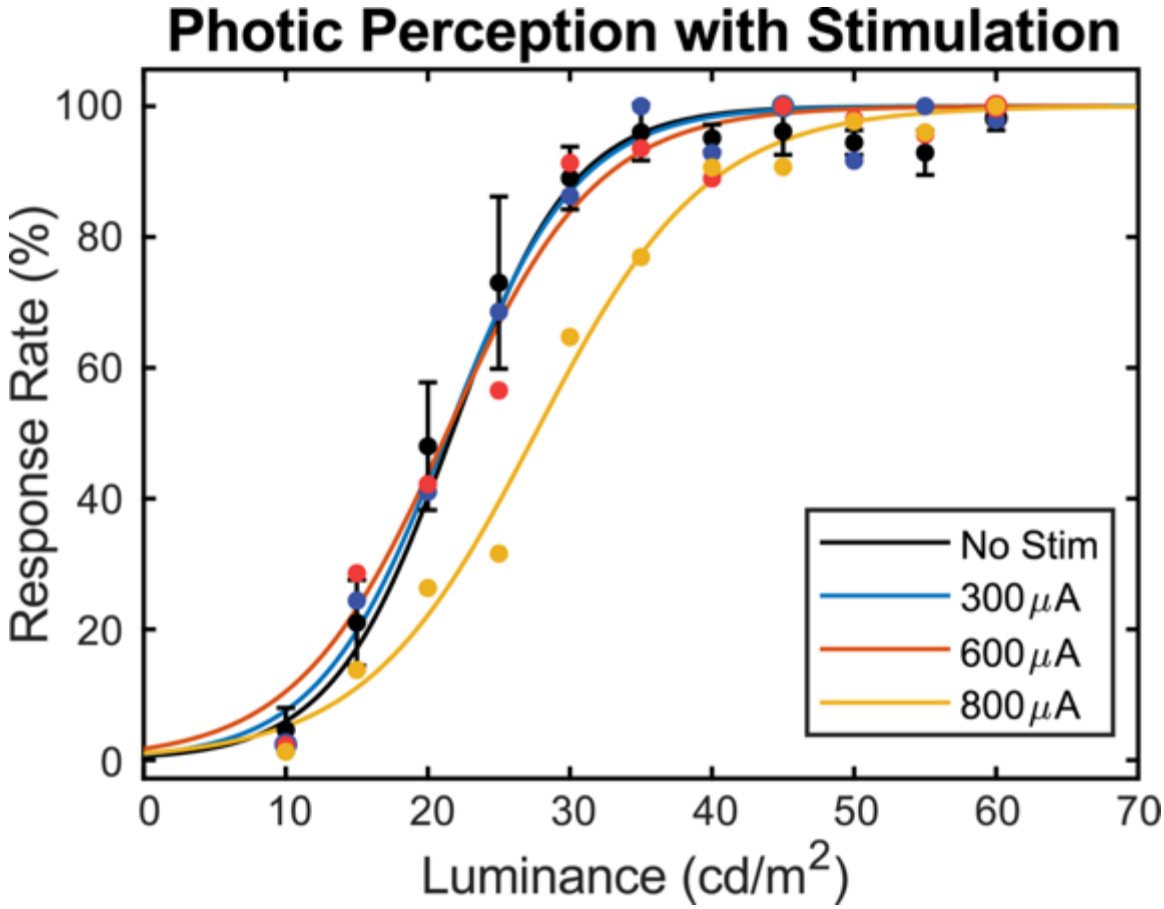

Figure 4.11. Photic psychophysics following termination of electric stimulation. The black cure indicates the baseline psychophysical responsiveness to photic stimuli at the indicated luminance values. The blue cure represents photic stimulation in the trial window following termination of stimulation applied at a peri-threshold current amplitude. The red curve indicates responsiveness to photic stimuli following stimulation at 2.5 times the amplitude of the threshold current. The yellow cure indicates photic responsiveness following application of an electric stimulus approximately three times the amplitude of the threshold current.

Acuity factors. NHP1 behavioral responses during the two-point discrimination task indicate consistent perception of separate visual percepts during simultaneous stimulation on separate electrodes. Responses to a control paradigm in which stimulation was applied on a single electrode (distance = 0mm) responded correctly, indicating a single visual sensation was perceived, in 89% of catch trials. Responses to concurrent stimulation on the closes neighboring electrodes, 2.08mm center-to-center distance, reported separate percepts observed in 90% of trials and indicated multiple percepts observed in 10% of trials. Larger distances between stimulating

sites continued to yield responses indicating separate percepts (Figure 4.12). The analysis consists of 31 electrode pairings and 5009 stimulation trials.

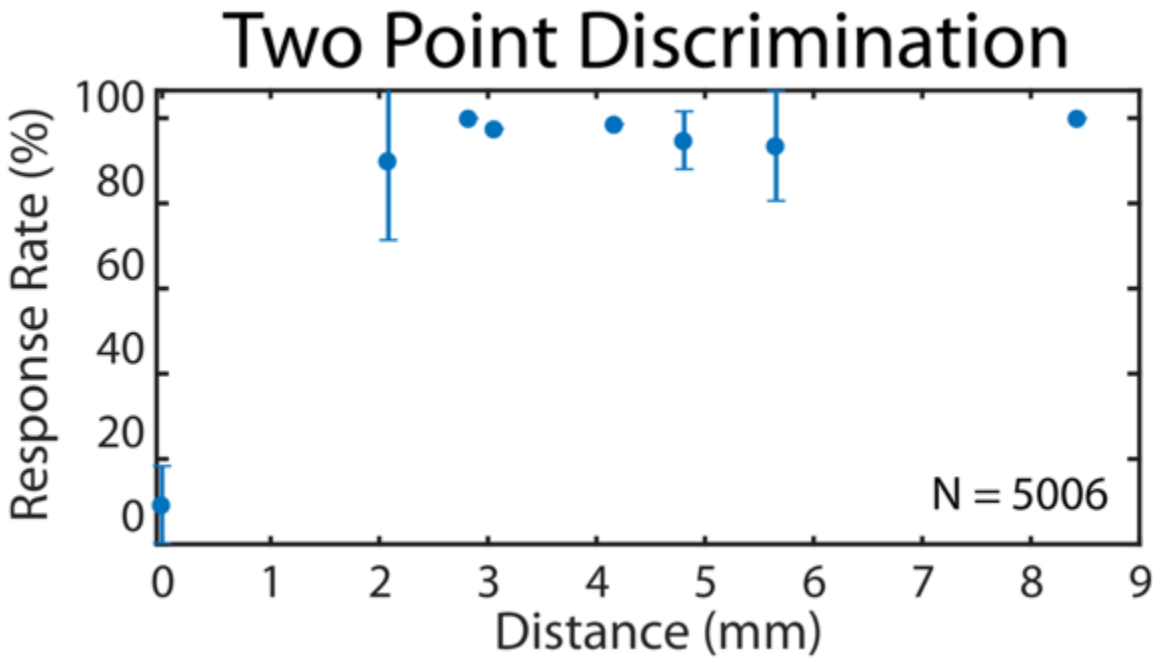

Figure 4.12. Two-point discrimination psychophysics. NHP1 behavioral responses to stimulating on electrodes at varying distances. Response rate reflects rate behavioral responses indicating perception of multiple stimuli. A distance of zero millimeters indicated stimulation at a single electrode site and was used as control. NHP1 behavioral responses to stimulation on two electrodes indicated perception of separate percepts at each distance tested. Nearest electrode pairs were separated by 2 mm, center-to-center.

DISCUSSION

ECMS was able to consistently evoke visual percepts in a NHP model. This constancy extended to implants over the same area of cortex and a combined implant time over a year. Thresholds were significantly lower than the several milliamperes required to evoke perceptual responses with large scale surface electrodes and counters the clam by Dobelle that electrode diameter does not have an impact on perception thresholds (Dobelle, Quest, Antunes, Roberts, & Girvin, 1979). This claim however, was validated only with electrodes over 1mm in diameter. Surface electrodes of this size are thought to operate on a different scale than submillimeter-diameter micro-electrodes (Cogan, 2008; Cogan, Ludwig, Welle, & Takmakov, 2016; Kellis et al.,

2016). Micro-electrodes have a significantly more localized interface with tissue. The charge necessary to effect change on a smaller volume of tissue is expected. The extent of how localized that volume is a notable factor for surface electrodes for main reasons, the first being whether it can sufficiently active enough tissue in layers deep enough to evoke perception, the second relating to neighboring stimulation cites and minimum perceptible difference. Previous studies were able to evoke visual percepts with electric stimulation in layer 1 of rhesus macaque striate cortex with 127µm wire electrodes (DeYoe, Lewine, & Doty, 2005) and this study consistently evoked percepts with surface stimulation on 200µm electrodes. With feasibility demonstrated, additional factors involved in consistency, safety, and resolution can be evaluated.

Stimulation thresholds across the array initially followed a general trend of increasing with eccentricity. This is not expected, considering the relationship between cortical area allocated per visual degree and eccentricity, in which more cortical area is allocated to visual field space located near the foveal representation. It can be assumed, provided the applied current is consistent, that the volume of tissue activated by surface stimulation is approximately the same regardless of spatial position. There is also a known positive relationship between applied current and volume of activation. Surface evoked percepts will intrinsically be larger in the periphery because the visual field representations are closer together. Combined with the noted increase in threshold, percepts size may increase at a more noticeable rate with eccentricity. However, a recent study applying epicortical stimulation on large ECoG electrodes in humans reported a saturation in phosphene size over a certain level of applied current (Bosking et al., 2017). Provided this phenomenon is consistent with microstimulation, size discrepancies may be less dramatic. More consistent percept size would be ideal to maintain consistency and limit image distortion when evoking complex imagery with stimulation.

This pattern, while clear with initial array thresholds, was not observed with the end-point threshold mapping. Thresholds for electrodes in more peripheral representations tended to decrease, while more foveal electrodes tended to maintain similar thresholds or slightly increase. As a result, thresholds across the array were generally more consistent. Initial percepts may have needed to be more notable in scale in the periphery for the subject to respond, compared to more

centrally located electrically evoked percepts. This may have been attention related as well as represent an adaptive learning effect. Previous studies in primates have shown decreases in response thresholds to visual cortex stimulation with prolonged training during forced-choice detection tasks(Ni & Maunsell, 2010). This would account for reductions in thresholds observed from implant 1 to implant 2, as well as longitudinally with electrodes on the second array.

For electrical stimulation-based prosthetics, there is already an imperative to maintain low stimulation thresholds to avoid stimulation-induced neurotoxicity; it also factors into the effective resolution of a finalized prosthetic device. Lower current amplitudes activate smaller volumes of cortex, allowing neighboring stimulation sites to be closer without interfering with each other. Higher thresholds translate to larger volumes of tissue being activated, increasing the minimum distance at which two neighboring electrodes can evoke distinct sensations. In this study, the subject consistently reported two distinct percepts from concurrent stimulation on electrodes with a center to center spacing of 2.01 mm. The absolute minimum distance for 200µm electrodes may be smaller and will be tested in following iterations with tighter inter-electrode spacing. This distance was evaluated with an applied current of 600µA supra-threshold for all electrodes and held true regardless of eccentricity. Differentiation will likely be influenced by this current, with greater perceived separability likely with lower applied currents.

The main advantage in targeting the primary visual cortex for visual prostheses is the cortical magnification factor (CMF), which relates a distance across a sheet of neurons, representing a given angle visual field space (Born, Trott, & Hartmann, 2015; Duncan & Boynton, 2003). The upper range of CMF for foveal representations in humans and nonhuman primates has been reported to 15-20 mm/deg, compared to a magnification factor of approximately 0.3 mm/deg in the retina (Brindley & Lewin, 1968; Cowey & Rolls, 1974; Dow, Snyder, Vautin, & Bauer, 1981; Duncan & Boynton, 2003; Tootell, Silverman, Switkes, & De Valois, 1982; Van Essen, Newsome, & Maunsell, 1984). For visual prosthetics, this translates to a higher resolution being attainable when targeting V1. The values for CMF provide some insight into what level of resolution or artificial acuity that may be attainable with the approach detailed in this study. The results obtained suggest

clearly separable percepts can be evoked at a distance of 2 mm, suggesting sub visual degree resolution is attainable with ECMS.

For a prosthetic device to be worth the risk of implantation requires it to provide therapeutic benefits consistently over time; minimizing tissue damage can increase the functional longevity of a device. Given the physics and placement of epicortical electrodes, ECMS inherently necessitates higher baseline thresholds and larger volumes of activation compared to ICMS. However, they potentially offer a more stable system with better long-term viability in vivo. Intracortical studies observed an increase in threshold after several months of implantation (Torab, et al., 2011; Davis, et al., 2012). Epicortical arrays may maintain more consistent thresholds over time since they evoke a comparatively minimal tissue response. Similar technologies, such epiretinal stimulation has shown considerable consistency for over five years (Humayun et al., 2013), and other implantable systems that employ long term subdural stimulation, such as the NeuroPace RMS System (NeuroPace, Mountain View, CA, USA) have also demonstrated therapeutic responsiveness to stimulation for over two years(Heck et al., 2014; Sun & Morrell, 2014). This study evaluated ECMS in NHP V1, showing consistent perception thresholds with two arrays and longitudinally across several months. Additionally, the array was safely explanted after seven months of implant, with a new array placed over the same area. This is not typically feasible with intracortical arrays due to the tissue dimpling caused by their placement and the general fragility that hinders explanation. With the epicortical approach detailed herein, response thresholds did not increase, nor was photic perception impaired. Provided this stability continues, an epicortical approach may provide a more consistent platform for a prosthetic system.

Comparing Shannon model values for charge per phase and charge density metrics of tissue damage across a range of stimulation methods used to evoke visual sensations have reported values in excess of the safety limit. Intracortical microsimulation studies initially reported values below the safety value. However, with threshold increases observed over 6 months of implant, thresholds rose to a level that exceeded safety limits [9, 10]. Two acute epicortical macro-stimulation studies [5, 38] both reported a range of threhsolds to evoke perception, with the maximum current threhsolds exceeding safety limits, and lower threhsolds mainiting a safe charge

per phase – charge density relationship. This study using epicortical microstimulation, in a similar fashion to previous studies, showed a range of threhsolds, the lower bounds falling below damage limits, and upper bounds above that limit. Charge relationships vaired in accordance with the pulse width used to evoke the sensation, with shorter pulse widths reducing the charge relaitonship below the damage limit. Implatible devices tend to use shorter pulse widths close to chronaxie. The Sannon metrics for threhsolds collected in the range of 0.1-0.3ms pulse widths were comfortably below the damage limit, and suggests under normal operation, a device based on epicortical microstimulaiton would be capable of evoking snesations in such a way to inject current below accpted damage levels.

A review of therapeutic electrical stimulation concluded damage thresholds for microelectrodes are more dependent on charge per phase rather than charge density as with macro electrodes, with pulse frequency also being an important factor(Cogan, Ludwig, Welle, & Takmakov, 2016). While strict safety limits have yet to be determined for microelectrodes, microelectrodes have been shown to safely provide current densities exceeding the 30μC/cm^2 level approved by the FDA (Cogan, 2008; Cogan et al., 2016; Kellis et al., 2016). This safety range was tested specifically for microelectrodes with GSA 0.0002-0.002mm, whereas the traditional Shannon model of damage was derived from electrodes with a GSA in the range of 1-50mm^2. Microelectrodes, particularly surface microelectrodes, like the ones used in this study, typically have GSAs 0.03-0.07mm^2 and occupy a space in-between these two metrics. As these electrodes do not fall into the GSA ranges for which the predictive damage models were established, specific testing of the acceptable charge density and charge per phase limits for these larger microelectrodes will likely be necessary.

The method for which thresholds were collected used a longer pulse phase duration of 0.6ms. At this phase duration, thresholds were close to the lower limit of rheobase. This long phase duration did ensure low current thresholds and showed stability in evoking percepts, however, the increased duration beyond chronaxie means that is less efficient in its usage of charge to evoke some sensation. As the Shannon metric for tissue damage is largely charge based, it should be

noted that thresholds collected with shorter phase duration did fall below the Shannon line with a k = 1.86, a commonly accepted damage limit (Cogan, 2008; Cogan et al., 2016).

Maximum charge density and charge per phase applied here were 1.1mC/cm^2 and 540nC/ph respectively, far above threshold values of 0.177-0.35mC/cm^2 and 87-172nC/ph. With this level of current injection, no functional deficits were detected. Histology has not been collected at the time of publication to directly determine tissue damage, however pre- and post-study responsiveness to photic stimuli used as a metric of visual function did not indicate acquired defects to natural perception nor lasting disruption of local visual processing. NHP1 did show an increase in responsiveness to lower luminance values, which is likely a training effect, rather than a sensitization caused by electrical stimulation of cortex.

This approach does not reach therapeutic stimulation levels below the present 30μC/cm^2 charge density limits often enforced by regulating agencies. While it offers improved stability, and operates at a biologically relevant scale, charge requirements to evoke perception would need special pre-market approval. Data available in public regulatory databases in the form of SSEDs for devices approved by the PMA process detail a collection of devices that received approval in excess of traditional Shannon model limits, as well as data suggesting a wider range of acceptable values (Kumsa et al., 2018). This study did not observe functional impairments or note changes in electrophysiology, suggesting the stimulation at the range applied here may be considered safe.

CHAPTER 5

CHARACTERIZING THE EFFECT OF STIMULATION PARAMETERS ON PERCEPTION THRESHOLDS AND CHARGE EFFICIENCY

ABSTRACT

The efficiency of charge utilized is central to the long-term functionality of implantable neural stimulating devices, impacting battery longevity, electrode degradation, and tissue health. Efficiency is dependent on temporal characteristics of the waveform stimulus, with pulse and pulse train parameters having an effect. This study attempts to characterize the effect of simple waveform parameters, phase asymmetry and pulse frequency, on charge efficiency at the functional level of evoking visual percepts. Current thresholds required to elicit a visual sensation were collected with phase durations of 0.1 – 0.6 ms, frequencies of 50 – 300 Hz, and leading-to-following phase ratios of 1:4. Results indicated that for a given pulse width, higher pulse frequency improves charge efficiency for charge balanced waveforms. The introduction of phase asymmetry also improved charge efficiency. Determining the ways in which waveform parameters mediate charge efficiency can assist in establishing optimal operating ranges for stimulating neural prosthetics to improve overall device functionality and long-term viability.

INTRODUCTION

The past few decades have seen a growing rise in the use of implantable neurostimulators for treating a range of disorders. Recent advances have employed targeted electrical stimulation of the nervous system as a means to artificially create sensation lost to disease, injury, or amputation. With the expanding filed of implantable neurostimulators, and research in the field of sensory neural prosthetic devices progressing towards fully implantable systems, there is an increasing imperative to consider the impact of the stimulus parameters utilized.

The amount of and way in which charge is injected has implications for tissue damage (S. Cogan, 2008; S. Cogan, Ludwig, Welle, & Takmakov, 2016) and the qualities of the sensation evoked (Graczyk et al., 2016; L. A. Johnson et al., 2013; Lee et al., 2018; Romo, Hernandez,

Zainos, & Salinas, 1998). Furthermore, internalized systems rely on battery power for operation. The size of the battery is directly proportional to the maximum power that can be delivered per stimulus pulse and the lifetime of the battery related to the energy consumed per stimulus pulse (Wongsarnpigoon, Woock, & Grill, 2010).

Tissue damage factors. There is a relationship between the amount of current injected and the extent of tissue damage incurred (Merrill, Bikson, & Jefferys, 2005). Traditional metrics of damage thresholds for electrical stimulation of nervous tissue focus on the charge density and charge per phase of an applied pulse. The Shannon equation can be used to describe the boundary between tissue damaging and non-damaging levels with a linear relationship between charge density and charge per phase(S. Cogan et al., 2016). This is given by:

$$\log\left(\frac{Q}{A}\right) = k - \log(Q) \qquad 5.1$$

where Q is charge per phase (μC) and Q/A is the charge density per phase (μC/cm^2)(Merrill et al., 2005). This relationship was determined through experimentation with large scale surface electrodes (GSA of .01cm^2 – .5cm^2) and predicts damage threshold well for macroelectrodes. Although a factor to consider, there are limitations of this predictive model and its applicability to stimulation with micro-scale electrodes, an interface type common to sensory encoding applications. Current density thresholds for damage have been shown to scale differently with microelectrodes (GSA<.01cm^2), whereby the charge per phase is a stronger predictor of damage (S. Cogan et al., 2016). Optimizing charge efficiency with stimulus pulse parameters will reduce the total amount of charge necessary to evoke perception and contribute to maintaining healthy, viable tissue.

Stimulation efficiency. Stimulation efficiency is dependent on waveforms shape and pulse train characteristics. The strength-duration relationship described by Weiss (WEISS & Weiss, 1901) and Lapicque (Lapicque, 1907) is described mathematically by:

$$I_{th} = \frac{I_{rh}}{1-e^{-W/\tau_m}} \qquad 5.2$$

where I_{th} is the threshold current, I_{rh} is the rheobase current, W is the pulse width, and τ_m is the membrane time constant (Merrill et al., 2005). The minimum constant current able to evoke

excitation at a theoretically infinite pulse width is the rheobase current, chronaxie is the time duration at twice rheobase current. The strength-duration relationship instructs that shorter pulse widths yield greater charge efficiency, longer pulse widths increase power efficiency, and optimized efficiency is achieved with a pulse duration set to chronaxie (Kroll, 1993) (Wongsarnpigoon et al., 2010). Computational models have shown strength duration curves produced with different waveforms shapes have distinct behavior (Sahin & Tie, 2007), indicating waveform shape has non-trivial impact on stimulation efficiency.

Tissue damage and efficiency can be mediated by pulse waveform and pulse train characteristics, and range of arbitrary waveform shapes have been proposed to optimize outcomes. However, even within the family of rectangular waveforms, room for optimization exists. Monophasic waveforms readily activate excitable tissue but are known to cause more tissue damage, and are in limited use in neurostimulators, particularly in sensory prosthetic applications. Biphasic stimulation, which uses an activating phase followed by a reversal phase to remove the charge from tissue, is commonly used and is known to reduce tissue damage in comparison to monophasic stimulation despite the higher amplitudes to activate tissue. Biphasic waveforms are typically charge balanced, which means the product of the amplitude and the phase duration for the reversal phase is equal to that of the activating phase. The result is reduced tissue damage, compared to a monophasic waveform, and improved excitation capacity compared to charge balanced biphasic waveforms (Merrill et al., 2005). Asymmetric waveform maintains charge balance by reducing the amplitude and increasing the pulse duration of the reversal phase of stimulation. The effect is rapid charge injection followed by a slower removal of charge. It has been suggested that asymmetric waveforms can improve performance (S. F. Cogan, Troyk, Ehrlich, Plante, & Detlefsen, 2006), but it has not yet been established how introducing asymmetry effects thresholds and charge efficiency. This study seeks to characterize the relationship between phase asymmetry and charge efficiency.

Pulse frequency also factors into charge accumulation (Merrill et al., 2005) and may have an impact on charge efficiency. Pulse trains with sufficiently short inter-pulse durations can result in electrical charge accumulating on the electrodes. Monophasic cathodal pulsing yields a negative

drift in potential if a second pulse occurs before the electrode has completely discharged from the previous pulse. During charge balanced, cathodal first stimulation is subject to effects from the anodal current and the double layer capacitance, resulting in a positive drift in potential. These drifts in potential can contribute to both tissue and electrode damage (Merrill et al., 2005). There is considerably less understood about the effect pulse frequency has on the sensory perception of electrical stimulation. Preliminary studies in which electrical stimulation has been applied to somatosensory cortex imply pulse frequency may correlate to the perceived intensity of a stimulus(L. Johnson et al., 2013). Pulse frequency and its effect on charge efficiency have yet to be evaluated, despite its impact on a devices efficacy and longevity. This study hypothesizes that stimulation frequency and waveform shape can be tuned to improve charge efficiency

METHODS

Subjects and surgery. One adult male rhesus macaques (Macaca Mulatta) will be used in this study, NHP1. NHP1 was implanted with the epicortical array described above. The array was placed in the sagittal fissure facing the right hemisphere, with the caudal-most point of the array placed in close approximation to the pole, superior to the calcarine fissure. Human protocols were followed during surgery and post-operative care.

Recording and stimulation. Recordings were conducted with a 128-channel Neural Signal processor (Blackrock Micro Systems). Stimulation experiments use an IZ2-128 stimulator (Tucker-Davis Technologies, Alachua, FL). The stimulator is capable of delivering 300μA to 128 channels. To achieve higher current levels, up to 3mA, a custom adder box was developed. Pulse trains consisted of symmetric, cathode-first, biphasic waveforms. The initial interphase interval and phase duration are set at 100μs and 600μs respectively, with pulse frequency and train duration set at 300Hz and 300ms. Explanations of waveform parameters are presented in Figure 5.1.

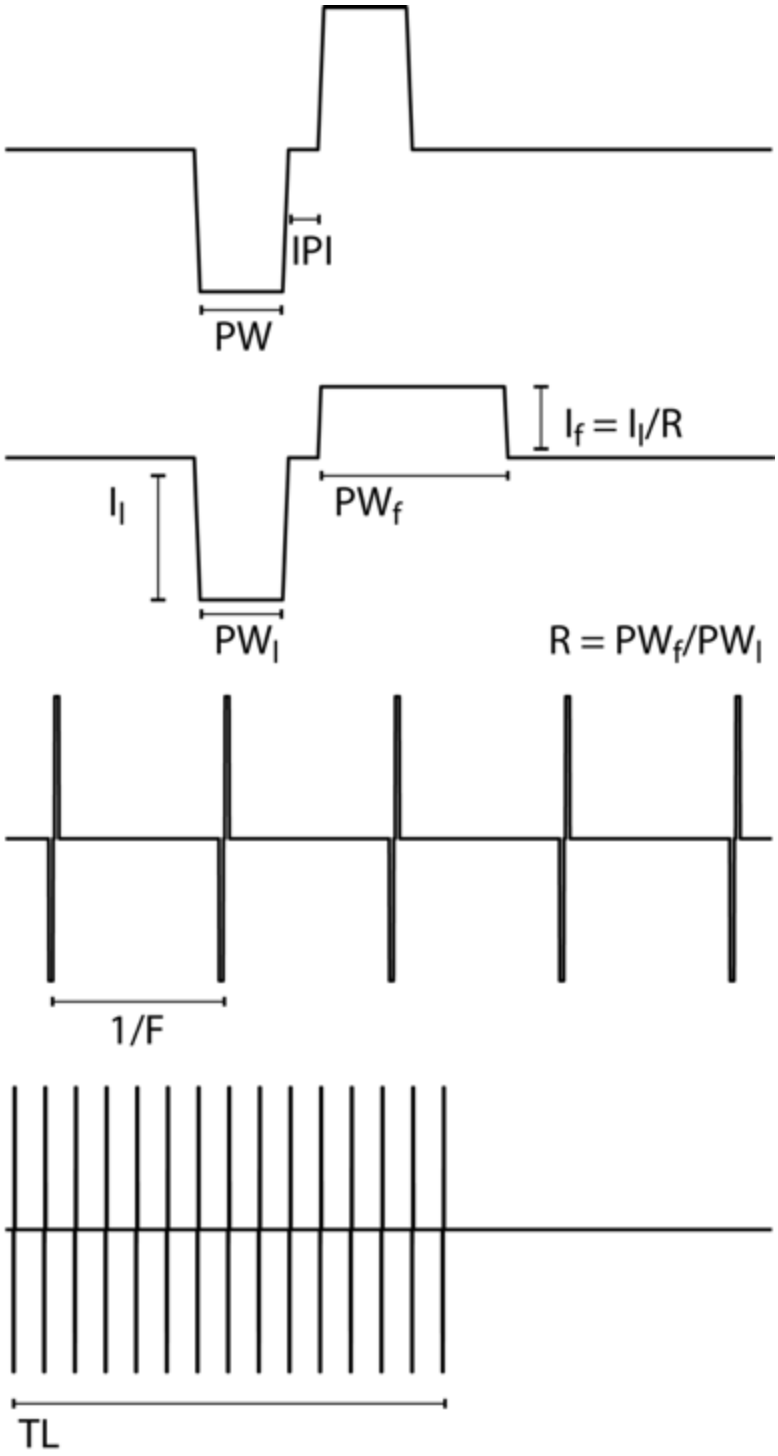

Figure 5.1. Waveform parameter graphical explanations. The top most plot shows one symmetric, biphasic waveform, indicating the pulse width PW and the interphase interval IPI. The second plot shows an asymmetric charge-balanced waveform, indicating the pulse widths and amplitudes for leading and following phases, and the mathematical relationship between each parameter and the selected ratio R. The third plot shows pulse frequency F, defined by the inverse of the interval between each pulse. The lowest plot depicts a pulse train, with the train length TL indicated.

Stimulation paradigms.

Frequency variation. Thresholds were collected with a constant train length of 300 ms and each phase duration listed in the strength-duration curve methods section for pulse frequencies of 50, 100, 150, 200, and 300Hz. Thresholds and minimum charge for each were determined and compared across frequencies. The resulting dataset was also used to evaluate the interdepended relationship between waveform parameters and charge injected in a pulse phase and for the duration of the pulse train. Charge per phase Q_{ph} is calculated according to Equation 5.3, and pulse train charge Q_{PT} in Equation 5.4.

$$Q_{ph} = I * PW \tag{5.3}$$

$$Q_{PT} = I * PW * F * TL \tag{5.4}$$

where I is the current amplitude, PW is the pulse width, F is the pulse frequency, and TL is the duration of the train length.

Charge balanced frequency variation. In order to account for the differences in total charge injected during a pulse train that occur with frequency, an additional set of thresholds was collected whereby charge was balanced across the pulse train by modulating the train length. The length of the delivered pulse train was set to the time duration allowing for fifteen pulses at each frequency. The values for the frequencies 50, 100, 150, 200, and 300Hz are 300, 150, 100, 75, and 50ms respectively. All thresholds were collected with a phase duration of 0.6 ms and each again for 0.3 ms.

Asymmetry ratio. The asymmetric ratio *r* is described by the proportion of the phase duration of the leading or activating phase PW_l to the reversal phase PW_f. For the charge-balanced asymmetric waveforms, the phase duration of the reversal phase was directly proportional to the ratio and the current amplitude I_x was inversely proportional.

$$PW_l = rPW_f \tag{5.6}$$

$$I_f = \frac{I_l}{r} \tag{5.7}$$

Individual pulse waveforms for ratios of 1:1, 1:2, 1:3, and 1:4 were tested, each at a pulse frequency of 200Hz and train length of 300ms.

Strength-duration and charge-duration curves. Thresholds were collected for phase durations of 0.1, 0.3, 0.4, and 0.6 ms for each paradigm outlined. Thresholds from these four points were curve fit to Equation 5.3:

$$I_{th} = \frac{I_{rh}}{1-e^{-W/\tau_m}} \tag{5.8}$$

where I_{th} is the threshold current, I_{rh} is the rheobase current, W is the pulse width, and τ_m is the membrane time constant. In order to curve fit, the rheobase current for a given parameter regime was set to the threshold value determined with a phase duration of 0.6ms. The time constant was used to additionally tune the equation. The charge per phase threshold Q_{th} was determined by the product of the current threshold and the pulse width, such that:

$$Q_{th} = I_{th}W \tag{5.9}$$

The minimum charge Q_{min} was determined by the threshold charge at chronaxie.

Threshold detection task. This task is used to determine the luminance threshold for detection of photic stimuli as well as current thresholds for perception of electric stimuli. The NHP is placed in a primate chair inside of a dark chamber, facing a CRT monitor (Figure 5.2). The subject is required to place each hand on a capacitance switch, one to the left and the other to the right. A small red dot (.1X.1 visual degrees) at the center of the CRT screen was used for a fixation point. Once the NHP directs its gaze within one degree of the center point, an auditory tone signals the start of the trial. The NHP must maintain eye fixation for 200ms before a stimulus, either photic or electric, is presented. Electric stimuli are described below. Photic stimuli were randomly varied within a list of monochromatic shapes (Gaussian, square, bar, and donut) with randomly varying size and orientation angle parameters to encourage generalization responsiveness to visual sensations. Luminance levels are varied between 10 and 60 cd/m^2 in 5 cd/m^2 increments and presented on a screen with background luminance of 10 cd/m^2. Photic stimuli are presented for

300ms. Following a variable hold duration, a second unique auditory tone cues the NHP to respond. The NHP responds by removing its right hand to indicate that it did not perceive, or its left hand to indicate that it did perceive a stimulus. Photic threshold trials are rewarded with a bolus of water 50% of the time regardless of response. Clearly visible or invisible catch photic trials are used to ensure that the animal is responding correctly; rewarded is given only if the correct response is made. Catch stimuli are presented in 30% of trials. LabView (National Instruments, Austin, TX) is used to control task flow and monitor session progress. Visual stimuli are generated using a real-time visual stimulator (ViSaGe, Cambridge Research Systems, Rochester, Kent, England) and displayed on a CRT monitor (G90fb, ViewSonic, Walnut, CA). The NHPs are head-fixed using a minimally invasive technique and eye positions is tracked with an infrared camera (EyeLink 1000, SR Research, Mississauga, ON, Canada). Behavioral and neural data are collected using a Cerebus NeuroPort System (Blackrock Microsystems, Salt Lake City, UT, USA) at 10kHz. Data collection is conducted daily in 2 hour sessions.

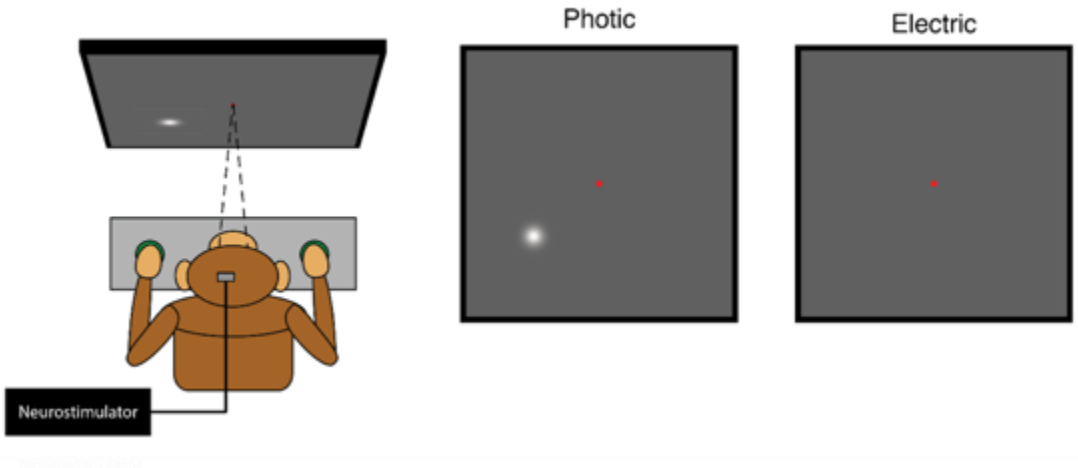

Figure 5.2. Task setup for all experiments. Non-human primate subjects are seated, head-fixed, facing a CRT monitor. Photic stimuli are present on monitor. Electric stimuli are delivered via an IZ2 neurostimulator with no photic stimuli presented on monitor, fixation point is maintained.

Grid design. An epicortical array featuring concentric rings was designed and produced in tandem with Second Sight Medical Products (Sylmar, CA 91342, USA). The array consists of 46 electrodes. The center electrode for each grouping has an exposed area of 200μm. Each concentric ring is composed of these 200μm electrode pads electrically tied together. The concentric rings are

composed of 6, 12, or 18 electrode pads, creating effective diameters of 750μm, 1500μm, and 2100μm. The array has a length of 13.84 mm and height of 9 mm. Groupings have a spacing of 2.12mm from ring center to center. Four rings with increasing eccentricity across the midline of the array contain each of the four electrode diameters; all remaining groupings contain the center electrode, the 6-ring, and the 12-ring (Figure 5.3). The array was potted to a titanium base with ZIF clip connector. The pedestal base is used as ground.

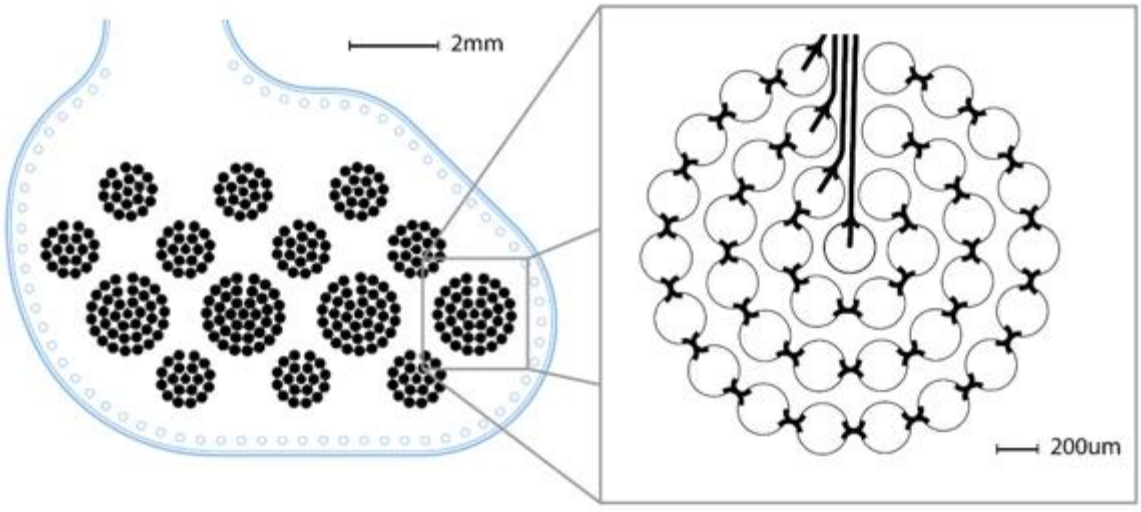

Figure 5.3. Custom array design with concentric rings. Array allows for probing thresholds and percept characteristics while accounting for variations with eccentricity and maximizing spatial landscape of the array. Rings made up of 1-, 6-, 12-, 18-disk groupings and provide electrode diameters of 200, 800 1400 and 2000μm.

Determining electric thresholds. Electric stimuli were applied at 100μA increments from 0-900μA and consisted of 5-40% of trials within a daily session, the reminder consisting of photic trials. At least one photic trial separated each electric trial to limit the effect of prior stimulations on the raw threshold collection. The amplitude of the current was applied randomly between the specified values. For each session, responses to stimulation were fitted with a sigmoid curve, with the threshold determined to be the point at which the fitted curve passed 80%.

Data collection. Data was collected daily in sessions lasting up 3.5 hours. Sessions including electric stimulation were conducted most days, with gaps occurring for collection of receptive field data and photic behavioral data baselines.

RESULTS

Pulse frequency and charge efficiency.

Perception thresholds. The current amplitude necessary to evoke behavioral responses indicating perception decreased with increasing frequency. Within each phase duration grouping examined, threshold values decreased as pulse frequency was increased. Values for charge per phase at threshold levels of charge injection also decreased with frequency across all pulse widths assessed. The total charge delivered at threshold across the full pulse train increased with pulse frequency (Figure 5.4).

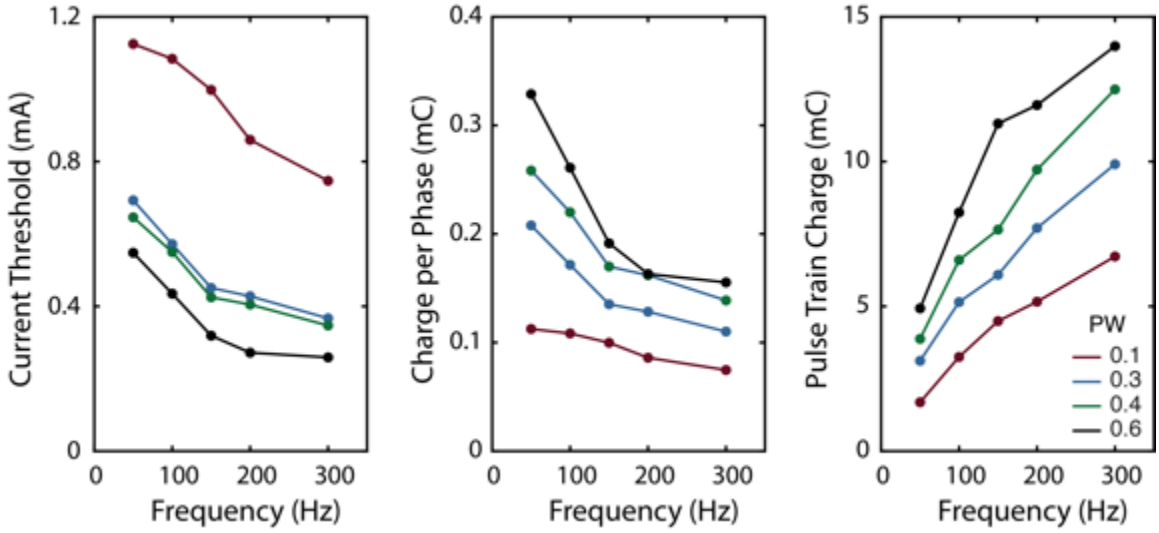

Figure 5.4. Threshold variations with pulse frequency. The left most plot indicates raw perception threshold values collected for each frequency (50Hz, 100Hz, 150Hz, 200Hz, and 300Hz) and each phase duration, 0.1 ms in purple, 0.3 ms in blue, 0.4 ms in green, and 0.6 ms represented in yellow. Threshold values decrease with frequency. Middle plot charge per phase as a function of pulse frequency. Charge per phase also was shown to decrease with increasing frequency. The right most plot shows the total chare delivered within a pulse train for threshold levels. Pulse train charge increases with frequency.

Strength-duration and charge-duration relationships with pulse frequency. Strength-duration and charge-duration curves were determined based on perception thresholds for each phase duration and pulse frequency combination. Strength- and charge-duration curves modulated in accordance with pulse frequency of the applied pulse train. Increasing pulse frequency consistently caused each curve to shift downward, indicating improved charge efficiency with

increasing frequency. (Figure 5.5). Minimum charge was used as a metric of charge efficiency; chronaxie was determined from the strength-duration curves and used to establish the minimum amount of charge for each pulse frequency. Results report minimum charge to decrease with pulse frequency (Figure 5.5).

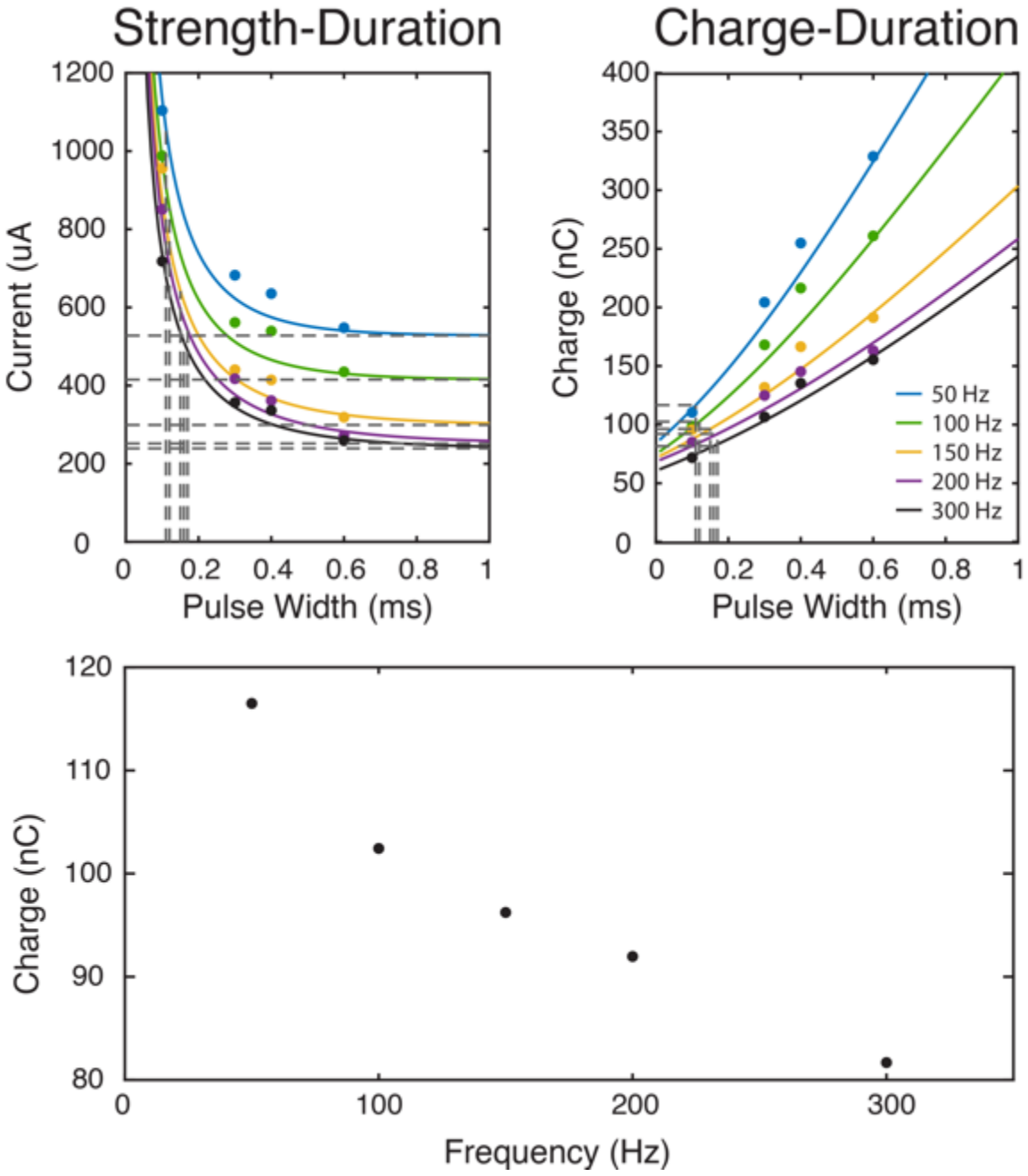

Figure 5.5. Strength-duration and charge-duration curves for tested pulse frequencies. The top row of the figure presents strength-duration (left) and charge-duration (right) relationships for different pulse frequencies. Increasing frequency consistently causes a vertical shift for both strength and charge duration relationships. The lower plot presents charge at chronaxie, or the minimum phase charge to evoke perception at each pulse frequency. Minimum charge decreased with frequency.

Assessing parameter relationships under equalized pulse train charge. From the collection of parameter-varied thresholds assessed, selections with equal total charge delivered across a pulse train were assessed to ascertain effects of phase duration and pulse frequency. Evaluating thresholds in response to frequency and phase duration when equal charge is delivered in the pulse train can provide insight into the relationship between waveforms characteristics and charge requirements. In the condition where frequency and phase duration are modulated to deliver equal charge, but train duration is fixed to 300 ms, the total charge delivered within a pulse train at threshold is less perturbed by frequency or phase duration, with vertical shifts largely dependent on the product of the phase duration and pulse frequency (Figure 5.6).

Current thresholds for a given pulse train charge tended to remain fairly consistent across frequency and pulse width variations. Pulse train cases with a lower total charge tended to show an increase with frequency and decrease with pulse width for threshold values. This was true for pulse trains with a base multiplier of 4.5, 6, and 9 for both frequency and pulse width. Trends dispersed for cases with a base multiplier of 18 or higher, with multipliers 18, 27, and 36 reflecting little to no variation in threshold across frequency or pulse width. Charge per phase did show a general trend across all levels of total pulse train charge evaluated in which charge per phase declined with frequency and increased with pulse width. in terms of total charge delivered, pulse train charge remained fairly consistent at threshold across frequency and pulse width. Selections with lower overall train charge, mainly those with multipliers of 4.5 and 6, did reflect an increase in pulse train charge with frequency to evoke perception, and decrease for pulse width (Figure 5.6).

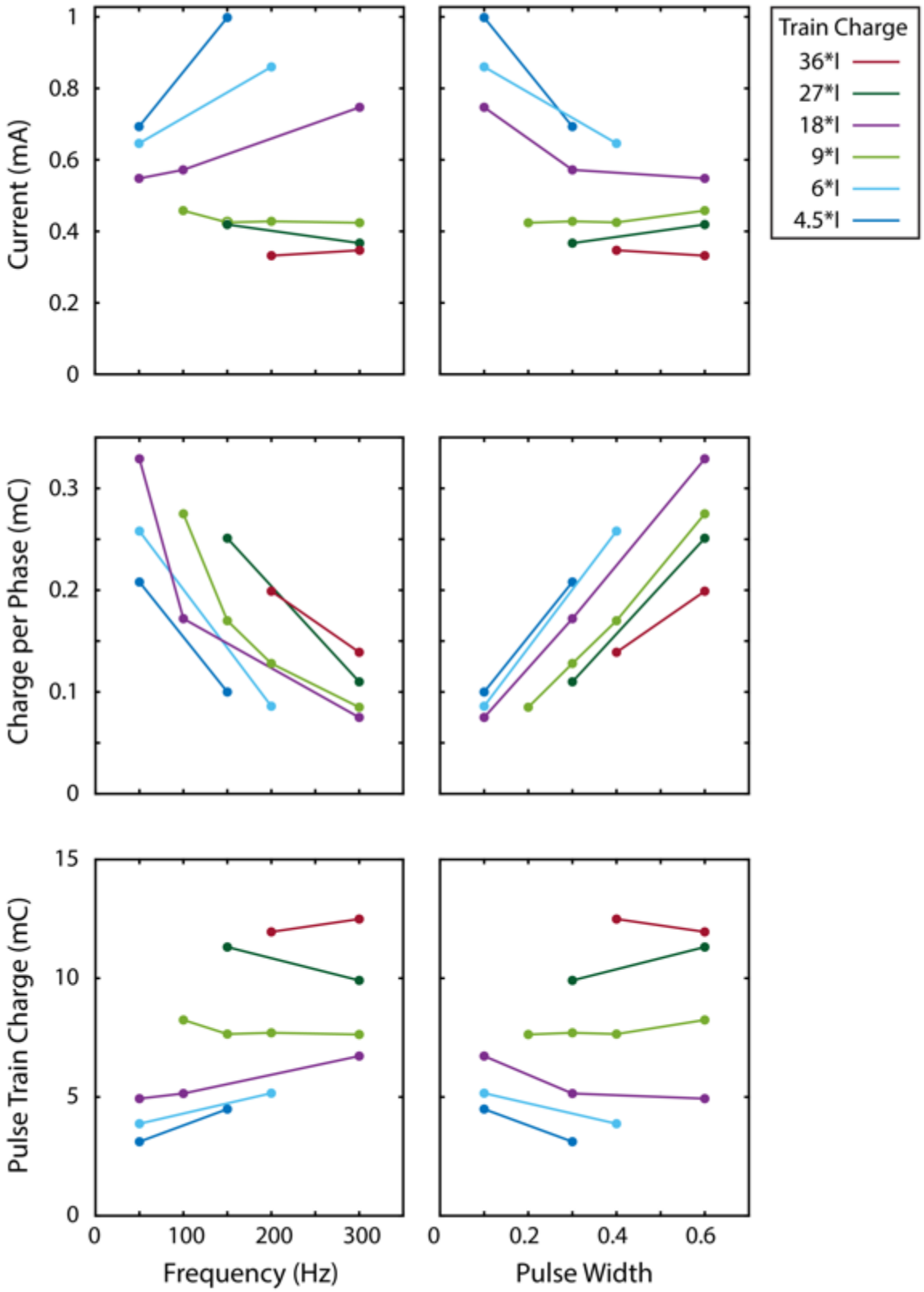

Figure 5.6. Parameter-charge relationships for equalized train charge. The left column change in indicated threshold metrics with pulse frequency, the column on the right presents values for pulse

width. The top row provides values of current threshold organized by train charge. The middle row reports the dependence of charge per phase on pulse frequency (left) and pulse width (right) when train charge is equalized. The bottom row reports the total pulse train charge delivered at threshold, and the variability with pulse frequency and pulse width.

***Charge injection equalized for pulse frequency across pulse train*.** To account for the increased charge delivered at higher pulse frequencies across the duration of the pulse train, perception thresholds were collected for one subset of phase durations (0.3 and 0.6ms) across the listed range of pulse frequencies with train length modulated to deliver equal charge for each pulse frequency. Charge balanced stimulation trains report improved charge efficacy with frequency when charge balancing is achieved through modulating train duration rather than the phase duration-frequency product. The total charge delivered across the pulse train inverts once charge balancing is considered. At threshold, charge per phase for reduced train lengths remains close in value to those collected at longer train lengths. Equalizing charge across the stimulus delivered reveals charge reductions with increasing frequency, mirroring the noted behavior for charge per phase, as it is mathematically proportional at an equal rate for each trial case. This does not account for equal charge delivered within a pulse train. Current thresholds did increase slightly for both phase durations evaluated from the non-train balanced condition to the fully charge balanced condition. Threshold increases were observed for each pulse width parameter across the range of evaluated frequencies. Charge per phase remained low and at similar values as in the unbalanced condition. Pulse train charge required to evoke perception decreased notably from the non-balanced condition to the charge balanced condition. Pulse train charge is uniformly proportional to charge per phase in this paradigm.

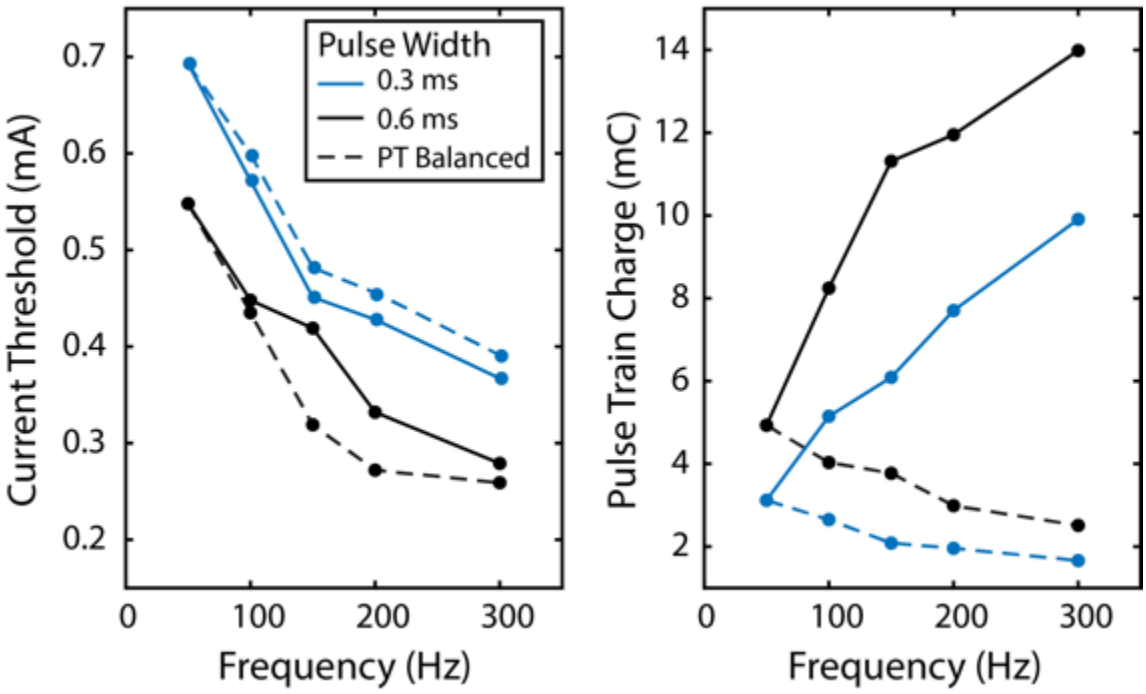

Figure 5.7. Charge balanced, frequency isolated effect on current thresholds and pulse train charge. Left shows current thresholds for pulse widths of 0.3 and 0.6 ms across increasing frequencies, for which train lengths have been modulated to deliver equal charge at each frequency point. Current thresholds deviated slightly from non-train balanced values. Right plot indicates total pulse train charge at threshold levels for unbalanced (solid line) and pulse train charge balanced (dashed line) for each pulse width evaluated. Pulse train charge was observed to decrease with frequency in the balanced condition, varying from the prior increase.

Asymmetric ratio and charge efficiency.

Perception thresholds. Phase asymmetry was evaluated in its capacity to improve charge efficiency. Current thresholds to evoke perception were found to decrease with increasing asymmetric ratio (Figure 5.8). Current threshold decreased for each pulse width evaluated with an increasing ratio. Pulse train charge was also observed to decrease with the asymmetric ratio for each pulse width condition evaluated. The shift from 1:1 to 1:2, that this the intial introduction of asymmetry had the largest impact or reduction in threshold for both 0.1 and 0.6 ms pulse widths. Intermediate pulse widths of 0.3 and 0.4 ms both reflected a more linear reduction in current threshold and pulse train charge in comparison to the other two pulse width conditions.

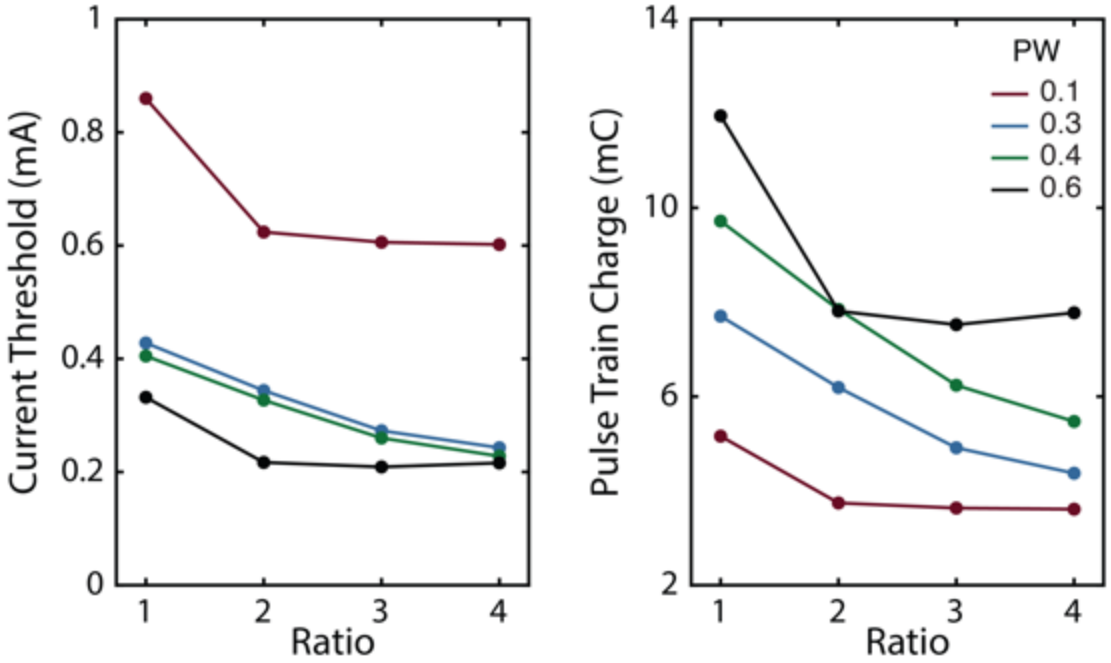

Figure 5.8. Perception thresholds varying by asymmetric pulse train ratio. Threshold variations with phase asymmetry. Top left indicates raw perception threshold values collected for each asymmetric ratio (1:1, 1:2, 1:3, 1:4) and each phase duration. Threshold values decrease as the ratio increases. Top right shows threshold values normalized to the 1:1 threshold for that phase duration, indicating a larger percent reduction in threshold between 1:1 and 1:2.

Charge relationships to asymmetric phase ratio. Strength-duration and charge-duration curves were determined based on perception thresholds for each phase duration and pulse ratio combination. Strength- and charge-duration curves modulated in accordance with the activating to reversal phase ratio of the applied pulse train (Figure 5.9). The effect on each of the duration relationships was less pronounced and sustained than the that observed by pulse frequency. The initial shift in curves from 1 to 1 was the largest, with remaining curves reflecting smaller downward shifts. The minimum charge metric of efficiency was shown to decrease rapidly from 1 to 2, with more gradual reductions in the range between 2 to 4. The introduction of phase asymmetry reflected an improvement in charge efficiency.

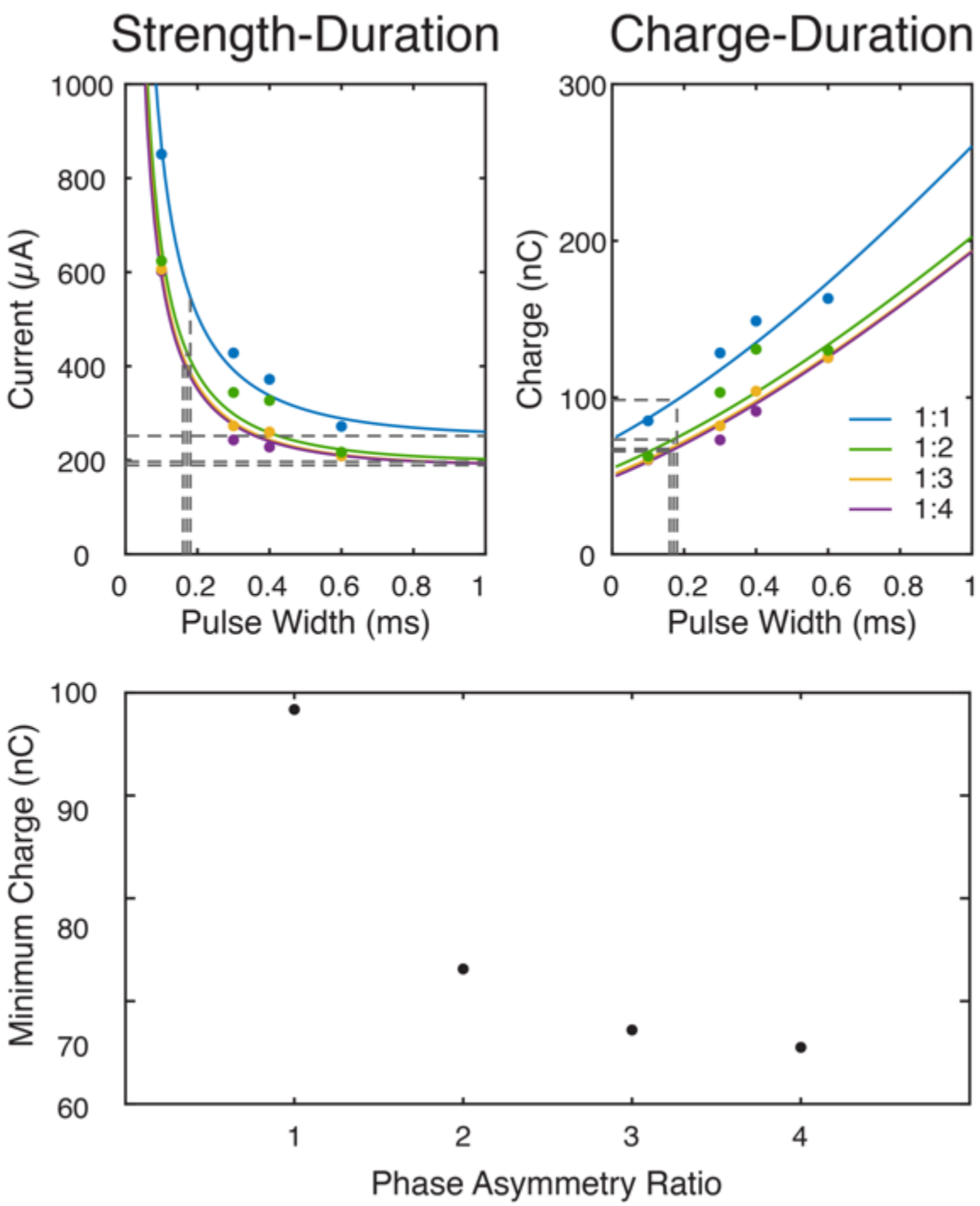

Figure 5.9. Strength-duration and charge-duration curves for asymmetric pulse waveforms. Strength-duration and charge-duration curves for tested asymmetric phase ratios. Strength- and charge-duration curves for each pulse ratio based on perception thresholds at each phase duration and frequency. Curves tended to shift downward with increasing ratios, indicating better charge efficiency at higher asymmetric ratios.

Stimulation parameters and safety considerations. The Shannon model is the generally accepted metric for determining whether a stimulation regime is thought to cause damage, with a damage threshold of k = 1.86. Increasing pulse frequency resulted in a reduction of k value across each set of pulse widths. Changing pulse frequency from 50 Hz to 300Hz reduced the k value from 1.58 to 1.21, 2.13 to 1.58, 2.32 to 1.78, and 2.53 to 1.88 for pulse width of 0.1, 0.3, 0.4, and 0.6 ms pulse widths respectively. Implementing asymmetric pulses was also observed to reduce the Shannon k value. At a pulse frequency of 200 Hz, each pulse width tested fell below the safety threshold of k = 1.86 for asymmetric ratios greater or equal to 2. The reductions observed form symmetric (ratio = 1) to the maximum asymmetry tested (ratio = 4) were 1.37 to 1.06, 1.72 to 1.22, 1.92 to 1.42, and 1.92 to 1.69 for pulse widths of 0.1, 0.3, 0.4 and 0.6 respectively.

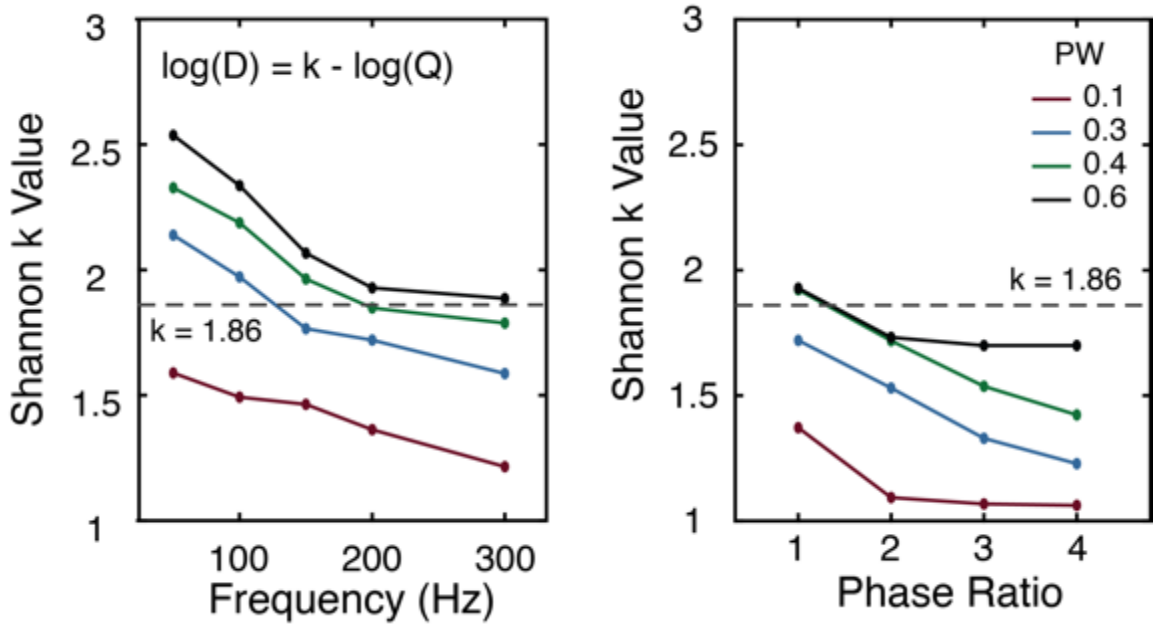

Figure 5.10. Tissue damage metrics for varied waveform parameters. Left shows the change in Shannon k value for different pulse frequencies at each pulse width evaluated. Higher frequencies are observed to reduce the k value. The accepted damage threshold of k = 1.86 is indicated by the horizontal dashed line. Right presents the change in Shannon k value for a asymmetric phase ratios from 1 to 4, applied at 200 Hz, for each evaluated pulse width. Introducing phase asymmetry reduces the Shannon k value below the damage threshold for each pulse width at asymmetric ratios 2 and greater.

DISCUSSION

This study sought to evaluate the way in which modulating pulse train and waveform parameters impacts perception threshold and charge efficiency. Pulse frequency and phase asymmetry were each shown to influence the current required to evoke a visual percept and shift the relationship between phase duration and charge. Previous studies (Fridman, Blair, Blaisdell, & Judy, 2010; L. Johnson et al., 2013) have proposed phase duration and pulse frequency as cofactors in evoking perception, with both linked to the intensity of the percept. The results here support the interdependence. Modulating both frequency and pulse width to inject equal charge across a waveform resulted in similar thresholds and charge requirements to evoke perceptions. This study also observed that when frequency was isolated and pulse width maintained constant, charge efficiency was improved with frequency; the current thresholds to evoke perception decreased with increasing frequency. These results are not seen as incongruous as it is understood that charge efficiency is maximized at chronaxie and decreases with increasing pulse width. Therefore, increasing pulse width and decreasing frequency to maintain charge balance will likely cancel out the opposing effects on efficiency and reveal a direct dependence on total charge delivered. While the total charge injected within a pulse train is undoubtedly important in eliciting a sensation, the way in which charge is applied does impact its efficiency and likely modulates the quality of the evoked sensation. Frequency, amplitude, and pulse width have each been reported to modulate the intensity of an evoked percept. Implantable devices used in sensory prosthetic applications may be able to operate at higher frequencies and lower amplitudes in order to achieve the desired percept intensity and maintain optimal charge efficiency.

Provided the initial metrics in collecting strength duration curves did not account for full chare delivered across the pulse train, the effect of frequency on efficiency was likely exaggerated due to the increase in delivered charge. However, in conditions where pulse train charge is held constant and only frequency is varied, the reduction in phase charge remained as well as a total reduction in pulse train charge requirements. The effect indicates the rate of charge delivered has a clear impact, and not just the integrated amount of charge delivered. Furthermore, introducing pulse asymmetry was also observed to improved charge efficiency. This does not fundamentally

change the way charge is delivered, but does how long it interacts with tissue and the rate at which it is reveres. Provided the rate of charge delivered effects charge efficiency and perception, manipulating the rate of charge reversal may also impact the way the charge is observed or the way in which the tissue responds to it. It has not yet been studied how asymmetric pulses effect the quality of an evoked sensation. Provided asymmetry has little effect on the qualities of the percept experienced, charge-balanced asymmetric pulses would provide a means to additionally improve charge efficiency without disrupting the evoked sensation. If asymmetry does in some way impact the qualities or subjective experience of the percept, that parameter could then be used as a means to increase the complexity of the generated percept or scene.

Modulating individual pulse parameters as well as pulse train parameters were observed to effect whether a stimulation regime was considered to cause tissue damage. Increasing pulse frequency as well as introducing phase asymmetry both reduced the k value, a metric associated with damaging stimulation. Given that maintaining tissue health is important for the long-term viability of a prosthetic device, employing stimulation parameters that reduce the damage effects of stimulation is an imperative. Careful control of the waveform shape used to deliver charge can improve efficiency, and the interplay between individual parameters should be considered when developing stimulation paradigms for implantable devices. Increasing frequency and introducing phase asymmetry improve efficiency, shifting pulse width away from chronaxie reduces efficiency. Future studies are needed to further explore the relationship between waveform parameters and the subjective experience or qualities of the evoked percept in order to establish optimal ranges for device functionality.

REFERENCES

Ashmont, K. (2015). Engineering Approaches for Improving Cortical Interfacing and Algorithms for the Evaluation of Treatment Resistant Epilepsy. *Doctoral DIssertation*.

Ayton, L. (2014). First-in-Human Trial of a Novel Suprachoroidal Retinal Prosthesis. *PLoS On, 9*(12).

Barrese, J., Rao, N., Paroo, K., Triebwasser, C., Vargas-Irwin, C., Franquemont, L., & Donoghue, J. (2013). Failure mode analysis of silicon-based intracortical microelectrode arrays in non-human primates. *Journal of Neural Engineering, 10*(6).

Bartlet, J., DeYoe, E., Doty, R., Lee, B., Lewine, J., Negrao, N., & Overman, W. (2005). Psychophysics of Electrical Stimulation of Striate Cortex in Macaques. *Journal of Neurophysiology, 94*, 3430-3442.

Beautemps, D., Badin, P., & Bailly, G. (2001). Linear degrees of freedom in speech production: analysis of cineradio- and labio-film data and articulatory-acoustic modeling. *JOurnal of the Acoustical Society of America, 109*(5), 2165-2180.

Bezard, E., Basal Gang. Laboratoire de Neurophysiologie (EB, T., CG), Universite de Bordeaux II, Bordeaux, France, Service de Neurochirurgie (J-PN, Y., Centre Hospitalier Universitaire Henri Mondor, Creteil, France, and Units of Neurology and Neurosurgery (FV), G. a. C. s. H. S., Mexico City, Mexico, Boraud, T., Basal Gang. Laboratoire de Neurophysiologie (EB, T., CG), Universite de Bordeaux II, Bordeaux, France, . . . and Units of Neurology and Neurosurgery (FV), G. a. C. s. H. S., Mexico City, Mexico. (1999). Cortical Stimulation and Epileptic Seizure: A Study of the Potential Risk in Primates. *Neurosurgery, 45*(2), 346-350. doi:10.1097/00006123-199908000-00030

Bezard, E., Boraud, T., Nguyen, J. P., Velasco, F., Keravel, Y., & Gross, C. (1999). Cortical stimulation and epileptic seizure: a study of the potential risk in primates. *Neurosurgery, 45*(2), 346-350.

Bhavsar, R., Sun, Y., Helian, N., Davey, N., Mayor, D., & Steffert, T. (2018). The Correlation between EEG Signals as Measured in Different Positions on Scalp Varying with Distance. *Procedia Computer Science, 123*, 92-97. doi:https://doi.org/10.1016/j.procs.2018.01.015

Binnie, C. D., McBride, M. C., Polkey, C. E., Sawhney, I. M., & Janota, I. (1994). Electrocorticography and stimulation. *Acta Neurol Scand Suppl, 152*, 74-82.

Blandini, F., Nappi, G., Tassorelli, C., & Martignoni, E. (2000). Functional changes of the basal ganglia circuitry in Parkinson's disease. *Progress in Neurobiology, 62*(1), 63-88.

Boinagrov, D., Loudin, J., & Palanker, D. (2010). Strength–Duration Relationship for Extracellular Neural Stimulation: Numerical and Analytical Models. In *J Neurophysiol* (Vol. 104, pp. 2236-2248).

Born, R., Trott, A., & Hartmann, T. (2015). Cortical magnification plus cortical plasticity equals vision? *Vision Research, 111*, 161-169.

Bosking, W., Sun, P., Ozker, M., Pei, X., Foster, B., Beauchamp, M., & Yoshor, D. (2017). Saturation in Phosphene Size with Increasing Current Levels Delivered to Human Visual Cortex. *Journal of Neuroscience, 37*(30), 7188-7197.

Bosking, W. H., Beauchamp, M. S., & Yoshor, D. (2017). Electrical Stimulation of Visual Cortex: Relevance for the Development of Visual Cortical Prosthetics. *https://doi.org/10.1146/annurev-vision-111815-114525*. doi:10.1146/annurev-vision-111815-114525

Brindley, G., & Lewin, W. (1968). The sensations produced by electrical stimulation of the visual cortex. *Journal of pHysiology, 196*(2), 479-493.

Brindley, G. S., & Rushton, D. N. (1974). Implanted stimulators of the visual cortex as visual prosthetic devices. *Transactions - American Academy of Ophthalmology and Otolaryngology, 78*, 741-745.

Brown, R. (2013). *Introductory Physics II*. Durham, NC: Duke University Physics Department.

Brunton, E. K., Winther-Jensen, B., Wang, C., Yan, E. B., Hagh Gooie, S., Lowery, A. J., & Rajan, R. (2015). In vivo comparison of the charge densities required to evoke motor responses

using novel annular penetrating microelectrodes. *Front Neurosci, 9*. doi:10.3389/fnins.2015.00265
Butterwick, A., Vankov, A., Huie, P., Freyvert, Y., & Palanker, D. (2007). Tissue Damage by Pulsed Electrical Stimulation. *IEEE Transactions on Biomedical Engineering, 54*(12), 2261-2267.
Buzsaki, G., Anastassiou, C. A., & Koch, C. (2012). The origin of extracellular fields and currents--EEG, ECoG, LFP and spikes. *Nature Neurosceince, 13*(6), 407-420.
Buzsáki, G., Anastassiou, C. A., & Koch, C. (2012). The origin of extracellular fields and currents — EEG, ECoG, LFP and spikes. *Nature Reviews Neuroscience, 13*(6), 407. doi:doi:10.1038/nrn3241
Cain, N., Iyer, R., Koch, C., & Mihalas, S. (2016). The Computational Properties of a Simplified Cortical Column Model. *PLOS Computational Biologu, 12*(9).
Casey, K. (1988). Electromagnetic Shielding Behavior of Wire-Mesh Screens. *IEEE Transactions on Electromagnetic Compatibility, 30*(3), 298-306.
Cattell, M., & Gerard, R. W. (1935). The "inhibitory" effect of hih frequency stimulaiton and the excitation state of nerve. *The Journal of Physiology, 83*(4).
Chang, E. (2015). Towards Large-Scale, Human-Based, Mesoscopic Neurotechnologies. *Neuron, 86*(1), 68-78.
Chang, E., Rieger, J., JOhnson, K., Berger, M., Barbaro, N., & Knight, R. (2010). Categorical speech representation in human superior temporal gyrus. *Nature Neuroscience, 13*, 1428-1432.
Chao, Z., Nagasaka, Y., & Fuji, N. (2010). Long-Term Asynchronous Decoding of Arm Motion Using Electrocorticographic Signals in Monkeys. *Frontiers in Neuroengineering, 3*.
Chapman, J., Hewett, D., & Trefethen, L. (2015). Mathematics of the Faraday Cage. *SIAM Review, 57*(3), 398-417.
Chauvel, P., Landre, E., Trottier, S., Vignel, J. P., Biraben, A., Devaux, B., & Bancaud, J. (1993). Electrical stimulation with intracerebral electrodes to evoke seizures. *Adv Neurol, 63*, 115-121.
Chen, R., Canales, A., & Anikeeva, P. (2017). Neural recording and modulation. *Nature Reviews, 2*(1).
Chen, R., Canales, A., & Anikeeva, P. (2017). Neural recording and modulation technologies. *Nature Reviews Materials, 2*(2), 16093. doi:doi:10.1038/natrevmats.2016.93
Cheng, D. L., Greenberg, P. B., & Borton, D. A. (2017). Advances in Retinal Prosthetic Research: A Systematic Review of Engineering and Clinical Characteristics of Current Prosthetic Initiatives. *Current Eye Research, 42*(3), 334-347.
Chestek, C., Gilja, V., Blabe, C., Foster, B., Shenoy, K., Parvizi, J., & Henderson, J. (2013). Hand posture classification using electrocorticography signals in the gamma band over human sensorimotor brain areas. *Journal of Neural Engineering, 10*.
Christie, B., Ashmont, K., House, P., & Greger, B. (2016). Approaches to a cortical vision prosthesis: implicaitons of electrode size and placement. *Journal of Neural Engineering, 13*.
Cogan, S. (2008). Neural Stimulation and Recording Electrodes. *Annual Review of Biomedical Engineering, 10*, 275-309.
Cogan, S., Ludwig, K., Welle, C., & Takmakov, P. (2016). Tissue damage thresholds during therapeutic electrical stimulation. *Journal of Neural Engineering, 13*.
Cogan, S. F., Troyk, P. R., Ehrlich, J., Plante, T. D., & Detlefsen, D. E. (2006). Potential-biased, asymmetric waveforms for charge-injection with activated iridium oxide (AIROF) neural stimulation electrodes. *IEEE Trans Biomed Eng, 53*(2), 327-332. doi:10.1109/tbme.2005.862572
Colbert, C., & Johnston, D. (1996). Axonal Action-Potential Initiation and Na+ Channel Densities in the Soma and Axon Initial Segment of Subicular Pyramidal Neurons. *The Journal of Neuroscience, 16*(21), 6676-6686.

Collinger, J. L., Foldes, S., Bruns, T. M., Wodlinger, B., Gaunt, R., & Weber, D. J. (2013). Neuroprosthetic technology for individuals with spinal cord injury. *J Spinal Cord Med, 36*(4), 258-272. doi:10.1179/2045772313y.0000000128

Compensation for Blindness With the Intelligent Retinal Implant System (IRIS V2) in Patients With Retinal Dystrophy (IRIS 2),. Retrieved from https://clinicaltrials.gov/ct2/show/NCT02670980

Cowey, A., & Rolls, E. (1974). Human cortical magnification factor and its relation to visual acuity. *Experimental Brain Research, 231*(5), 447-454.

Davis, T., Parker, R., House, P., Bagley, E., Wendelken, S., Normann, R., & Greger, B. (2012). Spatial and temporal characteristics of V1 microstimulation during chronic implantation of a microelectrode array in a behaving macaque. *Journal of Neural Engineering, 9*(6).

Dayan, P., & Abbot, L. F. (2000). *Theoretical Neuroscience: Computational and Mathematical Modeling*.

Degenhart, A., Hiremath, S., Yang, Y., Foldes, S., Collinger, J., Boninger, M., . . . Wang, W. (2018). Remapping cortical modulation for electrocorticographic brain–computer interfaces: a somatotopy-based approach in individuals with upper-limb paralysis. *Journal of Neural Engineering, 15*.

DeHemptinne, C., Ryapolova-Webb, E., Air, E., Garcia, P., Miller, K., Ojemann, J., . . . Starr, P. (2012). Exaggerated phase-amplitude coupling in the primary motor cortex in Parkinson disease. *Proceedings of the National Academy of Sciences of the United States of America, 110*(12), 4780-4785.

DeHemptinne, C., Swann, N., Ostrem, J., Ryapolova-Webb, E., SanLuciano, M., Galifianakis, N., & Starr, P. (2015). Therapeutic deep brain stimulation reduces cortical phase-amplitude coupling in Parkinson's disease. *Nature Neuroscience, 18*(5), 779-789.

DeMichele, G., & Troyk, P. (2003). *Stimulus-resistant neural recording amplifier.* Paper presented at the Annual International COnference of the IEEE EMBS, Cancun, Mexico.

DeYoe, E., Lewine, J., & Doty, R. (2005). Laminar variation in threshold for detection of electrical excitation of striate cortex by macaques. *Journal of Neurophysiology, 94*(5), 3443-3450.

Dobelle, W., Quest, D., Antunes, J., Roberts, T., & Girvin, J. (1979). Artificial vision for the blind by electrical stimulation of the visual cortex. *Neurosurgery, 5*(4), 521-527.

Dokos, S., Suaning, G. J., & Lovell, N. H. (2005). A bidomain model of epiretinal stimulation. *IEEE Trans Neural Syst Rehabil Eng, 13*(2), 137-146. doi:10.1109/tnsre.2005.847390

Dougherty, E. T., Turner, J. C., & Vogel, F. (2014). Multiscale coupling of transcranial direct current stimulation to neuron electrodynamics: modeling the influence of the transcranial electric field on neuronal depolarization. *Comput Math Methods Med, 2014*, 360179. doi:10.1155/2014/360179

Dow, B., Snyder, A., Vautin, R., & Bauer, R. (1981). Magnification factor and receptive field size in foveal striate cortex of the monkey. *Experimental Brain Research, 44*(2), 213-228.

Duncan, R., & Boynton, G. (2003). Cortical Magnification within Human Primary Visual Cortex Correlates with Acuity Thresholds. *Neuron, 38*(4), 659-671.

Einevoll, G., Kayser, C., Logothetis, N., & Panzeri, S. (2013). Modelling and analysis of local field potentials for studying the function of cortical circuits. *Nature Reviews Neuroscience, 14*, 770-785.

Fernandez, E., Greger, B., House, P., Aranda, I., Botella, C., Soto-Sanchez, C., . . . Normann, R. (2014). Acute human brain responses to intracortical microelectrode arrays: challenges and future prospects. *Frontiers in Neuroengineering*, 7-24.

Filed-Fote, E., & Spielholtz, N. (2003). Monophasic and biphasic stimulation evoke different responses. *Muscle and Nerve, 28*, 239-241.

Fridman, G. Y., Blair, H. T., Blaisdell, A. P., & Judy, J. W. (2010). Perceived intensity of somatosensory cortical electrical stimulation. *Exp Brain Res, 203*(3), 499-515. doi:10.1007/s00221-010-2254-y

Frontiers | Using Biophysical Models to Understand the Effect of tDCS on Neurorehabilitation: Searching for Optimal Covariates to Enhance Poststroke Recovery | Neurology. (2018). doi:doi:10.3389/fneur.2017.00058

Galvan, A., Devergnas, A., & Wichmann, T. (2015). Alterations in neuronal activity in basal ganglia-thalamocortical circuits in the parkinsonian state. *Frontiers in Neuroanatomy, 9*(5).
Galvan, A., & Wichmann, T. (2008). Pathophysiology of parkinsonism. *Clinical Neurophysiology, 119*(7), 1459-1474.
Gilbert, C., & Wiesel, T. (1989). Columnar specificity of intrinsic horizontal and corticocortical connections in cat visual cortex. doi:10.1523/JNEUROSCI.09-07-02432.1989
Gilbert, C. D. (1977). Laminar differences in receptive field properties of cells in cat primary visual cortex. *J Physiol, 268*(2), 391-421.
Goddard, G. V., McIntyre, D. C., & Leech, C. K. (1969). A permanent change in brain function resulting from daily electrical stimulation. *Experimental Neurology, 25*(3), 295-330.
Goodman, B. (2008). Channels active in the excitability of nerves and skeletal muscles across the neuromuscular junction: basic function and pathophysiology. *Advances in Physiology Education, 32*(2), 127-135.
Graczyk, E. L., Schiefer, M. A., Saal, H. P., Delhaye, B. P., Bensmaia, S. J., & Tyler, D. J. (2016). The neural basis of perceived intensity in natural and artificial touch. *Sci Transl Med, 8*(362), 362ra142. doi:10.1126/scitranslmed.aaf5187
Groiss, S., Wojtecki, L., Sudmeyer, M., & Schnitzler, A. (2009). Deep Brain Stimulation in Parkinson's Disease. *THerapeutic Advances in Neurological Disorders, 2*(6), 20-28.
Hall, J., & Guyton, A. (2006). *Guyton and Hall Textbook of Medical Physiology, 12 ed*. Philadelphia, PA: Saunders.
Harrison, R. (2008). The Design of Integrated Circuits to Observe Brain Activity. *Proceedings of the IEEE*, 1203-1216.
Hashimoto, T., Elder, C., & Vitek, J. (2002). A template subtraction method for stimulus artifact removal in high-frequency deep brain stimulation. *Journal of Neuroscience Methods, 113*(2), 181-186.
Heck, Stephens, Massey, Nair, Jobst, Barkley, . . . Morrell. (2014). Two-year seizure reduction in adults with medically intractable partial onset epilepsy treated with responsive neurostimulation: Final results of the RNS System Pivotal trial. *Epilepsia, 10*.
Heffer, L., & Fallo, J. (2008). A Novel Stimulus Artifact Removal Technique for High-Rate Electrical Stimulation. *Journal of Neurodcience Methods, 170*(2), 227-284.
Henriquez, C. S. (1993). Simulating the electrical behavior of cardiac tissue using the bidomain model. *Crit Rev Biomed Eng, 21*(1), 1-77.
Herff, C., Heger, D., de Pesters, A., Telaar, D., Brunner, P., Schalk, G., & Schultz, T. (2015). Brain-to-text: decoding spoken phrases from phone representations in the brain. *Frontiers in Neuroscience, 9*(217).
Hiremath, S., Tyler-Kabara, E., Wheeler, J., Moran, D., Gaunt, R., Collinger, J., . . . Wang, W. (2017). Human perception of electrical stimulation on the surface of somatosensory cortex. *PLOS One, 12*(5).
Hodgkin, A., & Huxley, A. (1952). A quantitative description of membrane currents and its application to conduction and excitation in nerve. *Journal of Physiology, 117*(4), 500-544.
Horton, J., & Hoyt, W. (1991). The representation of the visual field in human striate cortex. A revision of the classic Holmes map. *Archives of Opthalmology, 109*(6), 816-824.
Hsu-Lin Luo, Y., & da Cruz, L. (2016). The Argus® II Retinal Prosthesis System. *Progress in Retinal and Eye Research, 50*, 89-107.
Humayun, M., DaCruz, L., Dagnelie, G., Stanga, P., Ho, A., Greenberg, R., . . . Sachel, J. (2013). Recent Results from Second Sight's Argus® II Retinal Prosthesis Study. *Investagative Opthalmology and VIsual Science, 54*(15).
Humayun, M. S., Dorn, J. D., Ahuja, A. K., Caspi, A., Dagnelle, G., Salzmann, J., . . . Greenberg, R. J. (2009). *Preliminary 6 month results from the argustm ii epiretinal prosthesis feasibility study.* Paper presented at the 2009 Annula International Conference of the IEEE Engineering ain Medicine and Biology Society.
Intelligent Medical Implants GmBH. IRIS PILOT Extended Pilot Study With a Retinal Implant System. Retrieved from https://clinicaltrials.gov/ct2/show/NCT00427180

Johnson, L., Wander, J., Sarma, D., Su, D., Fetz, E., & Ojemann, J. (2013). Direct electrical stimulation of somatosensory cortex in humans using electrocorticography electrodes: a qualitative and quantitative report. *Journal of Neural Engineering, 10*(3).

Johnson, L. A., Wander, J. D., Sarma, D., Su, D. K., Fetz, E. E., & Ojemann, J. G. (2013). Direct electrical stimulation of somatosensory cortex in humans using electrocorticography electrodes: a qualitative and quantitative report. *J Neural Eng, 10*(3), 036021. doi:10.1088/1741-2560/10/3/036021

Joucla, S., Glière, A., & Yvert, B. (2014). Current approaches to model extracellular electrical neural microstimulation. *Front Comput Neurosci, 8*. doi:10.3389/fncom.2014.00013

Kellis, S., Miller, K., Thomson, K., Brown, R., House, P., & Greger, B. (2011). Decoding spoken words using local field potentials recorded from the cortical surface. *Journal of Neural Engineering, 7*(5).

Kellis, S., Sorensen, L., Darvas, F., Sayres, C., O"Neill, K., Brown, R., . . . Greger, B. (2016). Multi-scale analysis of neural activity in humans: Implications for micro-scale electrocorticography. *Clinical Neurophysiology, 127*(1), 591-601.

Kevric, J. Comparison of signal decomposition methods in classification of EEG signals for motor-imagery BCI system. In: Elsevier Science.

Kevric, J., & Subasi, A. (2017). Comparison of signal decomposition methods in classification of EEG signals for motor-imagery BCI system. *31*.

Kitzmiller, J., Beversdorf, D., & Hansford, D. (2006). Fabrication and testing of microelectrodes for small-field cortical surface electrodes. *Biomems Materals and Fabrication Technology, 8*, 81-85.

Kole, M., & Stuart, G. (2008). Is action potential threshold lowest in the axon? *Nature Neuroscience, 11*, 1253-1255.

Koop, M., Andrzejewski, A., Hill, B., Heit, G., & Bronte-Stewart, H. (2006). Improvement in a quantitative measure of bradykinesia after microelectrode recording in patients with Parkinson's disease during deep brain stimulation surgery. *Movement DIsorders, 21*(5), 673-678.

Kottaimalai, R., Rajasekaran, M. P., Selvam, V., & Kannapiran, B. (2013). *EEG signal classification using Principal Component Analysis with Neural Network in Brain Computer Interface applications*. Paper presented at the 2013 IEEE International Conference ON Emerging Trends in Computing, Communication and Nanotechnology. http://ieeexplore.ieee.org/stamp/stamp.jsp?tp=&arnumber=6528498

Kottaimalai, R., Rajasekeran, M., Selvam, V., & Kannapiran, B. (2013). *EEG signal classification using Principal Component Analysis with Neural Network in Brain Computer Interface Applications.* Paper presented at the International Conference on Emerging Trends in Computing, Communication, and Nanotechnology.

Kovac, S., Kahane, P., & Diehl, B. (2016). Seizures induced by direct electrical cortical stimulation--Mechanisms and clinical considerations. *Clin Neurophysiol, 127*(1), 31-39. doi:10.1016/j.clinph.2014.12.009

Kringelbach, M., Jenkinson, N., Owen, S., & Aziz, T. (2007). Translational principles of deep brain stimulation. *Nature Reviews Neuroscience, 8*, 623-635.

Kroll, M. W. (1993). A minimal model of the monophasic defibrillation pulse. *Pacing Clin Electrophysiol, 16*(4 Pt 1), 769-777.

Kubanek, J., Miller, K., Ojemann, J., & Schalk, G. (2009). Decoding flexion of individual fingers using electrocorticographic signals in humans. *Journal of Neural Engineering, 6*.

Kumsa, D., Steinke, G. K., Hudak, E., Montague, F., Kelley, S., Untereker, D., . . . Takmakov, P. (2018). Public Regulatory Databases as a Source of Insight for Neuromodulation Device Stimulation Parameters. *Neuromodualtion, 21*(2), 117-125.

Kumsa, D., Steinke, G. K., Molnar, G. F., Hudak, E. M., Montague, F. W., Kelley, S. C., . . . Takmakov, P. A. (2018). Public Regulatory Databases as a Source of Insight for Neuromodulation Devices Stimulation Parameters. *Neuromodulation, 21*(2), 117-125. doi:10.1111/ner.12641

Lange, G., Low, C., Johar, K., Hanapiah, F., & Kamaruzaman, F. (2016). *Classification of Electroencephalogram Data from Hand Grasp and Release Movements for BCI*

Controlled Prosthesis. Paper presented at the 3rd international Conference on System-Integrated Intelligence: New Challenges for Product and Production Engineering.
Lange, G., Low, C. Y., Johar, K., Hanapiah, F. A., & Kamaruzaman, F. (2016). Classification of Electroencephalogram Data from Hand Grasp and Release Movements for BCI Controlled Prosthesis. *Procedia Technology, 26*, 374-381. doi:https://doi.org/10.1016/j.protcy.2016.08.048
Lapicque, L. (1907). Recherches quantitatives sur l'excitation electrique des nerfs traitee comme une polarization. *J Physiol Pathol Gen, 9*, 620-635. doi:citeulike-article-id:4531815
Lee, B., Kramer, D., Armenta Salas, M., Kellis, S., Brown, D., Dobreva, T., . . . Andersen, R. A. (2018). Engineering Artificial Somatosensation Through Cortical Stimulation in Humans. *Front Syst Neurosci, 12*, 24. doi:10.3389/fnsys.2018.00024
Lees, A., Hardy, J., & Recesz, T. (2009). Parkinson's Disease. *The Lancet, 373*(9680), 2055-2066.
Lewis, P., & Rosenfield, J. (2016). Electrical stimulation of the brain and the development of cortical visual prostheses: An historical perspective. *Elsevier, 1630*, 208-224.
Lewis, P. M., Ackland, H. M., Lowery, A. J., & Rosenfeld, J. V. (2015). Restoration of vision in blind individuals using bionic devices: a review with a focus on cortical visual prostheses. *Brain Res, 1595*, 51-73. doi:10.1016/j.brainres.2014.11.020
Lewis, P. M., & Rosenfeld, J. V. (2016). Electrical stimulation of the brain and the development of cortical visual prostheses: An historical perspective. *Brain Res, 1630*, 208-224. doi:10.1016/j.brainres.2015.08.038
Logothetis, N. K., Kayser, C., & Oeltermann, A. (2007). In vivo measurement of cortical impedance spectrum in monkeys: implications for signal propagation. *Neuron, 55*(5), 809-823. doi:10.1016/j.neuron.2007.07.027
Ludwig, K., Miriani, R., Langhals, N., Joseph, M., Anderson, D., & Kipke, D. (2009). Using a Common Average Reference to Improve Cortical Neuron Recordings From Microelectrode Arrays. *Journal of Neurophysiology, 101*(3), 1679-1689.
Malmivuo, J., & Plonsey, R. (1995). *Bioelectric Magnetism - Principles and Applications of Bioelectric and Biomagnetic Fields*. New York: Oxford University Press.
Marc, R., & Jones, B. (2003). Retinal remodeling in inherited photoreceptor degenerations. *Molecular Neurobiology, 28*, 139-147.
Matsuo, T., Kawasaki, K., Osada, T., Sawahata, H., Suzuki, T., Shibata, M., . . . Hasegawa, I. (2011). Intrasulcal electrocorticography in macaque monkeys with minimally invasive neurosurgical protocols. *Fronteirs in Systems Neuroscience, 5*(34).
Maynard, E., Nordhausen, C., & Normann, R. (1997). The Utah Intracortical Electrode Array: A recording structure for potential brain-computer interfaces. *Electroencephalography and Clinical Neurophysiology, 102*(3), 228-239.
McCreery, D., Agnew, W., Yuen, T., & Bullara, L. (1990). Charge Density and Charge Per Phase as Cofactors in Neural Injury Induced by Electrical Stimulation. *IEEE Transactions on Biomedical Engineering, 37*(10), 996-1001.
McCreery, D. B., Agnew, W. F., Yuen, T. G., & Bullara, L. (1990). Charge density and charge per phase as cofactors in neural injury induced by electrical stimulation. *IEEE Trans Biomed Eng, 37*(10), 996-1001.
McIntyre, C. C., & Grill, W. M. (2001). Finite element analysis of the current-density and electric field generated by metal microelectrodes. *Ann Biomed Eng, 29*(3), 227-235.
Meffin, H., Tahayori, B., Sergeev, E. N., Mareels, I. M., Grayden, D. B., & Burkitt, A. N. (2014). Modelling extracellular electrical stimulation: part 3. Derivation and interpretation of neural tissue equations. *J Neural Eng, 11*(6), 065004. doi:10.1088/1741-2560/11/6/065004
Mehring, C., Nawrot, M., Cardoso de Oliveira, S., Vaadia, E., Schulze-Bonhage, A., Aertsen, A., & Ball, T. (2004). Comparing information about arm movement direction in single channels of local and epicortical field potentials from monkey and human motor cortex. *Journal of Physiology-Paris, 4*(6), 498-506.
Merrill, D., Bikson, M., & Jefferys, J. (2005). Electrical stimulation of excitable tissue: design of efficacious and safe protocols. *Jouranl of Neuroscience Methods, 141*, 171-198.

Merrill, D. R., Bikson, M., & Jefferys, J. G. (2005). Electrical stimulation of excitable tissue: design of efficacious and safe protocols. *J Neurosci Methods, 141*(2), 171-198. doi:10.1016/j.jneumeth.2004.10.020

Mountcastle, V. B. (1957). Modality and topographic properties of single neurons of cat's somatic sensory cortex. *Jounral of Neurophysiology, 20*(4), 408-434.

MOuntcastle, V. B. (1997). The columnar organization of the neocortex. *Brain, 120*, 701-722.

Mugler, E., Patton, J., Flint, R., Wright, Z., Schuele, S., Rosenow, J., . . . Slutzky, M. (2014). Direct classification of all American English phonemes using signals from functional speech motor cortex. *Journal of Neural Engineering, 11*.

Multiscale Finite Element Model of the Electrically Active Neural Tissue - IEEE Conference Publication. (of Conference: 9-12 Sept. 2007 Date Added to IEEE Xplore: 26 December 2007 ISBN Information: INSPEC Accession Number: 9810624 DOI: 10.1109/EURCON.2007.4400409Publisher: IEEE Conference Location: Warsaw, Poland). Retrieved from https://ieeexplore.ieee.org/document/4400409

Nam, Y., Brown, E., Ross, J., Blum, R., Wheeler, B., & DeWeerth, S. (2009). A retrofitted neural recording system with a novel stimulation IC to monitor early neural responses from a stimulating electrode. *Journal of Neuroscience Methods, 178*(1), 99-102.

Ni, A., & Maunsell, J. (2010). Microstimulation reveals limits in detecting different signals from a local cortical region. *Current Biology, 20*(9), 824-826.

Normann, R., Maynard, E., Rousche, P., & Warren, D. (1999). A neural interface for a cortical vision prosthesis. *Vision Research, 39*(15), 2577-2587.

Obien, M., Deligkaris, K., Bullman, T., Bakkum, D., & Frey, U. (2015). Revealing neuronal function through microelectrode array recordings. *Frontiers in Neuroscience, 8*.

Oswalt, D., Zhou, D., Tobey, D., Datta, P., Talbot, N., Greenberg, R., . . . Greger, B. (2016). *The potential for evoking visual perception using epicortical microelectrodes: micro-stimulation of primary visual cortex in the nonhuman primate.* Paper presented at the Society for Neuroscience, San DIego.

Padmavathi, P., & Ranganathan, V. (2008). A review on EEG based brain computer interface systems. *International Journal of Emerging Technology and Advanced Engineering, 4*, 2250-2459.

Padmavathi, R., Ranganathan, V. (2008). A Review on EEG Based Brain Computer Interface Systems R.Padmavathi. *International Journal of Emerging Technology and Advanced Engineering, 4*(4), 683-693. doi:ISSN 2250-2459

Pandarinath, C., Nuyujukian, P., Blabe, C., Sorice, B., Saab, J., Willett, F., . . . Henderson, J. (2017). High performance communication by people with paralysis using an intracortical brain-computer interface. *eLIFE, 6*.

Panzeri, S., Macke, J., Gross, J., & Kayser, C. (2015). Neural population coding: combining insights from microscopic and mass signals. *Trends in Congnitive Sciences, 19*(3), 162-172.

Pascolini, D., & Mariotti, S. (2010). Global estimates of visual impairment: 2010. *British Journal of Opthalmology, 96*(5).

Piallat, B., Chabardes, S., Devergnas, A., Torres, N., Allain, M., Barrat, E., & Benabid, A. (2009). Monophasic but not biphasic pulses induce brain tissue damage during monopolar high-frequency deep brain stimulaiton. *Neurosurgery, 64*(1), 156-163.

Pinsky, P., & Rinzel, J. (1994). Intrinsic and Network Rhythmogenesis in a Reduced Traub Model. *Journal of Computational Neuroscience, 1*, 39-60.

Platkiewicz, J., & Brette, R. (2010). A Threshold Equation for Action Potential Initiation. *Computational Biology, 6*(7).

Polikov, V., Tresco, P., & Reichert, W. (2005). Response of brain tissue to chronically implanted neural electrodes. *Journal of Neuroscience Methods, 148*, 1-18.

Potential-biased, asymmetric waveforms for charge-injection with activated iridium oxide (AIROF) neural stimulation electrodes - IEEE Journals & Magazine. (of Publication 23 January 2006). Retrieved from https://ieeexplore.ieee.org/document/1580839/

Pudenz, R. H. (1993). Neural stimulation: Clinical and laboratory experiences. *Surgical Neurology, 39*(3), 235-242. doi:10.1016/0090-3019(93)90190-C

Purves, D., Augustine, G., Fitzpatrick, D., Hall, W., LaMantia, A.-S., McNamara, J., & White, L. (2008). *Neuroscience, Fourth Edition*. Sunderland, MA: Sinauer Associates, Inc.

Rall, W., & Shephard, G. M. (1968). Theoretical reconstruction of field potentials and dendrodendritic synaptic interactions in olfactory bulb. *Journal of Neurophysiology, 31*(6), 884-915.

Read, J. (2015). The place of human psychophysics in modern neuroscienc. *Neuroscience, 269*, 116-129.

Romo, R., Hernandez, A., Zainos, A., & Salinas, E. (1998). Somatosensory discrimination based on cortical microstimulation. *Nature, 392*(6674), 387-390. doi:10.1038/32891

Rousche, P., & Normann, R. (1998). Chronic recording capability of the Utah Intracortical Electrode Array in cat sensory cortex. *Journal of Neuroscience Methods, 82*(1), 1-15.

Rouse, A., Williams, J., Wheeler, J., & Moran, D. (2016). Spatial co-adaptation of cortical control columns in a micro-ECoG brain–computer interface. *Journal of Neural Engineering, 13*.

Sadleir, R. (2010). A Bidomain Model for Neural Tissue. *International Journal of Bioelectromagnetism, 12*(1), 2-6.

Sahin, M., & Tie, Y. (2007). Non-rectangular waveforms for neural stimulation with practical electrodes. *J Neural Eng, 4*(3), 227-233. doi:10.1088/1741-2560/4/3/008

Schevon, C., Trevelyan, A., Schroeder, C., Goodman, R., McKhann, G., & Emerson, R. (1997). Spatial characterization of interictal high frequency oscillations in epileptic neocortex. *Brain, 120*, 701-722.

Schmidt, E., Bak, M., Hambrecht, F., Kufta, C., O'Rourke, D., & Vallabhanath, P. (1996a). Feasibility of a visual prosthesis for the blind based on intracortical micro stimulation of the visual cortex. *Brain, 119*(2), 507-522.

Schmidt, E., Bak, M., Hambrecht, F., Kufta, C., O'Rourke, D., & Vallabhanath, P. (1996b). Feasibility of a visual prosthesis for the blind based on intracortical microstimulation of the visual cortex. *Brain, 119*(2), 507-522.

Schmidt, E. M., Bak, M. J., Hambrecht, F. T., Kufta, C. V., O'Rourke, D. K., & Vallabhanath, P. (1996). Feasibility of a visual prosthesis for the blind based on intracortical microstimulation of the visual cortex. *Brain, 119 (Pt 2)*, 507-522.

Schmolesky, M. (2005). *Webvision: The Organization of the Retina and Visual System*. Salt Lake CIty, UT.

Schwartz, B. L., Chauhan, M., & Sadleir, R. J. (2016). Analytic Modeling of Neural Tissue: I. A Spherical Bidomain. In *J Math Neurosci* (Vol. 6).

Shannon, R. V. (1992). A model of safe levels for electrical stimulation. *IEEE Trans Biomed Eng, 39*(4), 424-426. doi:10.1109/10.126616

Sharott, A. (2014). Local FIeld Potential, Methods of Recording. In *Encylopedia of Computational Neuroscience*. New York: Springer Science.

Silberstein, P., Pogosyan, A., Kuhn, A., Hotton, G., Tisch, S., Kupsch, A., . . . Brown, P. (2005). Cortico-cortical coupling in Parkinson's disease and its modulation by therapy. *Brain, A journal of Neurology, 128*, 1277-1291.

Sillekens, S. (2008). *Influence of Volume Conduction on Beamformer Source Analysis in the Human Brain*. Munster.

Stavisky, S., Kao, J., Nuyujukian, P., Ryu, S., & Shenoy, K. (2015). A high performing brain-machine interface driven by low-frequency local field potentials alone and together with spikes. *Journal of Neural Engineering, 12*(3).

Stingl, K., Schrippert, R., Bartz-Schmidt, K., Besch, D., Cottriall, C., Edwards, T., . . . Troelenber. (2017). Interim Results of a Multicenter Trial with the New Electronic Subretinal Implant Alpha AMS in 15 Patients Blind from Inherited Retinal Degenerations. *Frontiers in Neuroscience, 11*.

Stoney, S. D., Jr., Thompson, W. D., & Asanuma, H. (1968). Excitation of pyramidal tract cells by intracortical microstimulation: effective extent of stimulating current. *J Neurophysiol, 31*(5), 659-669. doi:10.1152/jn.1968.31.5.659

Stuttgen, M., & Schwarz, C. (2008). Psychophysical and neurometric detection performance under stimulus uncertainty. *Nature Neuroscience, 11*, 1091-1099.

Sun, F., & Morrell, M. (2014). Closed-loop Neurostimulation: The Clinical Experience. *Neurotherapeutics, 11*(3), 553-563.
Tehovnik, E., & Slocum, W. (2009). Depth-dependent detection of microampere currents delivered to monkey V1. *European Journal of Neuroscience, 29*(7), 1477-1489.
Tehovnik, E. J. (1996). Electrical stimulation of neural tissue to evoke behavioral responses. *J Neurosci Methods, 65*(1), 1-17.
Tootell, R., Silverman, M., Switkes, E., & De Valois, R. (1982). Deoxyglucose analysis of retinotopic organization in primate striate cortex. *Science, 218*, 902-904.
Torab, K., Davis, T., Warren, D., House, P., Normann, R., & Greger, B. (2011). Multiple factors may influence the performance of a visual prosthesis based on intracortical microstimulation: nonhuman primate behavioural experimentation. *Journal of Neural Engineering, 8*(3).
Troyk, P. (2017). The Intracortical Visual Prosthesis Project. In *Artificial Vision* (pp. 203-214): Springer.
Tsui, B. (2008). *Atlas of Ultrasound- and Nerve Stimulation-Guided Regional Anesthesia*. NY: Springer-Verlag.
Van Essen, D., Newsome, W., & Maunsell, J. (1984). The visual field representation in striate cortex of the macaque monkey: Asymmetries, anisotropies, and individual variability. *Vision Research, 24*(5), 429-448.
Vansteensel, M., Pels, E., Cleichner, M., Branco, M., Denison, T., Freudenburg, P., . . . Ramsey, N. (2016). Fully Implanted Brain–Computer Interface in a Locked-In Patient with ALS. *New England Jounral of Medicine, 375*, 2060-2066.
Wagenaar, D., & Potter, S. (2002). Real-time multi-channel stimulus artifact suppression by local curve fitting. *Journal of Neuroscience Methods, 120*(2), 113-120.
Wang, X., Gkogkidis, C., Iljina, O., Fiederer, L., Henle, C., Mader, I., . . . Ball, T. (2017). Mapping the fine structure of cortical activity with different micro-ECoG electrode array geometries. *Journal of Neural Engineering, 14*.
Watanbe, H., Sato, M., Nambu, A., Kawato, M., & Isa, T. (2012). Reconstruction of movement-related intracortical activity from micro-electrocorticogram array signals in monkey primary motor cortex. *Journal of Neural Engineering, 9*(3).
Weber, B., Keller, A., J., R., & Logothetis, N. (2008). The microvascular system of striate and extrastriate visual cortex of the macaque. *Cerebral Cortex, 18*(10), 2318-2330.
WEISS, G., & Weiss, G. (1901). Sur la possibilité de rendre comparables entre eux les appareils servant à l'excitation électrique.
Wen, D., Jia, P., Lian, Q., Zhou, Y., & Lu, C. (2016). Review of Sparse Representation-Based Classification Methods on EEG Signal Processing for Epilepsy Detection, Brain-Computer Interface and Cognitive Impairment. *Front Aging Neurosci, 8*. doi:10.3389/fnagi.2016.00172
Wen, D., Jia, P., Zhou, Y., & Lu, C. (2016). Review of Sparse Representation-Based Classificaion Methods on EEG Signal Processing for Epilepsy Detection, Brain-Computer Interface, and Cognitive Impairment. *Frontiers in Aging Neuroscience, 8*.
Winawer, J., & Parvizi, J. (2016). Linking Electrical Stimulation of Human Primary Visual Cortex, Size of Affected Cortical Area, Neuronal Responses, and Subjective Experience. *Neuron, 92*, 1-7.
Winter, J. O., Cogan, S. F., & Rizzo, J. F. (2007). Retinal prostheses: current challenges and future outlook. *Journal of Biomaterials Science, Polymer Edition, 18*(8), 1031-1055.
Wise, K. D. (2005). Silicon microsystems for neuroscience and neural prostheses. *IEEE Engineering in Medicine and Biology Magazine, 24*(5), 22-29.
Wolpaw, J., Birbaumer, N., McFarland, D., Pfurtscheller, G., & Vaughan, T. (2002). Brain-Computer Interfaces for Communication and Control. *Clinical Neurophysiology, 113*, 767-791.
Wolpaw, J. R., Birbaumer, N., McFarland, D. J., Pfurtscheller, G., & Vaughan, T. M. (2002). Brain-computer interfaces for communication and control. *Clin Neurophysiol, 113*(6), 767-791.

Wongsarnpigoon, A., Woock, J. P., & Grill, W. M. (2010). Efficiency Analysis of Waveform Shape for Electrical Excitation of Nerve Fibers. *IEEE Trans Neural Syst Rehabil Eng, 18*(3), 319-328. doi:10.1109/tnsre.2010.2047610

Woodlinger, B., Downey, J., Tyler-Kabara, E., Schwartz, A., Bininger, M., & Collinger, J. (2015). Ten-dimensional anthropomorphic arm control in a human brain-machine interface: difficulties, solutions, and limitations. *Journal of Neural Engineering, 12*(1).

Wu, W., Gao, Y., Bienenstock, E., Donoghue, J. P., & Black, M. J. (2006). Bayesian population decoding of motor cortical activity using a Kalman filter. *Neural Comput, 18*(1), 80-118. doi:10.1162/089976606774841585

Yang, T., Hakimian, S., & Schwartz, T. (2014). Intraoperative ElectroCorticoGraphy (ECog): indications, techniques, and utility in epilepsy surgery. *Epileptic Disorders, 16*(3).

Ye, H., & Steiger, A. (2015). Neuron matters: electric activation of neuronal tissue is dependent on the interaction between the neuron and the electric field. *Journal of NeuroEngineering and Rehabilitation, 12*(1), 65. doi:doi:10.1186/s12984-015-0061-1

Ye, H., & Steiger, A. (2015). Neuron matters: electric activation of neuronal tissue is dependent on the interaction between the neuron and the electric field. In *J Neuroeng Rehabil* (Vol. 12).

Yuen, T. G., Agnew, W. F., Bullara, L. A., Jacques, S., & McCreery, D. B. (1981). Histological evaluation of neural damage from electrical stimulation: considerations for the selection of parameters for clinical application. *Neurosurgery, 9*(3), 292-299.

Zhuang, J., Truccolo, W., Vargas-Irwin, C., & Donoghue, J. P. (2010). Decoding 3-D reach and grasp kinematics from high-frequency local field potentials in primate primary motor cortex. *IEEE Trans Biomed Eng, 57*(7), 1774-1784. doi:10.1109/tbme.2010.2047015

APPENDIX A

NHP ANIMAL RESEARCH PROTOCOL

Institutional Animal Care and Use Committee (IACUC)
Office of Research Integrity and Assurance
Arizona State University
660 South Mill Avenue, Suite 315
Tempe, Arizona 85287-6111
Phone: (480) 965-4387 *FAX:* (480) 965-7772

Animal Protocol Review

ASU Protocol Number:	**16-1512R**
Protocol Title:	**Neural Interfaces for Control of Prostheses**
Principal Investigator:	**Bradley Greger**
Date of Action:	**6/23/2016**

The animal protocol review was considered by the Committee and the following decisions were made:

The protocol was approved by Full Committee Review as modified.

If you have not already done so, documentation of Level III Training (i.e., procedure-specific training) will need to be provided to the IACUC office before participants can perform procedures independently. For more information on Level III requirements see https://researchintegrity.asu.edu/training/animals/levelthree.

Total # of Animals:	**6**	
Species:	**NHP**	**Pain Level: D**

Protocol Approval Period: **6/23/2016 – 6/22/2019**

Sponsor:	**N/A**
ASU Proposal/Award #:	**N/A**
Title:	**N/A**

Signature: Augustowski for C Johnson
IACUC Chair or Designee

Date: 6/28/2016

Cc: IACUC Office
IACUC Chair

APPENDIX B

CHARGE CHARACTERIZATION DATA FOR NHP1

Table A.1

Charge Characterization Parameter Values

Pulse Freq (Hz)	Pulse Width (ms)	Tain Length (ms)	FPW	FPT	Phase Ratio (l:f)	Num Pulses	Current (mA)	Charge per Phase (mC)	Charge Density (mC/cm^2)	Pulse Train Charge (mC)	Num Trials	DPI
50	0.1	300	5	1.5	1	15	1.125	0.113	0.358	1.688	286	336
50	0.3	300	15	4.5	1	15	0.693	0.208	0.662	3.119	401	333
50	0.4	300	20	6.0	1	15	0.646	0.258	0.823	3.876	240	331
50	0.6	300	30	9.0	1	15	0.548	0.329	1.047	4.932	406	328
100	0.1	300	10	3.0	1	30	1.084	0.108	0.345	3.252	425	294
100	0.3	300	30	9.0	1	30	0.572	0.172	0.546	5.148	237	233
100	0.3	150	30	4.5	1	15	0.589	0.177	0.562	2.651	231	420
100	0.3	300	30	9.0	4	30	0.492	0.148	0.470	4.428	194	385
100	0.4	300	40	12.0	1	30	0.550	0.220	0.700	6.600	228	290
100	0.4	300	40	12.0	4	30	0.429	0.172	0.546	5.148	215	384
100	0.6	300	60	18.0	1	30	0.435	0.261	0.831	7.830	234	289
100	0.6	150	60	9.0	1	15	0.448	0.269	0.856	4.032	252	419
100	0.6	300	60	18.0	4	30	0.372	0.223	0.710	6.696	159	383
150	0.1	300	15	4.5	1	45	0.998	0.100	0.318	4.491	218	320
150	0.3	300	45	13.5	1	45	0.451	0.135	0.431	6.089	223	309

Pulse Freq (Hz)	Pulse Width (ms)	Tain Length (ms)	FPW	FPT	Phase Ratio (l:f)	Num Pulses	Current (mA)	Charge per Phase (mC)	Charge Density (mC/cm^2)	Pulse Train Charge (mC)	Num Trials	DPI
150	0.3	100	45	4.5	1	15	0.463	0.139	0.442	2.084	213	422
150	0.4	300	60	18.0	1	45	0.425	0.170	0.541	7.650	651	307
150	0.6	300	90	27.0	1	45	0.316	0.190	0.604	8.532	203	312
150	0.6	100	90	9.0	1	15	0.419	0.251	0.800	3.771	363	418
200	0.1	300	20	6.0	1	60	0.860	0.086	0.274	5.160	886	258
200	0.1	300	20	6.0	2	60	0.624	0.062	0.199	3.744	285	415
200	0.1	300	20	6.0	3	60	0.606	0.061	0.193	3.636	259	353
200	0.1	300	20	6.0	4	60	0.602	0.060	0.192	3.612	248	375
200	0.3	300	60	18.0	1	60	0.428	0.128	0.409	7.704	171	256
200	0.3	75	60	4.5	1	15	0.435	0.131	0.415	1.958	206	423
200	0.3	300	60	18.0	2	60	0.344	0.103	0.328	6.192	262	356
200	0.3	300	60	18.0	3	60	0.273	0.082	0.261	4.914	356	349
200	0.3	300	60	18.0	4	60	0.243	0.073	0.232	4.374	318	361
200	0.4	300	80	24.0	1	60	0.405	0.162	0.516	9.720	321	255
200	0.4	300	80	24.0	2	60	0.327	0.131	0.416	7.848	152	355

Pulse Freq (Hz)	Pulse Width (ms)	Tain Length (ms)	FPW	FPT	Phase Ratio (l:f)	Num Pulses	Current (mA)	Charge per Phase (mC)	Charge Density (mC/cm^2)	Pulse Train Charge (mC)	Num Trials	DPI
200	0.4	300	80	24.0	3	60	0.260	0.104	0.331	6.240	248	349
200	0.4	300	80	24.0	4	60	0.228	0.091	0.290	5.472	347	360
200	0.5	300	100	30.0	3	60	0.245	0.123	0.390	7.350	211	346
200	0.5	300	100	30.0	4	60	0.253	0.127	0.403	7.590	174	415
200	0.6	300	120	36.0	1	60	0.272	0.163	0.519	9.792	254	252
200	0.6	75	120	9.0	1	15	0.332	0.199	0.634	2.988	178	417
200	0.6	300	120	36.0	2	60	0.217	0.130	0.414	7.812	232	354
200	0.6	300	120	36.0	3	60	0.209	0.125	0.399	7.524	391	348
200	0.6	300	120	36.0	4	60	0.216	0.130	0.413	7.776	425	359
300	0.1	300	30	9.0	1	90	0.747	0.075	0.238	6.723	886	258
300	0.1	300	30	9.0	4	90	0.602	0.060	0.192	5.418	249	375
300	0.2	300	60	18.0	1	90	0.424	0.085	0.270	7.632	386	261
300	0.3	300	90	27.0	1	90	0.367	0.110	0.350	9.909	387	256
300	0.3	50	90	4.5	1	15	0.369	0.111	0.352	1.661	244	424
300	0.3	300	90	27.0	4	90	0.348	0.104	0.332	9.396	327	377

Pulse Freq (Hz)	Pulse Width (ms)	Tain Length (ms)	FPW	FPT	Phase Ratio (l:f)	Num Pulses	Current (mA)	Charge per Phase (mC)	Charge Density (mC/cm^2)	Pulse Train Charge (mC)	Num Trials	DPI
300	0.4	300	120	36.0	1	90	0.347	0.139	0.442	12.492	480	254
300	0.4	300	120	36.0	4	90	0.282	0.113	0.359	10.152	228	383
300	0.5	300	150	45.0	1	90	0.313	0.157	0.498	14.085	357	262
300	0.5	300	150	45.0	4	90	0.242	0.121	0.385	10.890	287	372
300	0.6	300	180	54.0	1	90	0.285	0.171	0.544	15.390	170	21
300	0.6	300	180	54.0	1	90	0.287	0.172	0.548	15.498	177	52
300	0.6	300	180	54.0	1	90	0.326	0.196	0.623	17.604	199	82
300	0.6	300	180	54.0	1	90	0.339	0.203	0.647	18.306	198	162
300	0.6	300	180	54.0	1	90	0.313	0.188	0.598	16.902	363	211
300	0.6	300	180	54.0	1	90	0.289	0.173	0.552	15.606	308	230
300	0.6	300	180	54.0	1	90	0.259	0.155	0.495	13.986	254	254
300	0.6	300	180	54.0	1	90	0.272	0.163	0.519	14.688	198	289
300	0.6	300	180	54.0	1	90	0.279	0.167	0.533	15.066	404	323
300	0.6	300	180	54.0	1	90	0.274	0.164	0.523	14.796	281	386
300	0.6	50	180	9.0	1	15	0.279	0.167	0.533	2.511	260	416